Peterhead CCS Project

Doc Title: Special Core Analysis (SCAL) Report and Geomech / Reactive Transport Modelling (RTM) Core Analysis Reports

Doc No. PCCS-05-PTD-ZP-9034-00001
Date of issue: 12/09/2014
Revision: K02
DECC Ref No: 11.112
Knowledge Cat: KKD-Subsurface

KEYWORDS
Goldeneye, CO_2, SCAL, Core.

Produced by Shell U.K. Limited
ECCN: EAR 99 Deminimus

IMPORTANT NOTICE

Information provided further to UK CCS Commercialisation Programme (the "Competition").

The information set out herein (the "Information") has been prepared by Shell U.K. Limited and its sub-contractors (the "Consortium") solely for the Department of Energy & Climate Change in connection with the Competition. The Information does not amount to advice on CCS technology or any CCS engineering, commercial, financial, regulatory, legal or other solutions on which any reliance should be placed. Accordingly, no member of the Consortium makes (and the UK Government does not make) any representation, warranty or undertaking, express or implied, as to the accuracy, adequacy or completeness of any of the Information and no reliance may be placed on the Information. Insofar as permitted by law, no member of the Consortium or any company in the same group as any member of the Consortium or their respective officers, employees or agents accepts (and the UK Government does not accept) any responsibility or liability of any kind, whether for negligence or any other reason, for any damage or loss arising from any use of or any reliance placed on the Information or any subsequent communication of the Information. Each person to whom the Information is made available must make their own independent assessment of the Information after making such investigation and taking professional technical, engineering, commercial, regulatory, financial, legal or other advice, as they deem necessary.

Table of Contents

Table of figures

No table of figures entries found.

List of Tables

1. Introduction

This Key Knowledge Deliverable comprises of two separate reports, which describe basic flow parameters. These are a key element in the reservoir modelling and reservoir management of the Goldeneye Field Well(s). These reports are given in Appendix A and Appendix B under the following references:

- Appendix A
  - 11.112, Special Core Analysis (SCAL) Report, PCCS-05-PT-ZP-9034-00001

- Appendix B
  - 11.112, Geomech/Reactive Transport Modelling (RTM) core analysis report. Also known as Report on Results of lab Experiments (Geo-Mechanical Investigation): Chemo-mechanical response of Captain Sandstone to CO2 injection, PCCS-05-PT-ZP-9018-00001

These core analysis reports include information on relative permeability and capillary pressure analysis as well as details of Special Core analysis: CO2 Flooding experiments and interpreted results performed on the Goldeneye field core.

The Executive Summaries of each report is presented here as an abstract to give a high level overview of this Key Knowledge Deliverable.

2. Executive Summary Abstract

2.1. Appendix A: Special Core Analysis (SCAL) Report

2.1.1. Executive Summary

Special core analysis (SCAL) of the Goldeneye data has been performed through the interpretation of legacy data in addition to a new programme of measurements that have been tailored to the specific needs of carbon storage.

This report is an updated and refocused version of the report originally issued for the Longannet CCS Project.

Assessment of storage capacity and injectivity was based on a reinterpretation of the legacy data, making full use of the in-situ saturation data to account for laboratory artefacts. This allowed ranges to be developed as inputs for the storage assessment for:

- Gas relative permeability at initial water saturation
- Trapped gas saturation to brine
- Water relative permeability at trapped gas saturation

History matches to Goldeneye production performance were achieved within the uncertainty range developed.

The new SCAL programme comprised a combination of ambient condition measurements and reservoir condition floods with CO_2 targeted at the key data uncertainties. An initial analysis of the results confirms the validity of the ranges used in the storage assessment based on the legacy data, so that there is no immediate requirement to update any of the existing reservoir models.

Unexpected differences in flood front dynamics and lowered trapped gas saturations were observed in some of the reservoir condition experiments with CO_2. These would warrant further investigation, including simulation of ambient and reservoir condition drainage and imbibition floods, and selected additional core floods. However, this additional work would not change the overall conclusions of the storage assessment.

The use of mass balance and in-situ saturation techniques proved to be essential in the subsequent interpretation of the results.

The use of mass balance and in-situ saturation techniques proved essential in the subsequent interpretation of results. A set of recommendations are made to further enhance the design of any future CO_2 storage SCAL studies.

2.2. Appendix B: Geomech/Reactive Transport Modelling (RTM) core analysis report.

Also known as Report on Results of lab Experiments (Geo-Mechanical Investigation): Chemo-mechanical response of Captain Sandstone to CO2 injection

2.2.1. Executive Summary

The Goldeneye depleted gas condensate field is a candidate for the storage of CO_2. Injection of CO_2 into a reservoir might result in a range of chemical and mechanical effects, and therefore, understanding the possible effect of chemical reactions on the mechanical properties of the reservoir and cap rock is key.

The rock mechanical properties of Captain D Sandstone of the Goldeneye field and the effect of the CO_2-saturated brine flow on them have been studied using samples obtained from Wells 14/29a-3 and 14/29a-5.

This report is an updated and refocused version of the report originally issued for the Longannet CCS Project.

The Goldeneye reservoir consists of a consolidated sandstone (Captain D Sandstone) with only 6 % cement of which 30 % is calcite ($CaCO_3$). It is known that calcite reacts with acidic CO_2-saturated brine, leading to dissolution. Rock mechanical experiments were performed to obtain a range of key mechanical parameters of the host formation, in order to better constrain numerical modelling efforts. In addition, the effect of CO_2-brine-rock interaction on these rock properties was studied, as well as any associated carbonate cement dissolution. The following parameters have been measured during and after the experiments:

- Young's modulus, Poisson's ratio, bulk modulus before and during CO_2 exposure.
- Failure strength under in-situ conditions, after CO_2 exposure.
- Axial V_p and V_s, as well stress and strain sensitivity (R- and S-factors).
- Pre- and post-experiment sample characterisation: porosity, permeability, microCT scan, XRD and SEM analysis.
- Chemical analysis and pH of effluent.

Important findings of this work are:

i. Calcite was completely dissolved during CO_2-saturated brine flow. This was confirmed by comparison of microCT-scan, XRD and SEM analysis of the pre- and post-experiment sample.
ii. Elemental analysis of the effluent showed an increase of the calcium concentration in the effluent in the first part of the flow phase, indicative of calcite dissolution. In the same part of the flow phase, the pH gradually decreased from pH ~6 to 5, after which it stayed constant for the remainder of the experiment.
iii. No significant change in rock mechanical parameters (Young's modulus, Poisson's ratio, bulk modulus and velocities) was observed in response to the continuous flow of artificial reservoir brine and CO_2-saturated brine.

iv. There was no measurable rock strength reduction as a result of exposure to CO_2-saturated brine, and the concomitant dissolution of calcite.
v. The experiment has shown that P-wave velocity and ultrasonic attenuation are good indicators for supercritical CO_2 coming out of the solution. The S-wave velocity was not sensitive to pore-fluid changes.

The results of these experiments indicate that injecting CO2 into the Captain D Sandstone of the Goldeneye field does not result in a measurable reduction in rock strength.

3. Appendices

Appendix A. Special Core Analysis (SCAL) Report

A.1. 11.112, Special Core Analysis (SCAL) Report, PCCS-05-PT-ZP-9034-00001

Appendix B. Geomech/Reactive Transport Modelling (RTM) core analysis report

B.1. 11.112, Geomech/Reactive Transport Modelling (RTM) core analysis report. Also known as Report on Results of Lab Experiments (Geo-Mechanical Investigation): Chemo-mechanical response of Captain Sandstone to CO2 injection, PCCS-05-PT-ZP-9018-00001

4. Glossary of terms

Term	Definition
CGR	Condensate gas ratio
CCS	Carbon Capture & Storage
CO_2	Carbon Dioxide
CT	Computer Tomography
EDAX	Energy Dispersive X-ray
FFM	Full Field Model
GIIP	Gas Initially In Place
HC	Hydrocarbon
HNBR	Hydrogenated Nitrile Butadiene Rubber
IFT	Interfacial Tension
microCT	Micro-Computer Tomography
PVT	Pressure-Volume-Temperature
QC	Quality Control
SCAL	Special Core Analysis
k_v:k_h	Ratio of vertical to horizontal permeability
SS	Steady State
S_{gi}	Initial gas saturation
S_{gt}	Trapped gas saturation
S_{wi}	Initial water saturation
USBM	United States Bureau of Mines
USS	Unsteady State
Vp	Compressional Velocity
Vs	Shear Wave Velocity
XRD	X-ray Diffraction

5. Glossary of Unit Conversions

For the provision of the SI metric conversion factor as applicable to all imperial units in the Key Knowledge Deliverable.

Table 5-1: Unit Conversion Table

Function	Unit - Imperial to SI Metric conversion Factor
Length	1 Foot = 0.3048m Metres 1 Inch = 2.54cm Centimetres 1 Inch = 25.4mm millimetres
Pressure	1 Psia = 0.0690 Bara
Temperature	1°F Fahrenheit = -17.22°C Centigrade
Weight	1lb Pound = 0.45kg Kilogram

Peterhead CCS Project

APPENDIX A

Doc Title: Special Core Analysis (SCAL) Report

Doc No.	PCCS-05-PT-ZP-9034-00001
Date of issue:	12/09/2014
Revision:	K02
DECC Ref No:	11.112
Knowledge Cat:	KKD-Subsurface

KEYWORDS

Goldeneye, CO_2, SCAL, Core.

Produced by Shell U.K. Limited

ECCN: EAR 99 Deminimus

IMPORTANT NOTICE

Information provided further to UK CCS Commercialisation Programme (the "Competition").

The information set out herein (the "Information") has been prepared by Shell U.K. Limited and its sub-contractors (the "Consortium") solely for the Department of Energy & Climate Change in connection with the Competition. The Information does not amount to advice on CCS technology or any CCS engineering, commercial, financial, regulatory, legal or other solutions on which any reliance should be placed. Accordingly, no member of the Consortium makes (and the UK Government does not make) any representation, warranty or undertaking, express or implied, as to the accuracy, adequacy or completeness of any of the Information and no reliance may be placed on the Information. Insofar as permitted by law, no member of the Consortium or any company in the same group as any member of the Consortium or their respective officers, employees or agents accepts (and the UK Government does not accept) any responsibility or liability of any kind, whether for negligence or any other reason, for any damage or loss arising from any use of or any reliance placed on the Information or any subsequent communication of the Information. Each person to whom the Information is made available must make their own independent assessment of the Information after making such investigation and taking professional technical, engineering, commercial, regulatory, financial, legal or other advice, as they deem necessary.

Table of Contents

Table of Figures

List of Tables

Executive summary

Special core analysis (SCAL) of the Goldeneye data has been performed through the interpretation of legacy data in addition to a new programme of measurements that have been tailored to the specific needs of carbon storage.

This report is an updated and refocused version of the report originally issued for the Longannet CCS Project.

Assessment of storage capacity and injectivity was based on a reinterpretation of the legacy data, making full use of the in-situ saturation data to account for laboratory artefacts. This allowed ranges to be developed as inputs for the storage assessment for:

- Gas relative permeability at initial water saturation
- Trapped gas saturation to brine
- Water relative permeability at trapped gas saturation

History matches to Goldeneye production performance were achieved within the uncertainty range developed.

The new SCAL programme comprised a combination of ambient condition measurements and reservoir condition floods with CO_2 targeted at the key data uncertainties. An initial analysis of the results confirms the validity of the ranges used in the storage assessment based on the legacy data, so that there is no immediate requirement to update any of the existing reservoir models.

Unexpected differences in flood front dynamics and lowered trapped gas saturations were observed in some of the reservoir condition experiments with CO_2. These would warrant further investigation, including simulation of ambient and reservoir condition drainage and imbibition floods, and selected additional core floods. However, this additional work would not change the overall conclusions of the storage assessment.

The use of mass balance and in-situ saturation techniques proved to be essential in the subsequent interpretation of the results.

1. Introduction

SCAL data is an important input to the assessment of the CO_2 storage capacity of the Goldeneye reservoir. Relative permeability and capillary pressure affect the mobility of the different fluid phases in the reservoir, and influence the overall volumetric sweep and the remaining water saturations in CO_2 invaded intervals. Trapped CO_2 saturations to brine imbibition post-injection provide long term storage of CO_2 as an immobile phase and limit the lateral movement of CO_2 in any aquifer storage scenario.

The SCAL study has comprised three stages: development of a conceptual framework for the displacement mechanisms and identification of key uncertainties; review of existing Goldeneye SCAL data; and specification and execution of a new SCAL programme to address uncertainties that have the largest impact on predictions of storage capacity and injectivity. The conceptual framework considered the full cycle of the Goldeneye reservoir:

- Production phase with the reservoir under depletion and subject to aquifer invasion in the hydrocarbon column
- Injection phase with the movement of the CO_2 plume, as highly mobile CO_2 displaces less mobile brine at trapped gas saturation in the original hydrocarbon column and potentially brine in the aquifer
- Post-injection phase with the fluid distribution equilibrating under gravity and the re-imbibition of brine, trapping CO_2

The framework enabled the key aspects of the displacement mechanisms to be identified and the corresponding SCAL data requirements. This focused subsequent modelling of uncertainty and laboratory measurements onto a high graded set of data, from the otherwise wide range of displacement mechanisms occurring in the reservoir. The initial understanding of the displacement processes was confirmed by ongoing comparison with the dynamic modelling in the simulacrum box models and full field models of Goldeneye. The existing SCAL data comprised:

- Steady state (SS) imbibition gas/water relative permeability for wells 14/29a-3 and 14/29a-5
- SS imbibition gas/oil, SS drainage gas/oil, SS imbibition water/oil for Well 20/4b-6

The data was reviewed and uncertainty ranges were developed for the trapped gas saturation to water and the brine endpoint relative permeability at trapped gas. This provided an input to the history matching of the existing Goldeneye production performance.

The new SCAL programme was designed to reconfirm the ranges on trapped gas saturation and water mobility at trapped gas and to extend the data set to the other key relative permeability data controlling CO_2 movement:

- CO_2 relative permeability towards lower water saturations, which influences injectivity and Dietz stability
- Trapped CO_2 saturation to water, which limits the possible movement of CO_2 in the aquifer
- Water primary drainage relative permeability and capillary pressure, which controls the remaining water saturation within the CO_2 plume

The programme uses a series of ambient condition tests using centrifuge and unsteady state (USS) displacements, together with USS reservoir condition measurements with CO_2. The USS

displacements were carefully designed, controlled and monitored to minimise laboratory artefacts. The reservoir condition tests, specifically, use pre-equilibrated CO_2 and brine in a recirculating system. Except for the centrifuge measurements, in-situ saturation monitoring is used throughout to allow more reliable interpretation of the data.

2. Conceptual framework for displacement mechanisms

This section examines the life cycle of the Goldeneye reservoir from initial depletion through to the period after CO_2 injection has been finished and the reservoir system has once again come back to an equilibrium condition. The expected displacement mechanisms were mapped out early in the project, and used to design the SCAL programme, and subsequently confirmed by simulation in box models and the history matched realisations of the full field model (FFM)[1].

A first pass through the displacement mechanisms is just to consider a simple gas water system, without the presence of condensate dropout or the oil rim. At the original conditions the reservoir consists of a gas column overlying the water leg, **Fig. 2.1**.

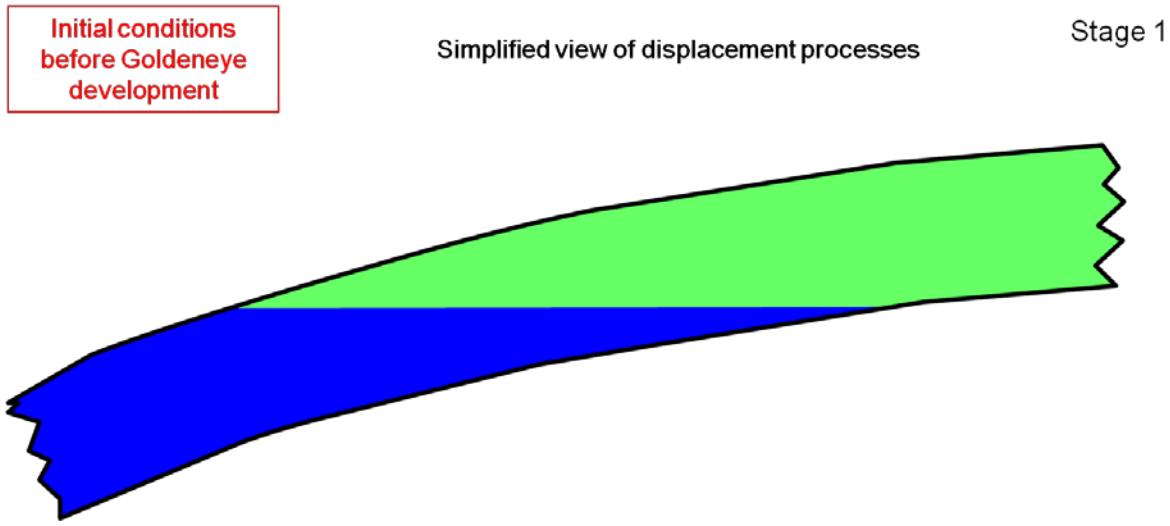

Fig. 2.1— Initial reservoir conditions before hydrocarbon gas production in Goldeneye

During depletion, the aquifer invades the original gas column, leading to trapped gas saturation on the primary imbibition cycle for water. The poorer quality Captain E unit at the top of the reservoir may only be partially invaded by the aquifer, if the vertical connectivity is not sufficiently high to allow this to be swept, **Fig. 2.2**.

[1] FFM Dynamic Model Report, PCCS-05-PT-ZR-3323-00002, KKD no. 11.122.

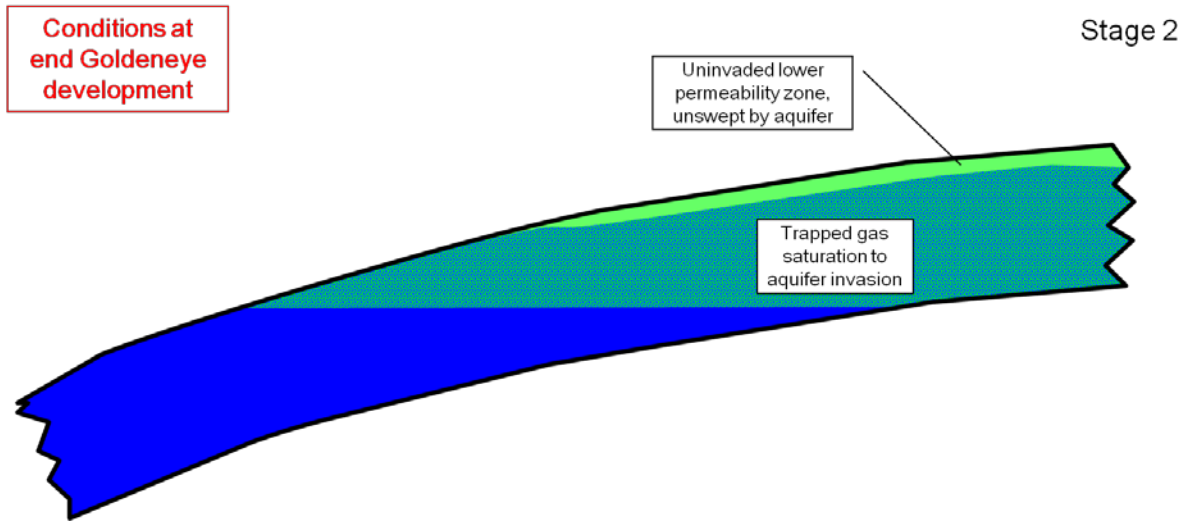

Fig. 2.2—Distribution of saturation at end of Goldeneye hydrocarbon gas production

The distribution of fluids during CO_2injection is shown schematically in **Fig. 2.3**.

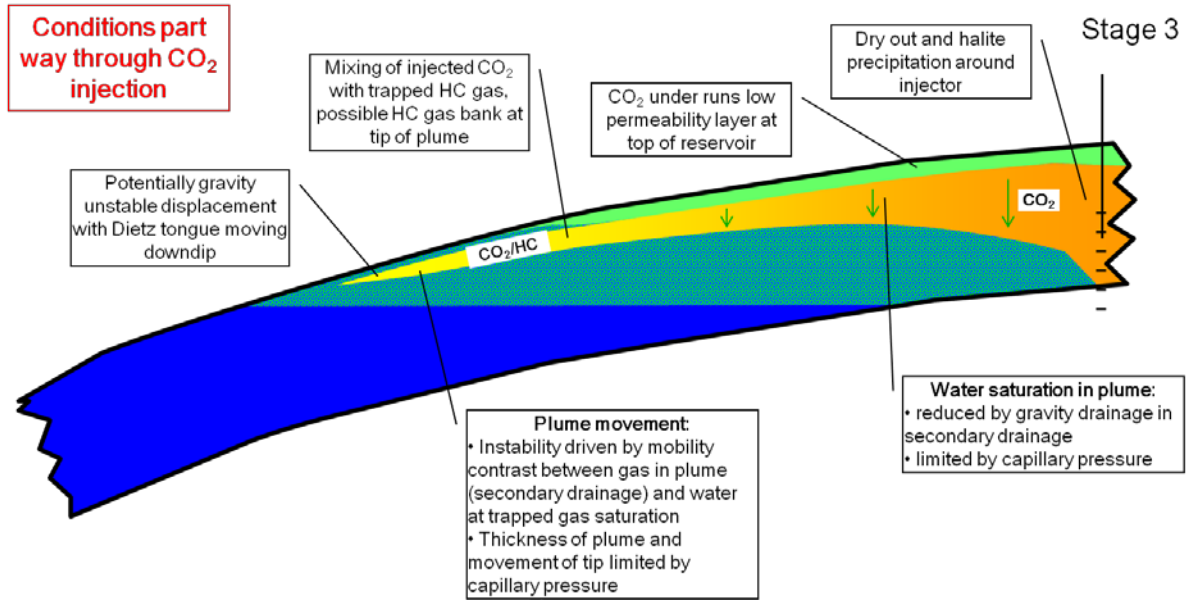

Fig. 2.3—Distribution of fluid during CO_2 injection in Goldeneye

The overall displacement will be dominated by gravity forces, with CO_2 overrunning in the high permeability aquifer invaded Captain D Sand. The shallow dip of the reservoir means that the displacement of brine by CO_2 in the hydrocarbon column is potentially an unstable displacement, with a Dietz Tongue moving downdip. This instability is driven by the mobility contrast between the gas in the plume and the brine at trapped gas saturation, which at the time of the formulation of the SCAL programme was estimated to be in the range 25 to 100 (for the range of reservoir pressures through the Goldeneye injection period and allowing for uncertainty in the end point relative permeabilities). This is compared to a mobility ratio of less than 1 for a stable displacement. The key driver from a SCAL perspective for the displacement is therefore the gas relative permeability within the plume and the water mobility at trapped gas saturation. The minimum thickness of the plume tip

will be limited by the gas/water capillary pressure on the secondary drainage cycle. Towards the front of the plume there will be mixing of the injected CO_2 with the trapped hydrocarbon gas, with the potential for the formation of a hydrocarbon gas bank at the tip of the plume (because of the favourable mobility ratio for CO_2 displacing hydrocarbon gas).

Within the plume itself water will drain vertically under the influence of gravity (secondary drainage process), so that much lower water saturations will be achieved than would be the case in a viscous dominated displacement. The remaining water saturation will affect the size of the plume, both by occupying pore space and through the reduction of the CO_2 relative permeability. At the injector there will be zone of dry out and the potential for halite precipitation.

At the end of the period of CO_2 injection, **Fig. 2.4,** the gas plume may have moved below the original hydrocarbon-water contact, under a primary drainage displacement. Since there is no gas trapped below the contact, the adverse mobility ratio between the water and the displacing gas in the plume will be lower than in the original hydrocarbon column, so the drivers for Dietz unstable movement of the plume will be reduced. At injectors, if there are periods of significant shut-in, brine may partially resaturate the near wellbore area, subsequent CO_2 injection could then increase the levels of possible halite deposition.

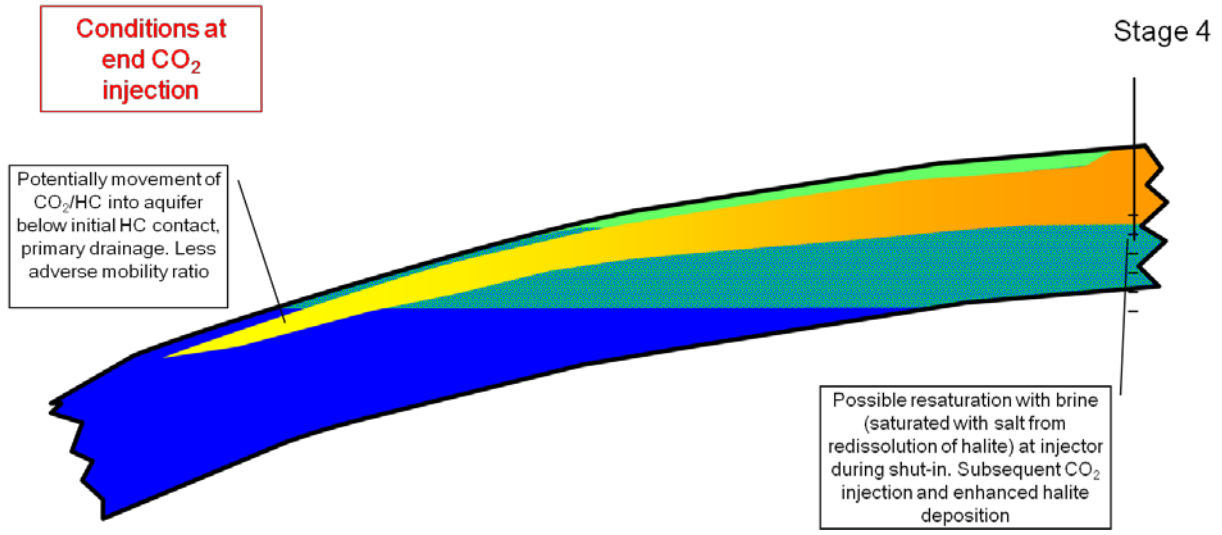

Fig. 2.4—Distribution of fluid at end of CO_2 injection in Goldeneye

After CO_2 injection has finished, the displacement is dominated by gravity forces which act to move the reservoir back to an equilibrium condition, **Fig. 2.5,** ultimately with a flat gas water contact. CO_2 that invaded the aquifer will move back within the original hydrocarbon column, leaving trapped CO_2/HC gas in the aquifer on a primary imbibition cycle, and retrapped gas within the original hydrocarbon column on a secondary imbibition cycle. The density contrast between CO_2 and HC gas may lead to the formation of a HC rich gas cap at the crest of the field, and depending on the connectivity of the Captain E Sand, the cap rock may become exposed to CO_2 saturated brine. The final distribution of water within the equilibrium gas cap will be determined by the secondary drainage capillary pressure.

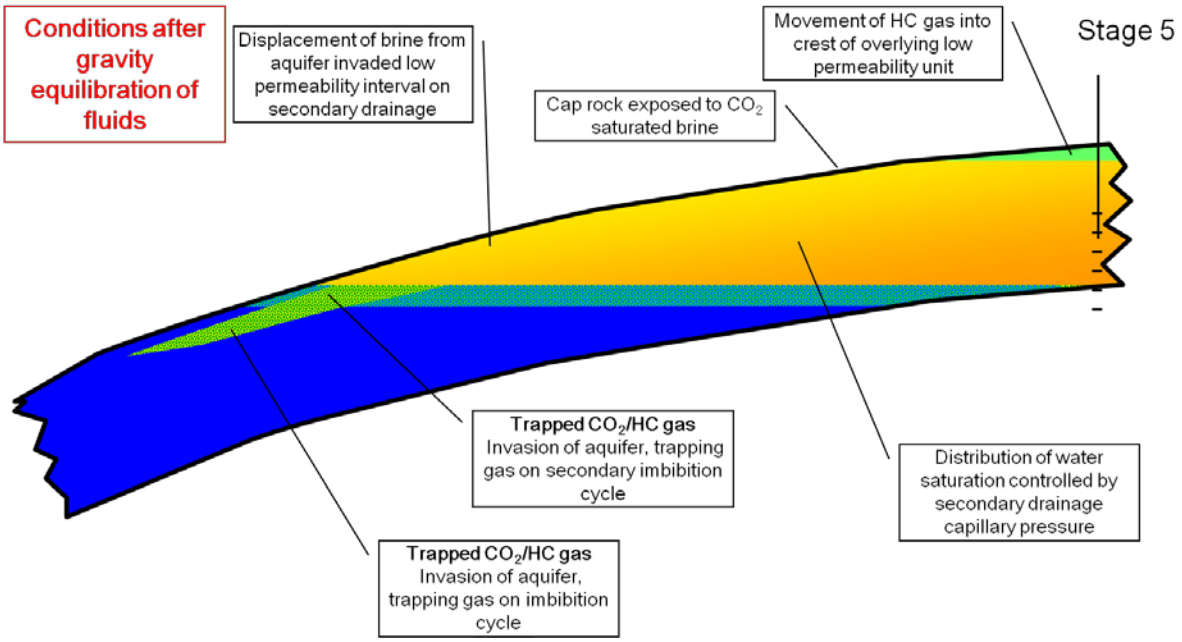

Fig. 2.5—Long term distribution of fluid after CO_2 injection in Goldeneye completed

Injected CO_2 that moves into the aquifer may encounter a local spill point that allows some HC gas/CO_2 to move updip away from the Goldeneye reservoir, **Fig. 2.6**. The movement of HC gas/CO_2 away from the Goldeneye structure beyond local spill point is controlled by conventional mechanisms that apply to saline aquifer storage:

- The plume movement is driven by a primary drainage process limited by gravity forces (movement of the plume being more rapid in high permeability reservoirs with significant dip)
- The relative permeability and capillary pressures relevant to this displacement are the same as those already included in the reservoir sequence for CO_2 moving below the original hydrocarbon contact in stage 4
- The initial immobilisation of CO_2 as the plume moves updip after the end of injection is through capillary trapping at the trailing edge of plume, this is covered by the mechanisms already included in the reservoir sequence for CO_2 retreating from the aquifer zone back into reservoir, stage 5
- The plume continues to move updip until all the CO_2 becomes capillary trapped or free CO_2 is left contained by local structural traps

Subsequent assessment work has shown that for the required storage volumes of 10 or 20 million tonnes CO_2 no scenario has been found in which CO_2 egresses under a local spill point. The present analysis shows that even if this were to occur, data gathered to describe the invasion of the water leg below the original hydrocarbon column in stage 4 and 5 will be sufficient to characterise this process.

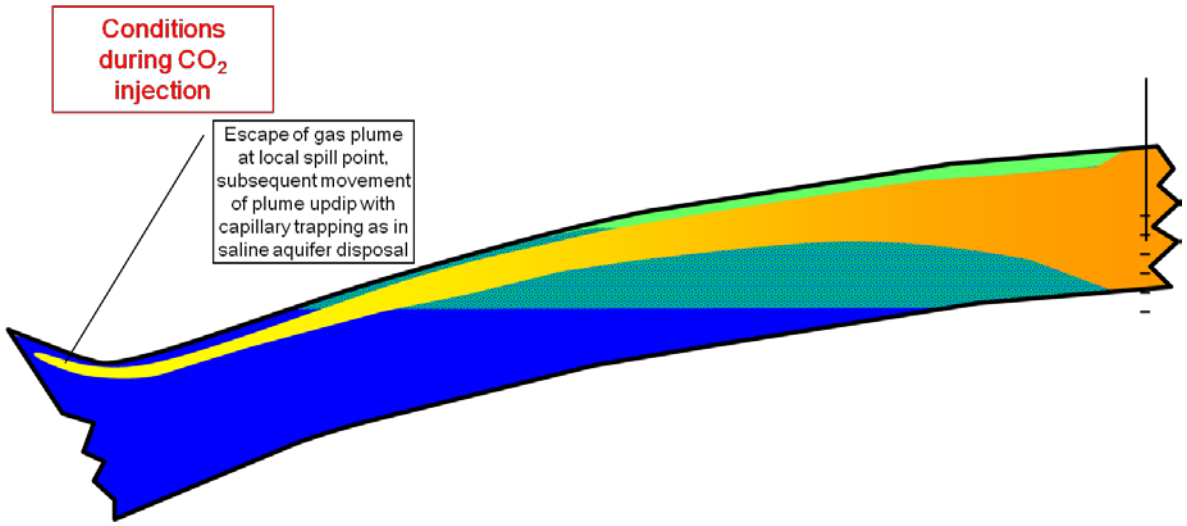

Fig. 2.6—Possible egression of CO_2 from local spill point

The displacement processes are further complicated by the presence of an oil rim and through condensate drop out during depletion, **Fig. 2.7** and **Fig. 2.8:**

- Goldeneye fluid has a low condensate gas ratio (CGR) near the dew point at the original reservoir pressure. Production of neighbouring fields caused pressure depletion in Goldeneye prior to first gas production and potentially dropped out very low saturations of condensate liquid in the reservoir. The ongoing pressure depletion during Goldeneye production will have increased the level of condensate drop out. In principle, polar components in the condensate liquid have the potential for wettability alteration.
- The original gas column was underlain by a thin (~30 ft [~9.14 m]) oil leg. Pre-production pressure depletion and the subsequent significant aquifer influx when Goldeneye was produced, will have pushed the oil rim into the original gas column. As the aquifer invades the gas column, the initial trapping of gas will be by oil,. This is because mobile oil is pushed ahead of the water, until all the mobile oil becomes immobilised as residual oil to water imbibition at the trapped gas saturation. The presence of oil in the gas column may also alter wettability, although the extent of the invaded region is only estimated to be in the range 10 to 35% of the original gas leg volume (depending on the assumptions made about remaining oil saturations in the rim and the impact of trapped gas reducing the residual oil saturation to water imbibition in the gas column.)
- Under CO_2 injection a further set of displacement processes can occur through immiscible/miscible displacement of condensate and oil by the injected CO_2 and CO_2/HC gas mixture at the plume tip. This may lead to the formation of a local oil rim under the invading gas plume through gravity drainage mechanisms, as seen in the box model used as part of the dynamic modelling work to investigate displacement physics[2].

[2] PCCS-05-PT-ZR-3323-00002 – FFM Dynamic Model Report for Goldeneye Project, KKD no. 11.122.

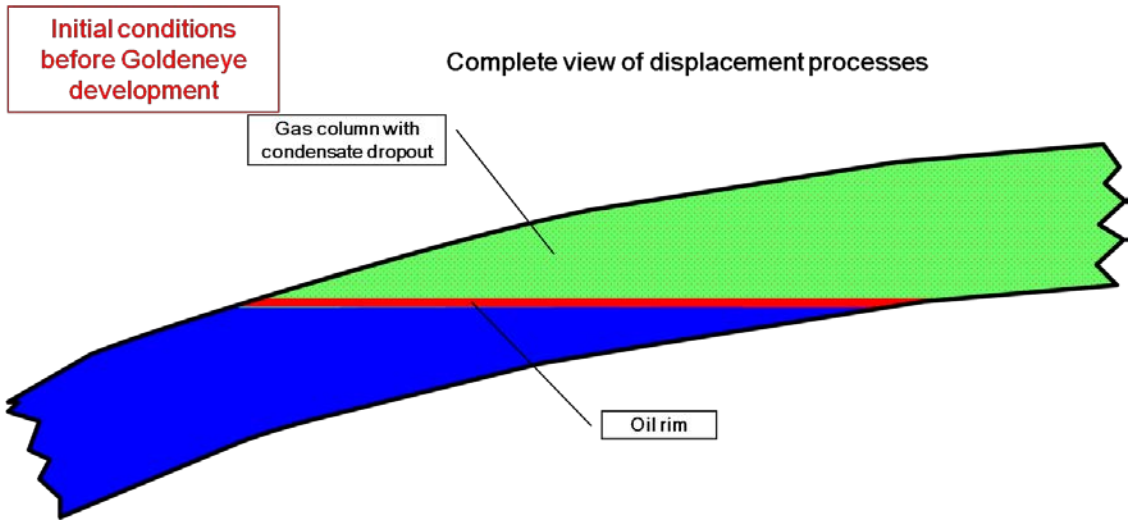

Fig. 2.7—Initial distribution of fluid including oil rim and condensate dropout

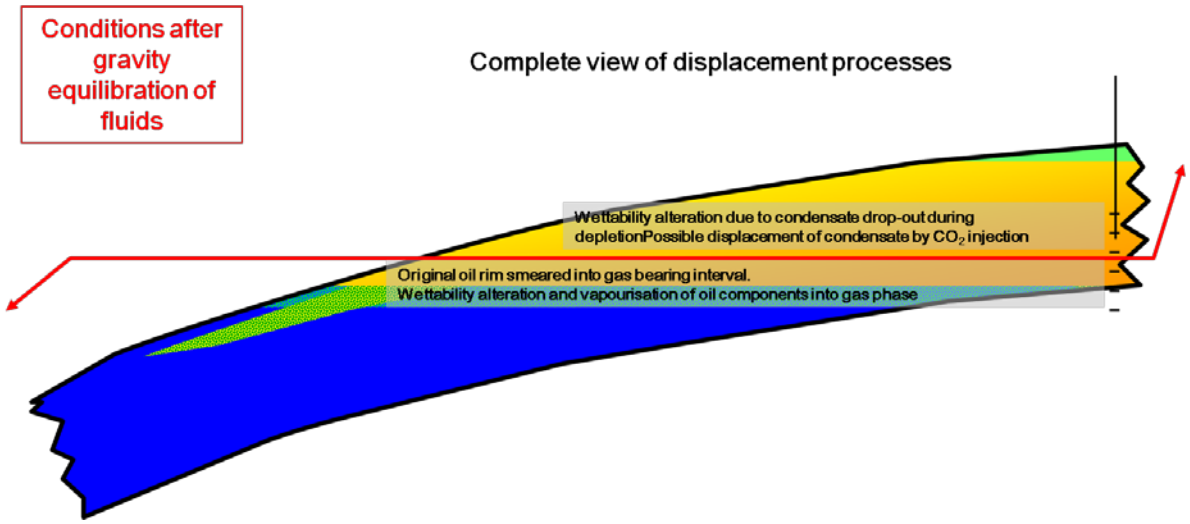

Fig. 2.8—Potential for wettability alteration from smeared oil rim and condensate dropout

3. Existing SCAL data

In this section the existing SCAL data is described and reviewed. This provided the initial ranges to be used when developing the history matched FFM of the existing reservoir performance under depletion. Data from two SCAL studies was reviewed:

Well 14/29a-3 and 14/29a-5

- Third Party study for Shell
- Steady State (SS) imbibition gas/water relative permeability

Well 20/4b-6

- Third Party study for Amerada Hess
- Wettability (well encountered oil rim)
- SS imbibition gas/oil, SS drainage gas/oil, SS imbibition water/oil

3.1. Well 14/29a-3 and 14/29a-5

3.1.1. Overview

The reservoir coverage in the seven core plugs used in this study is summarised in **Table 3.1**.

Table 3.1—Core coverage for SCAL study of wells 14/29A-3 and 14/29A-5

Sample	Reservoir interval	Porosity %	Brine Permeability (md)
S1A, Well A-3	Captain D Plug associated with thin shaly interval	18.2	1.7
S2A, Well A-3	Captain D Plug associated with thin shaly interval	27.3	111
S3A, Well A-3	Captain D	25.0	792
S4A, Well A-5	Captain D	27.8	688
S5A, Well A-5	Captain D	28.3	1224
S7, Well A-5	Captain E	26.2	28.4
S47, Well A-5	Captain C	23.3	27

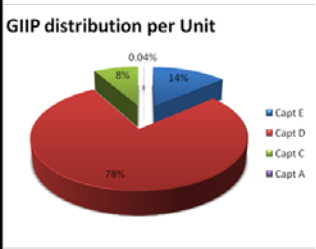

Captain D is the dominant unit in the Goldeneye field, comprising some 78% of the gas initially in place (GIIP). Five of the core plugs are taken from Captain D, however two of these are from thin shaley intervals, not representative of the bulk of Captain D. Therefore, only three of the plugs S3A, S4A and S5A from the seven are representative of Captain D, as shown by the green entries in Table 3.1. The SCAL procedure was as follows:

- Core plugs cut using synthetic formation brine
- Flow through cleaning with toluene and methanol
- Helium porosity
- Air permeability
- Saturate plugs with synthetic formation water (doped with sodium iodide for subsequent X-ray saturation monitoring)

- Drain plugs on porous plate to achieve initial water saturation (S_{wi}) based on applied displacing phase pressure of 64 psig [441.26 KPa] (S5A and S 47) or 128 psig [882.53 KPa](S1A, S2A, S3A, S4A and S7)
- SS water-gas imbibition floods with X-ray saturation monitoring

Review of the results show that the porous plate method used to establish S_{wi} did not achieve the low values of initial water saturation determined from the logs. **Table 3.2** shows the comparison between the initial water saturation achieved in the SCAL study with log derived values for the representative Captain D samples. The higher initial water saturation may result from insufficient capillary contact between the plugs and the porous plate, or because there was insufficient drainage time. The higher S_{wi} would be expected to give trapped gas saturations that are lower than would be found in the reservoir.

Table 3.2—Comparison with initial water saturation achieved in SCAL study for Well 14/29a-3 with log derived values

Sample	Brine Permeability (md)	Log determined S_{wi}	Plug S_{wi}
S3A, Well A-3	688	4.7%	20.7%
S3A, Well A-5	792	9.1%	20%
S5A, Well A-5	1224	6.2%	14.1%

3.1.2. Laboratory artefacts

Trapped gas saturation measurements are subject to a number of potential laboratory artefacts. The choice of SS procedures in the test sequence reported here increases the likelihood of artefacts, compared to the use of limited throughput USS imbibition water floods to determine trapped gas saturation (the highly favourable mobility ratio for water displacing gas making relative permeability data from intermediate saturations irrelevant, since these lie below the Buckley Leverett shock front).

- Large fluid throughput may lead to loss of gas from the core as it dissolves in the brine and a consequential understatement of trapped gas saturation. This is a particular issue for the final stage of the SS test sequence when just flowing brine, with the risk of progressive stripping of gas from near the inlet, dependent on total throughput and the extent to which the injected brine and gas were saturated and humidified respectively
- Higher pressure drops are expected at trapped gas saturation which may lead to reduction in trapped gas saturation because of compression, depending on the operating pressure of the test. The mobility reduced by up to factor ~1000 flowing 100% gas vs. 100% brine depending on the operating pressure for the test. The quoted gas density corresponds to N_2 at standard conditions, and it is possible that the flood was not operated at a sufficiently high pressure to minimise compressibility effects. This is more of an issue for low permeability plugs, but these are from units with a smaller contribution to GIIP

No flow rate or total throughput volumes are reported so it is not possible to assess how important these issues may be. However, all these issues are expected to reduce reported trapped gas saturation relative to values that would apply in the reservoir.

3.1.3. Captain D

Fig. 3.1 shows the in-situ saturation data for the plugs that are representative of the good quality Captain D unit. The data shows the initial water saturation distribution in the plug, with successive SS conditions for increasing water fractional flows, with the final curve corresponding to the situation after 100% water injection. The saturation profiles shown are the final profiles at the end of each different fractional flow period.

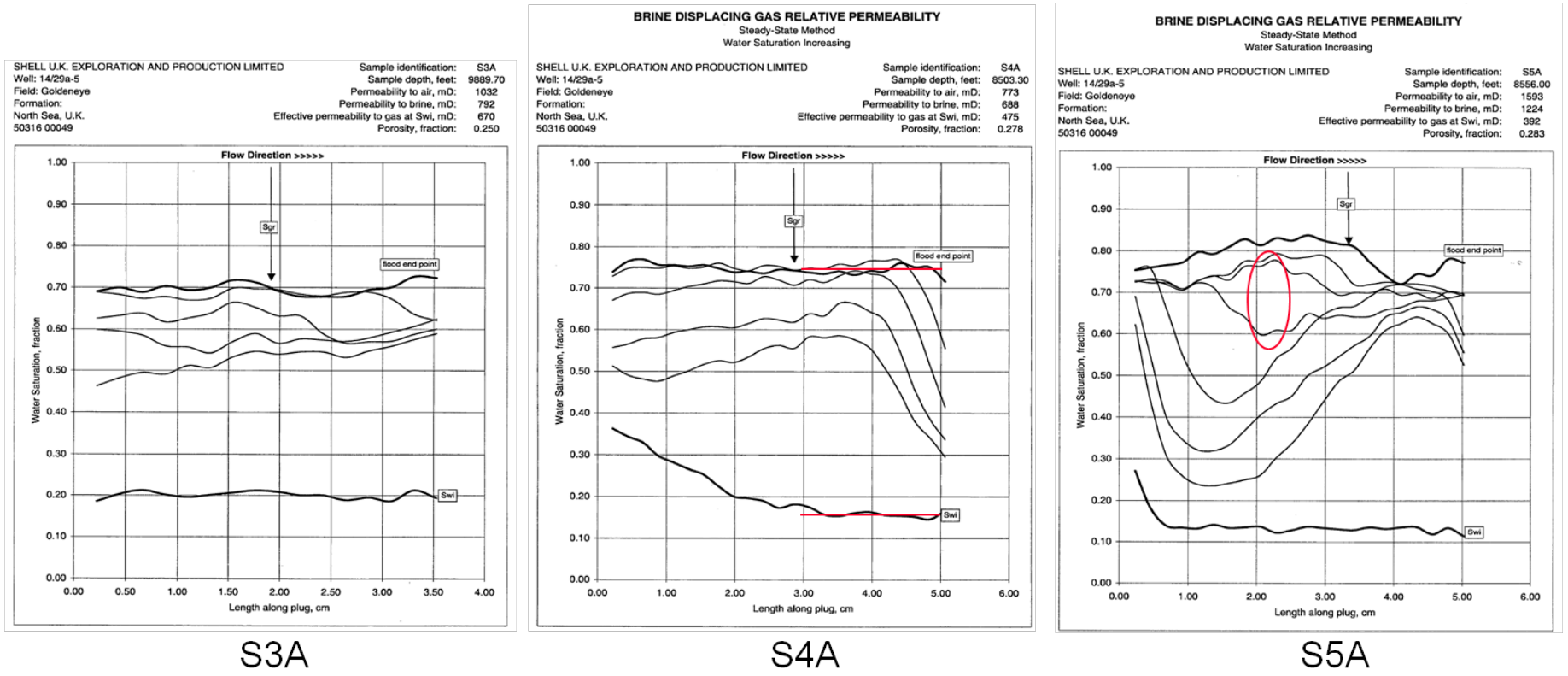

Fig. 3.1—In-situ saturation data for SS gas/water imbibition floods in representative Captain D plugs

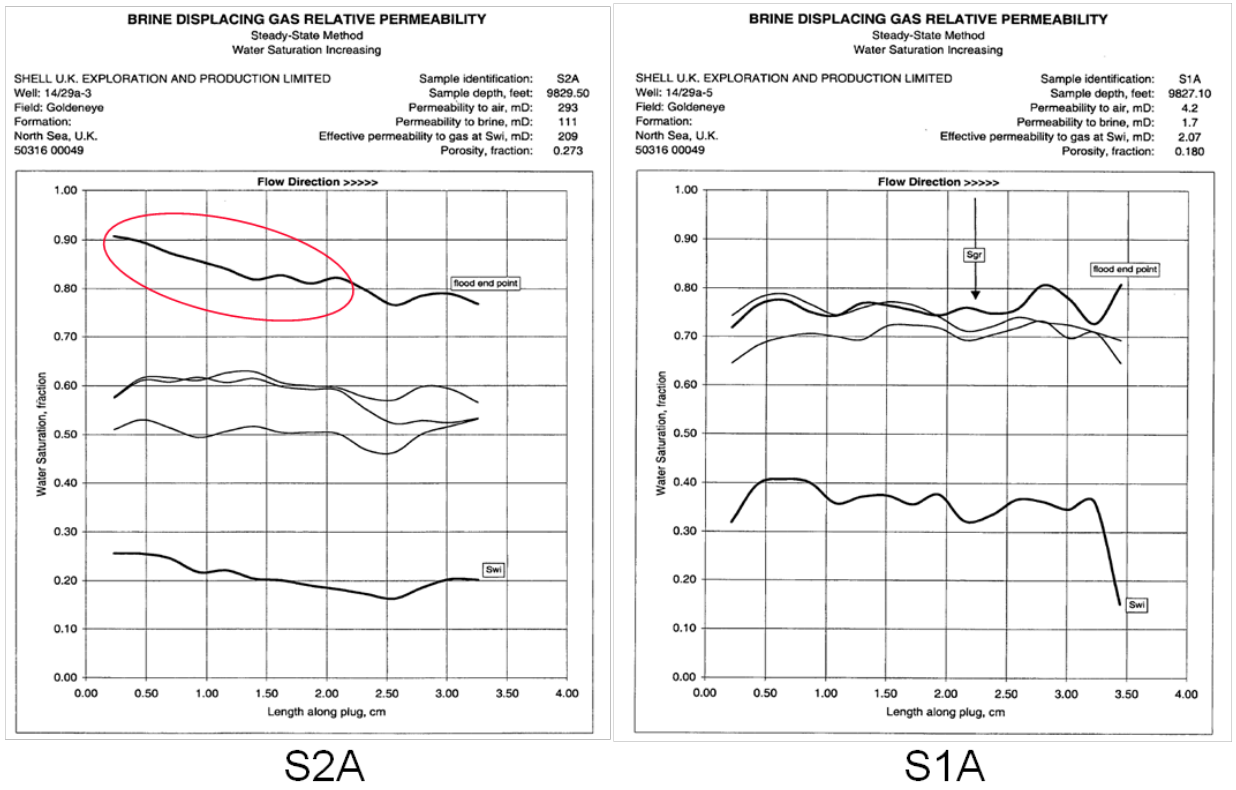

Fig. 3.2—In-situ saturation data for SS gas/water imbibition floods in other Captain D plugs

Plug S3A shows uniform initial water saturation and monotonically increasing water saturations at each position as the water fractional flow is increased through the different SS floods, until a uniform trapped gas saturation of 30% is obtained. Note that because of the highly favourable mobility ratio of the displacement, the penultimate water fractional flow of 0.1275 is sufficient to approach trapped gas saturation ($S_{gt)}$ within saturation measurement accuracy.

Plug S4A shows a non-uniform initial water saturation, which decreases towards the core outlet, although the final 2 cm of the core does have a uniform water saturation of 16% (shown by red line). The water saturation increases monotonically at each position as the water fractional flow is increased through the different SS floods. As was found for S3A, the penultimate water fractional flow, in this case 0.077, is sufficient to approach S_{gt} within saturation measurement accuracy. Over the outlet section of the plug with the uniform initial water saturation of 16% there is a corresponding trapped gas saturation of 25%. However, the trapped gas saturation is also uniform along the entire length of the plug, so in this case there is no strong dependence of trapped gas saturation over initial water saturations in the range 16% to 35%. If this were a general result, any concerns over the impact of higher laboratory initial water saturations compared to field values would be reduced. The most consistent data from this plug is taken to be an initial water saturation of 16% and a trapped gas saturation of 25%.

Plug S5A shows uniform initial water saturations (apart from a very short interval at the beginning of the core). Subsequent profiles for the equilibrium saturation distribution at the end of each fractional flow show unexpected variations. The water saturation does not increase monotonically with increased water fractional flow, as would be expected, and there is a very significant hump in the gas saturation profile in the inlet half of the plug. The results from this plug are considered to be less reliable, although trapped gas saturations are not too dissimilar from S3A and S4A. In the repeat measurements on S5A reported in Section 6.1, no anomalous behaviour was observed and a trapped gas saturation of 30% was measured.

Profiles for the other Captain D samples (from the shaley intervals) are shown in **Fig. 3.2**. Both plugs show relatively uniform initial water saturations, with a significantly higher initial water saturation in the tighter S1A plug. The decreasing trapped gas saturation at the inlet of S2A could result from stripping/compressibility effects, however these indications are not found in S1A. The most representative trapped gas saturation from this latter plug is taken as 22%.

3.1.4. Captain C and E

Fig. 3.3 shows saturation profiles for the Captain C and E samples. Both plugs show relatively uniform initial water saturations. The decreasing trapped gas saturation at the inlet of S7 is very similar to the behaviour in S2A. In this case, based on the behaviour of plugs S3A and S4A, the penultimate water fraction flow of 0.1275 would be expected to be the trapped gas saturation within saturation measurement accuracy. This suggests that the reduction at the inlet could result from stripping/compressibility effects, and that a more representative figure for trapped gas would be 28%, based on the saturation for the average of the saturation profile for the penultimate fractional flow. Plug S47 shows significant variation in trapped gas saturation, including some very low values towards the outlet of the core, which would be at variance with values from the published literature.

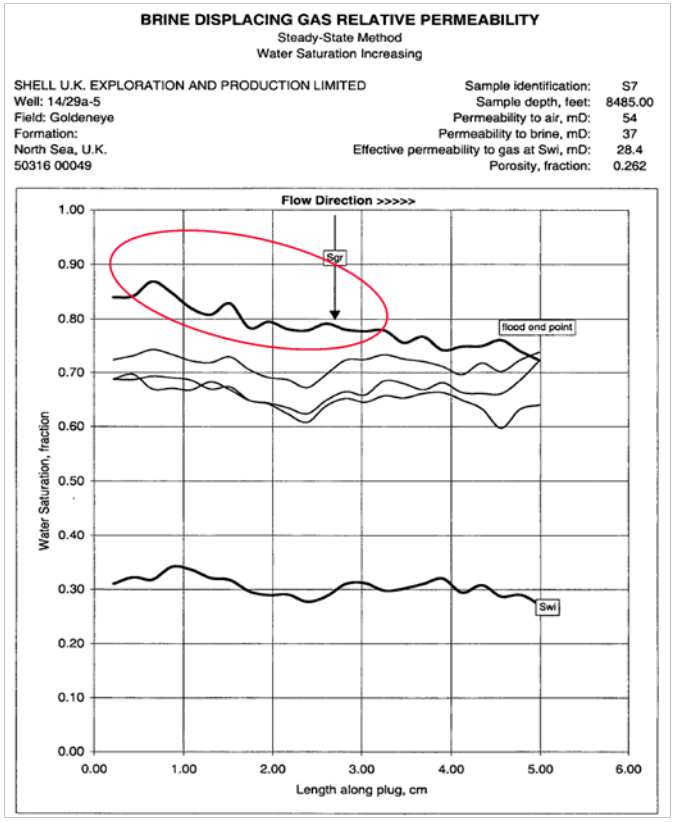

S7

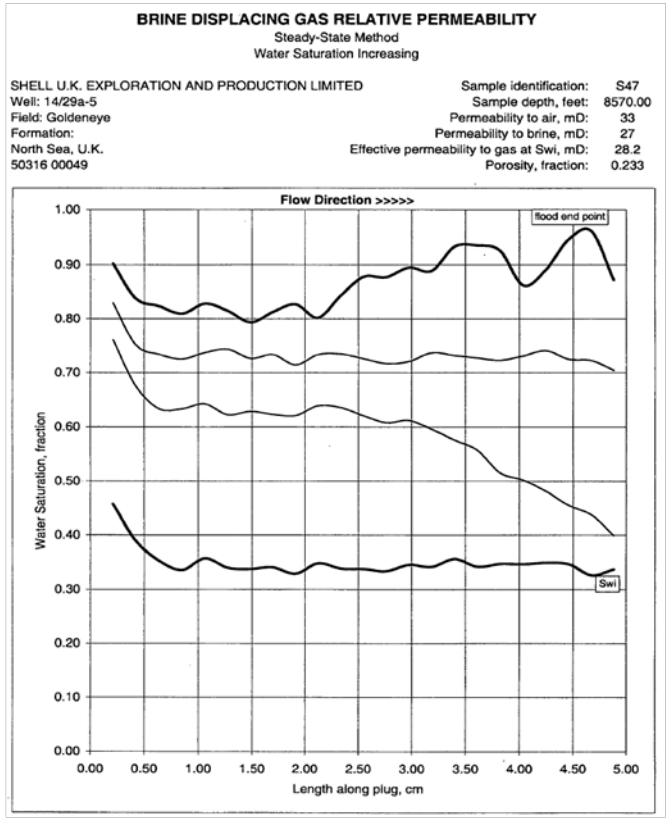

S47

Fig. 3.3—In-situ saturation data for SS gas/water imbibition floods in Captain C and E plugs

3.1.5. Conclusions

The original data (average saturation data along the full core plug) and the corrected data where adjustment is justified by the in-situ saturation profiles are shown in **Fig. 3.4**, which plots trapped gas saturation against initial gas saturation. For the representative Captain D samples this shows that trapped gas saturation is between 25 and 30%, with no clear dependence on initial gas saturation. Initial gas saturations in the experiments are 8-16% lower than those observed in the field.

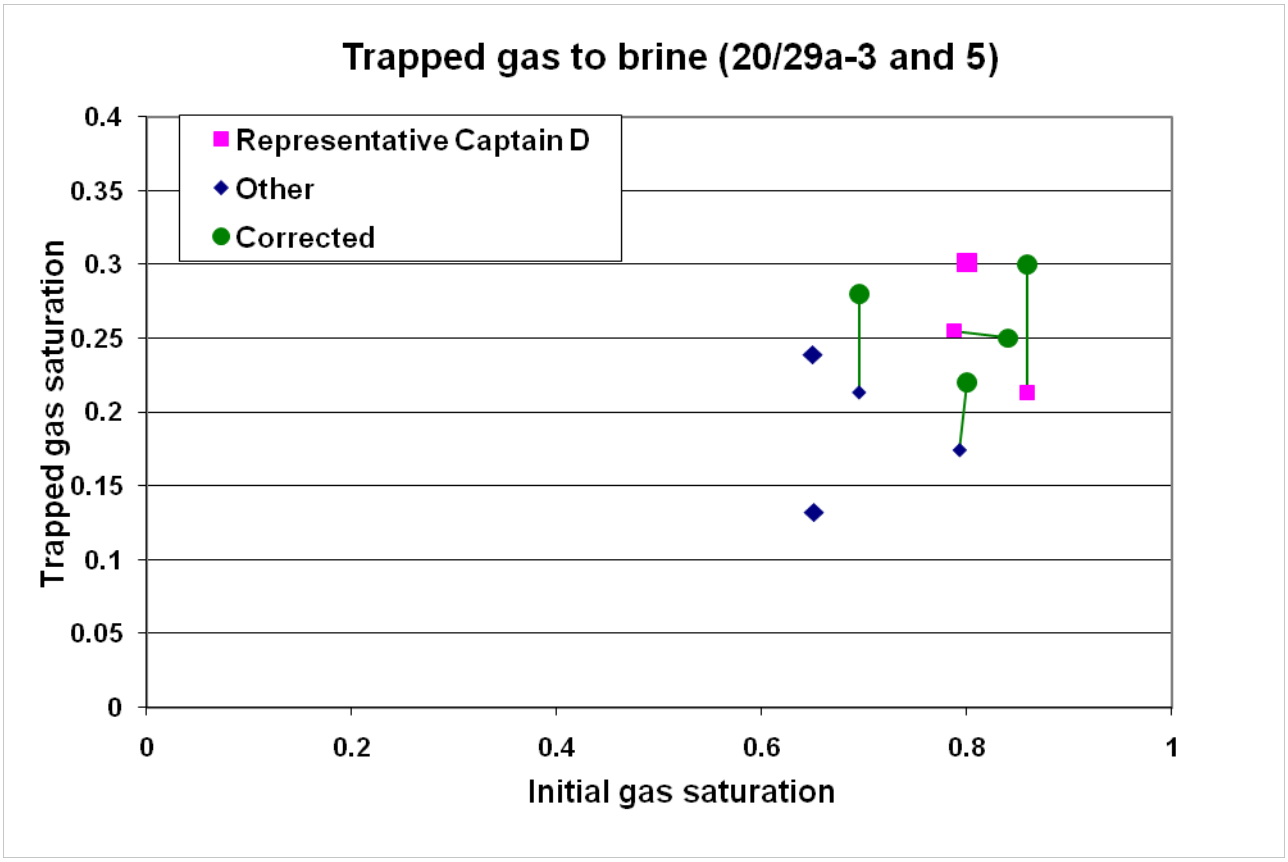

Fig. 3.4—Trapped gas saturation as a function of the initial gas saturation

3.2. Well 20/4b-6

3.2.1. Overview

The reservoir coverage in the four core plugs used for relative permeability measurements in this study is summarised in Table 3.3.

Table 3.3—Core coverage for SCAL study of well 20/4b-6

Sample	Reservoir interval	Porosity %	Air Permeability (md)
11A	Captain E	25.0	215
38A	Captain D	26.8	1168
50A	Captain D	26.4	1412
56A	Captain D	26.3	1451

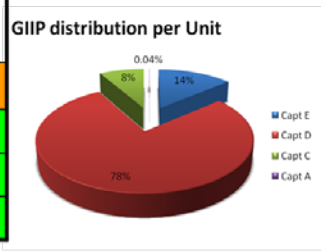

Captain D is the dominant unit in the Goldeneye field, comprising some 78% of the GIIP. Three of the core plugs, 38A, 50A and 56A are taken from Captain D and have representative absolute permeabilities, highlighted as the green entries in **Table 3.1**. The fourth sample, 11A, is from the lower permeability Captain E unit.

Well 20/4b-6 penetrated the oil rim on the southern flank of the Goldeneye reservoir and a different set of procedures was used in the SCAL programme compared to 14/29a-3 and 14/29a-5. Alongside the plugs taken for relative permeability tests, sister plugs were taken for Amott and United States Bureau of Mines (USBM) wettability tests in fresh state core. These showed wettability that was neutral to water wet.

For the plugs taken for relative permeability measurements the following procedures were followed:

- Flow through cleaning with toluene and methanol
- Saturate plugs with synthetic formation water
- Drain plugs on porous plate to achieve S_{wi} based on an applied displacing phase pressure of 180 psig [1241.06 KPa]
- SS oil-gas imbibition floods with X-ray saturation monitoring (oil doped with 20% iododecane to increase the X-ray contrast between phases)
- SS oil-gas drainage floods with X-ray saturation monitoring
- SS water-oil imbibition floods with X-ray saturation monitoring
- X-ray calibration scans for 100% doped oil phase, 100% brine and 100% gas
- Helium porosity
- Air permeability

In this sequence of tests more representative initial water saturations were achieved compared to the plugs from wells 14/29a-3 and 14/29a-5, with values in the range 10 to 13%.

The focus of the data review is the trapped gas saturation to oil in the oil-gas imbibition test. The oil-gas drainage floods are not relevant to any displacement process occurring in Goldeneye during production. The waterflood results are of limited applicability, because the water-oil displacement only applies directly to the limited volume of the original oil rim. The subsequent movement of oil in

the original gas column is a water-oil imbibition process at initial conditions of gas trapped by oil, which is not covered by the reported tests.

The oil gas imbibition tests are subject to the same range of artefacts as already discussed for gas-water imbibition described for wells 14/29a-3 and 14/29a-5. While the gas is stated to be humidified, there is no discussion of any procedures to minimise the stripping of gas in the core by injected oil. As will be seen there is strong evidence for gas stripping having taken place in all of the tests, during the final sequence of 100% oil injection to take the plugs to trapped gas saturation.

3.2.2. Reinterpretation of results

Fig. 3.5 shows the saturation distribution for plugs 50A and 11A. The saturation values shown are the initial water saturation and then the combined total of the initial water saturation and the gas saturation, calculated on the assumption that the initial water present in the core remains immobile during the gas-oil imbibition floods. Initially the core is at a 100% combined saturation of water and gas, as the fractional flow of oil is increased the gas saturation (and the combined gas and initial water saturation) reduces.

The data for each plug shows uniform initial water saturations. Subsequent SS saturation distributions also show uniform character along the length of the plugs, with the exception of the final profile for 100% oil fractional flow. As the oil fractional flow increases the combined saturation of gas and initial brine decreases, the difference between the profile and the initial water saturation representing the gas saturation. The final profile in Plug 50A has an entirely different character, showing no gas present at the inlet of the core, but progressing to a trapped gas saturation of 35% at the outlet of the core (ringed in red) equal to the penultimate fractional flow when gas and oil were still being injected into the core together. This profile is indicative of stripping of the remaining gas saturation in the core by the injected gas. Unfortunately no data is provided on the volumes of oil injected in this final stage of the test or the pressure at which the test was conducted, so it is not possible to further quantify the level of stripping that might be expected. The assertion in the report that theses profiles are the result of "oil fingering through the larger pores in the sample" is not considered to be a plausible explanation, because the displacement is at a favourable mobility ratio and there is no evidence from the preceding profiles for non-uniform saturation distributions along the length of the core. The results for Plug 11A are similar, except in this case the gas saturation has been almost entirely stripped from the core.

The results for Plugs 38A and 56A are shown in **Fig. 3.6.** Similar characteristics are seen compared to Plugs 50A and 11A, with relatively uniform saturation profiles, until the last scan at 100% oil injection, where stripping of gas again is evident. In Plug 38A the gas saturation at the outlet end of the core (highlighted in red) is in agreement with the saturation found in the penultimate profile.

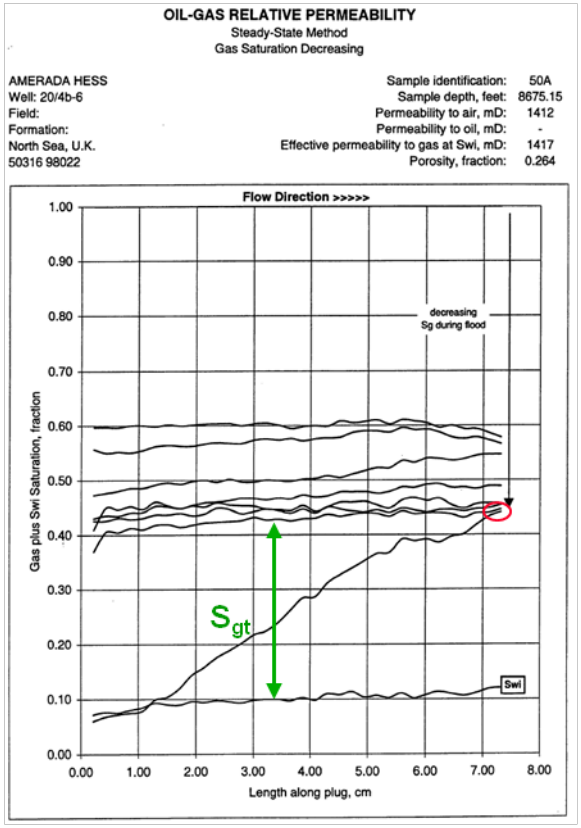

50A

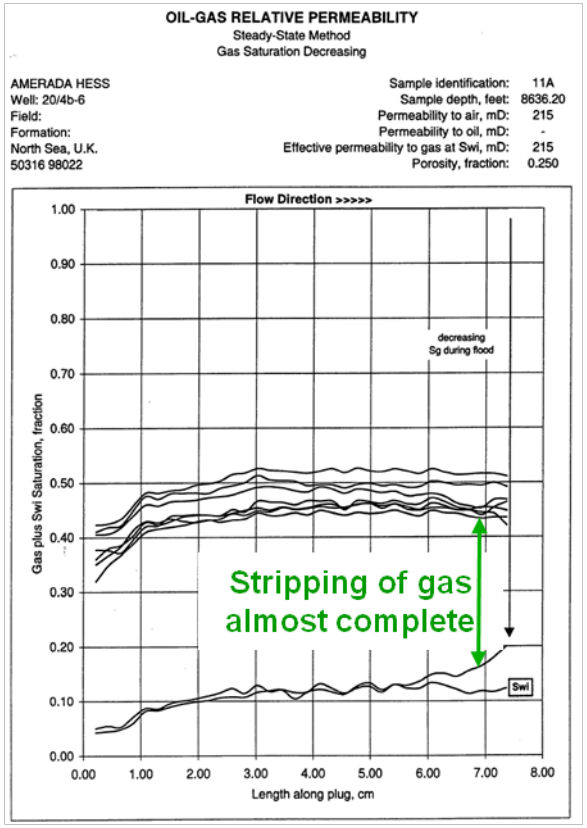

11A

Fig. 3.5—Saturation distribution for oil imbibition tests for plugs 50A and 11A

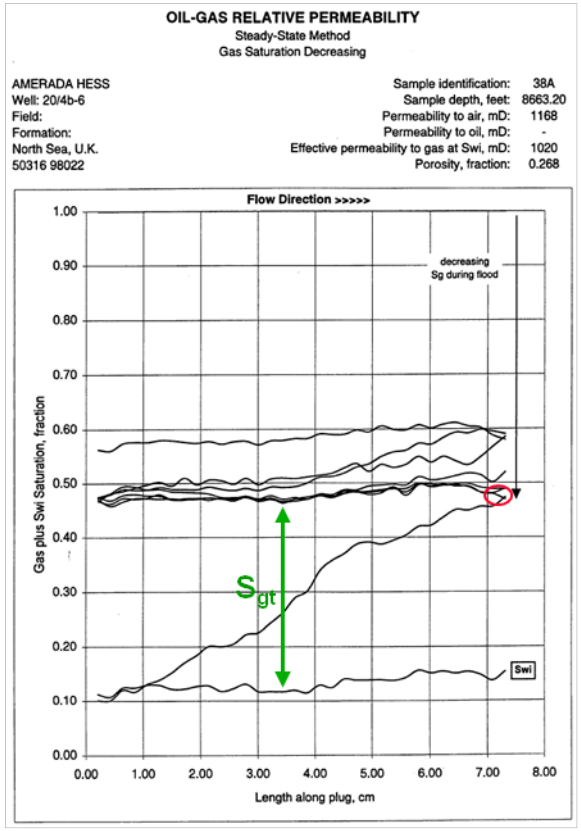

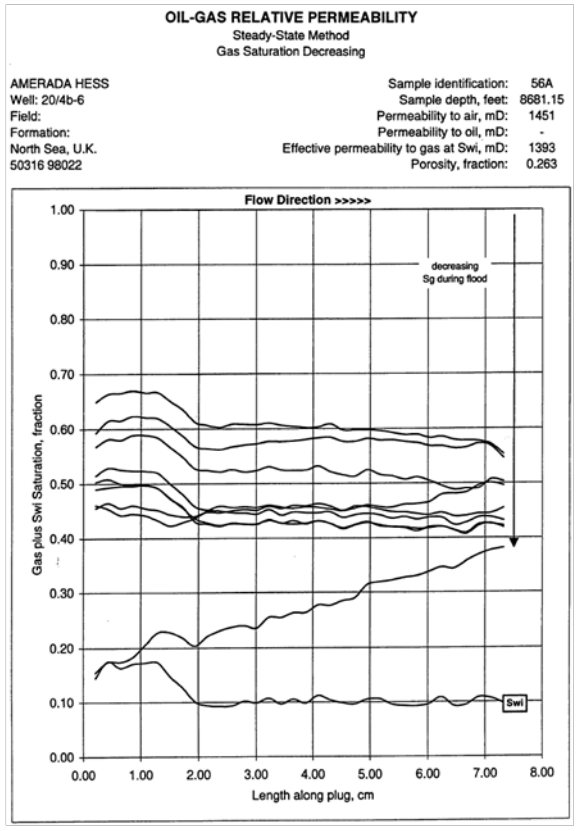

Fig. 3.6—Saturation distribution for oil imbibition tests for plugs 38A and 56A

In the gas-water imbibition study for Well 14/29a-3 and 14/29a-4 it was found that once the imbibing phase (water) fractional flow exceeded 0.1, the trapped gas saturation was approached within experimental error. The viscosity of the oil used in the gas-oil imbibition tests has a viscosity of 1.7 cp, compared to the water viscosity of 1 cp. This suggests that for oil fractional flows greater than 0.2 the saturation profiles should be essentially at the trapped gas saturation (consistent with the agreement of the outlet saturation for the 100% oil fractional flow in Plugs 38A and 50A). The penultimate fractional flows for 11A, 38A, 50A and 56A are 0.894, 0.9, 0.822 and 0.84 respectively, well above this criterion, so that trapped gas saturation can be reliably inferred from the penultimate saturation profile. The inferred trapped gas saturation data is plotted in **Fig. 3.7**, which shows that trapped gas saturations in the range 32 to 35%. For the four plugs available there is a consistent set of data, with no significant dependence on rock type or permeability and with the lower initial water saturations achieved in the plugs being more representative of those observed in the field.

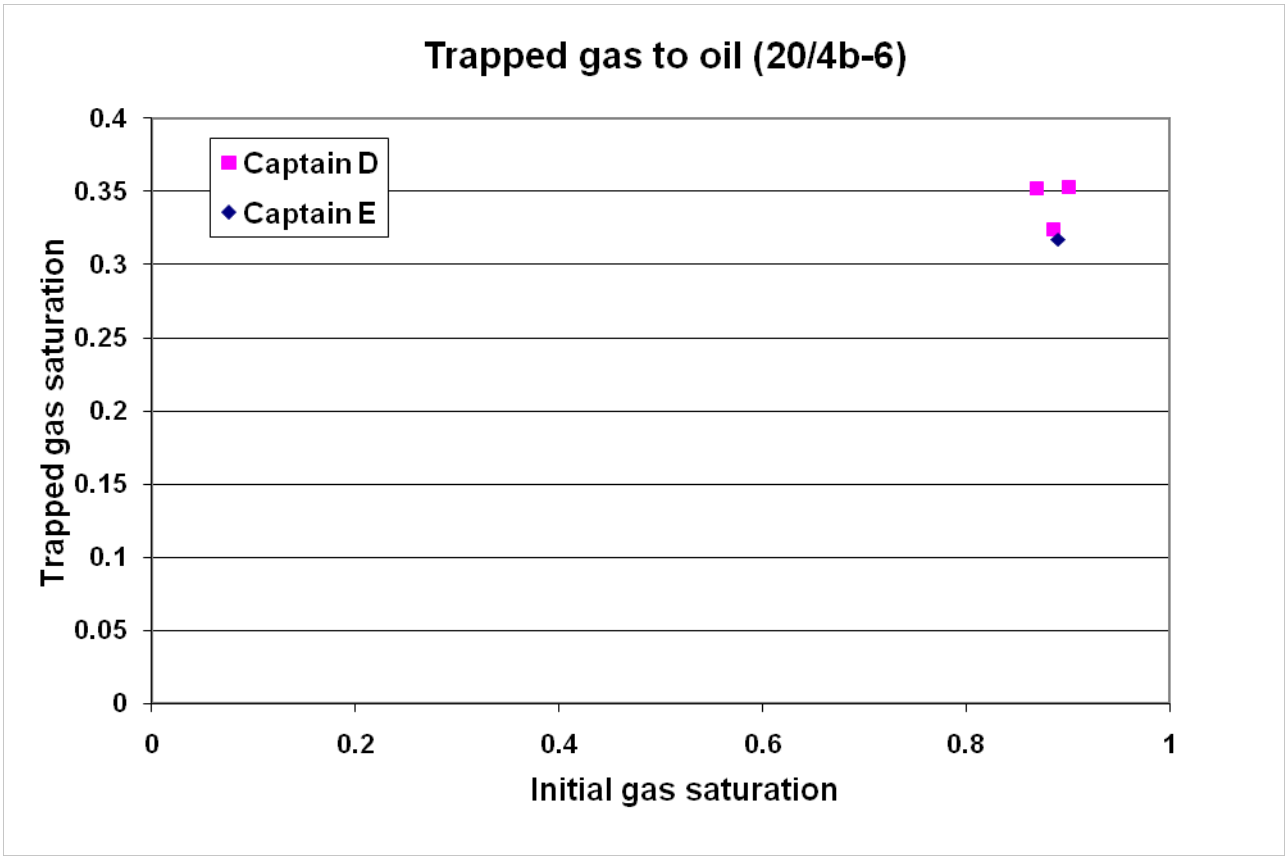

Fig. 3.7—Interpreted trapped gas saturation to oil for well 20/4b-6

3.3. Relative permeability at trapped gas

Sections 3.1 and 4.2 have evaluated data for trapped gas to water and oil imbibition respectively. In this section the results are combined and ranges for use in history matching inferred. To a first approximation trapping of gas to oil and brine is assumed to be similar, given that the gas phase remains the non-wetting phase in both cases.

Fig. 3.8 shows the combined data set.

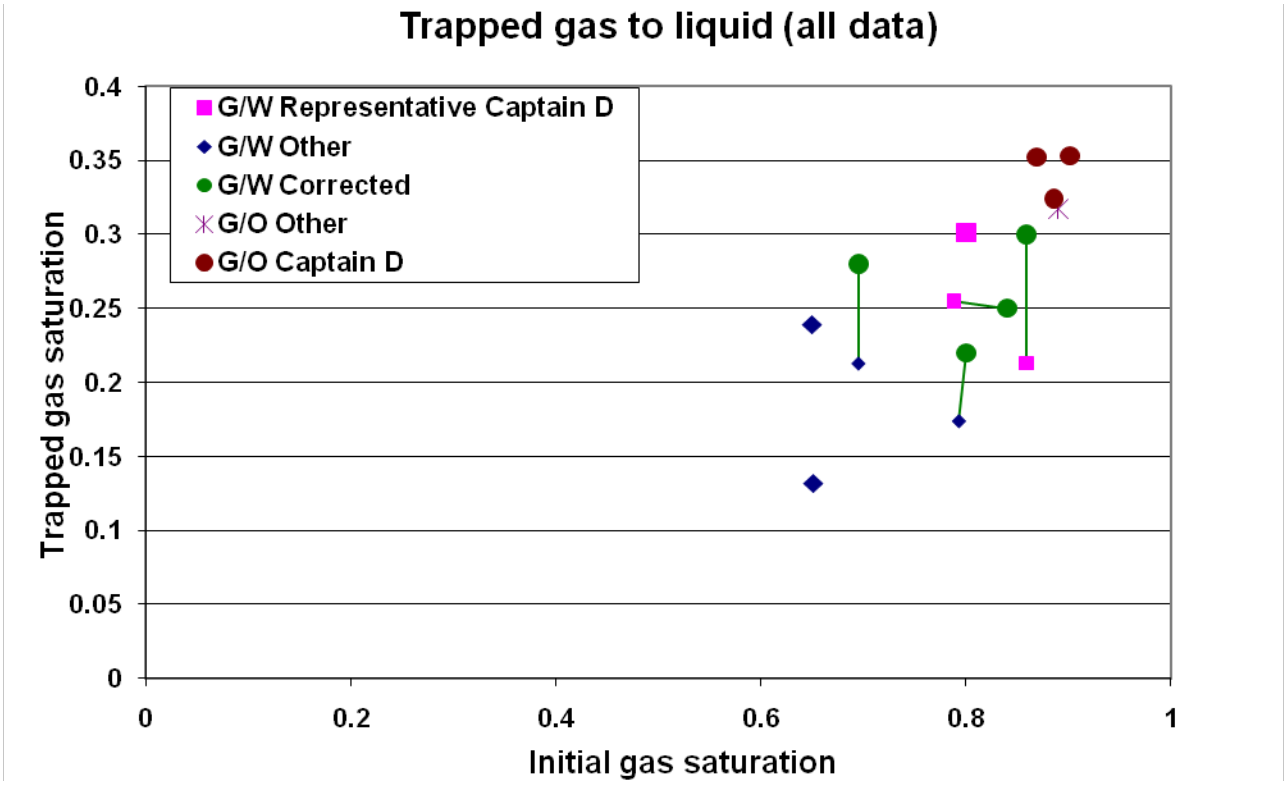

Fig. 3.8—Collation of trapped gas saturation to liquid for all samples

Focusing on the Captain D data (corrected where necessary for the gas-water data) gives **Fig. 3.9.** The Captain D data lies within Land correlations with trapped gas saturations of 25% to 32%-38% at an initial water saturation of 5%.

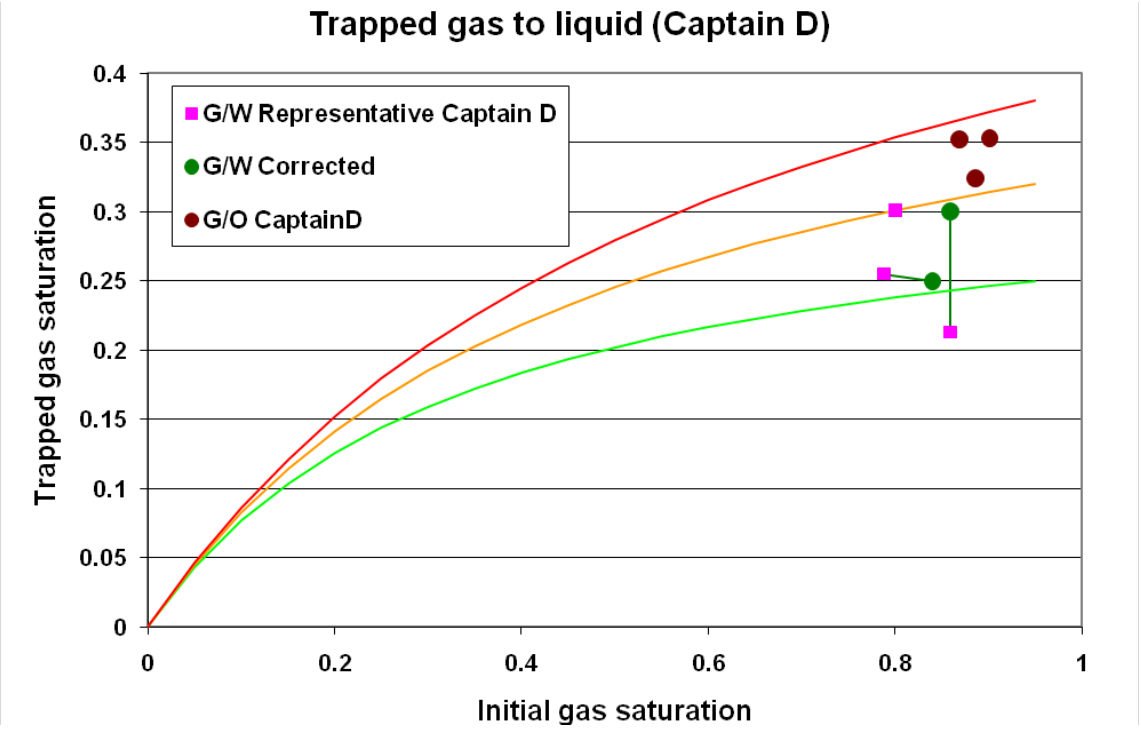

Fig. 3.9—Trapped gas saturation for Captain D, with uncertainty bands using Land's correlation

The liquid permeability at trapped gas saturation is another key variable, controlling the mobility of the encroaching aquifer during the development phase, and the mobility contrast between injected CO_2 and the water that must be pushed out of the reservoir during the storage phase. Fig. 3.10 collates the data for the gas-oil imbibition floods and the gas-water imbibition floods in Captain D. Endpoint relative permeabilities refer to core average data (based on total pressure drop) and so these cannot be updated where saturation data has required an updated estimate of the trapped gas saturation. For the gas-oil data the oil relative permeability has been taken from the penultimate fractional flow stage, which essentially corresponds to the final trapped gas saturation.

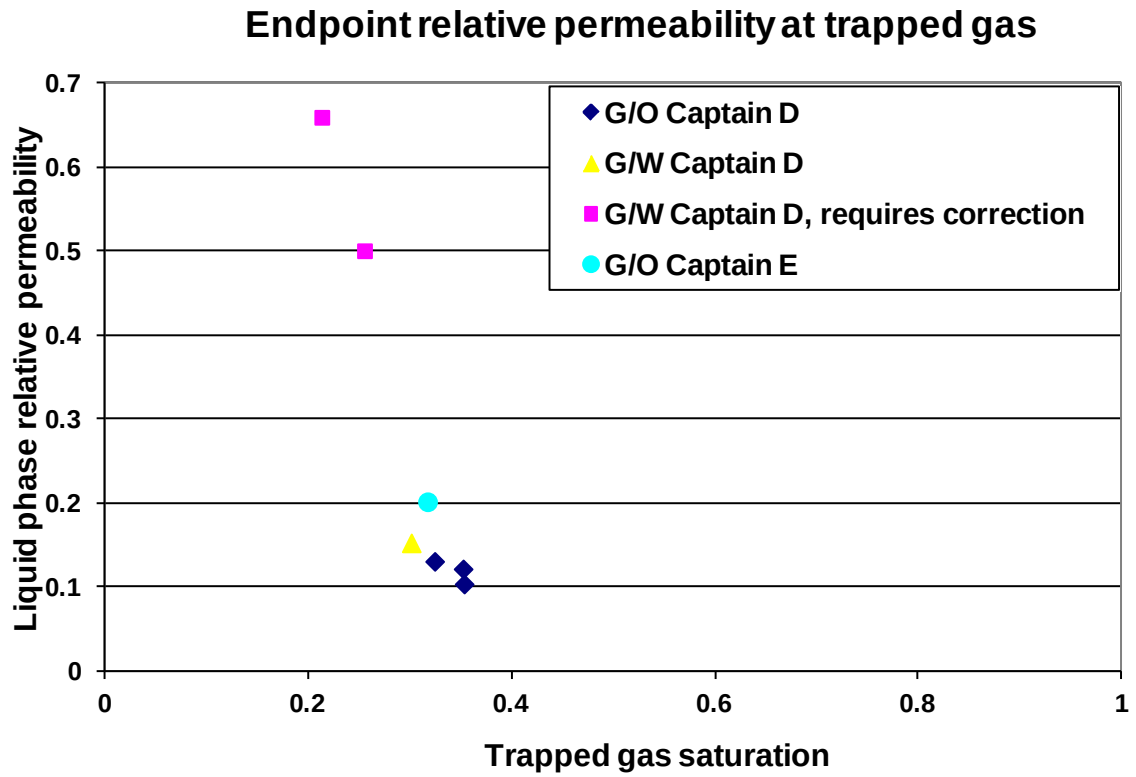

Fig. 3.10—Endpoint liquid relative permeability at trapped gas saturation

Based on data where saturation does not require correction, a range of endpoint relative permeability of 0.05 to 0.25 is supported.

4. Ranking of issues

Section 2 outlined the different mechanisms operating during the full life cycle of Goldeneye reservoir, during the initial hydrocarbon production, through CO_2 injection and ultimately after site closure. These were ranked for their potential impact on injectivity, capacity and containment, **Table 4.1.**

Table 4.1—Ranking of displacement mechanism impact on CO_2 storage injectivity, capacity and containment

Displacement mechanism	Issue	Issue number	Rank	Comment
Aquifer invasion trapping hydrocarbon gas during production phase	Mobility of water that has to be pushed back into aquifer by gas plume.	1	1	Drives maximum plume size and capacity for CO2 storage within given area
	Volume of trapped gas that will mix with CO2 as plume advances, affecting physical properties of gas (reduced viscosity) and increasing volume of gas at reservoir conditions (non-ideal mixing)	2	2	Drives maximum plume size and capacity for CO2 storage within given area
Growth of gas plume in reservoir above the GWC	Mobility of gas in tongue at tip of plume resulting from effective residual water saturation determined by capillary pressure and the water drainage relative permeability.	3	1	Drives maximum plume size and capacity for CO2 storage within given area
	Effect of capillary pressure on limiting minimum gas plume thickness and vertical saturation distribution within plume.	4	1	Drives maximum plume size and capacity for CO2 storage within given area
	Gas present at plume tip may be HC gas (bank pushed ahead of more viscous CO2) or mixed CO2/HC gas composition	5	2	Drives maximum plume size and capacity for CO2 storage within given area
Plume movement within reservoir	Longer term drainage of water towards the base of the plume may increase gas mobility	6	2	Drives maximum plume size and capacity for CO2 storage within given area
	Water draining to plume base creates additional capacity for dense phase CO2 within original reservoir structure	7	2	Drives maximum plume size and capacity for CO2 storage within given area
Growth of gas plume into aquifer (including movement beyond local spill point)	Mobility of gas in tongue at tip of plume resulting from effective residual water saturation determined by capillary pressure and the water drainage relative permeability.	8	1	Drives maximum plume size and capacity for CO2 storage within given area. Movement of CO2 away from reservoir updip of "local" spill point
	Effect of capillary pressure on limiting minimum gas plume thickness and vertical saturation distribution within plume.	9	1	Drives maximum plume size and capacity for CO2 storage within given area. Movement of CO2 away from reservoir updip of "local" spill point. Impacts ability of seismic to image plume in aquifer.
	Gas present at plume tip may be HC gas (bank pushed ahead of more viscous CO2) or mixed CO2/HC gas composition	10	2	Drives maximum plume size and capacity for CO2 storage within given area. Movement of CO2 away from reservoir updip of "local" spill point
Plume retreat in reservoir invaded zone	Mobility of water in reinvaded zone	11	3	Contraction of plume back from maximum extent
	Trapped gas saturation left in reinvaded zone	12	3	Maximum movement of gas away from Goldeneye structure, if gas plume has expanded to local spill point
Plume retreat in aquifer invaded zone and/or movement away from local spill point	As free gas saturation in reservoir equilibrates plume retreats, leaving trapped gas saturation.	13	2	Contraction of plume back from maximum extent
	Trapped gas saturation left in reinvaded zone	14	1	Maximum movement of gas away from Goldeneye structure, if gas plume has expanded to local spill point
Injectivity	Impact of cement dissolution and halite precipitation on injectivity	15	1	
	Effect on matrix of secondary imbibition of water into near well bore region during well shut-in. Possible weakening of matrix through dissolution of calcite cements	16	2	
	Enhanced halite deposition from reinvading brine reducing injectivity	17	1	Reinvading brine will contact halite desposited around injector and potentially become saturated, increasing halite depsoition on subsequent injection
Cap rock integrity	Interaction of CO2 saturated brine with cap rock	18	1	Calcium carbonate component of cap rock may be attacked by CO2 saturated brine

These displacement process issues have been addressed throughout the project work programme through a combination of modelling (including sensitivity analysis), analogue data or laboratory studies.

Issues over halite deposition have been investigated and shown to be of low impact, based on assessment of the levels of potential precipitation and through analogue data from existing CO_2 injection projects at Sleipner and In Salah[3].

Similarly issues of cap rock integrity have been addressed by geochemical modelling[4] and also shown to be of low impact.

The remaining high impact areas are driven by the following:

- The mobility of the water at trapped gas saturation that has to be pushed back into the aquifer by the gas plume
- Mobility of gas within the plume resulting from the remaining water saturation within the plume
- Trapped gas saturation to imbibition by brine
- Effect of capillary pressure and relative permeability on limiting minimum gas plume thickness and vertical saturation distribution within the plume

5. CO_2 storage SCAL programme design

This section describes the SCAL programme designed to address the key displacement issues identified in Section 4.

5.1. Design considerations

The design of the flooding sequence has been driven be a number of considerations to tailor the programme specifically to the needs of Goldeneye CO_2 storage.

1. The displacement mechanism in the reservoir is strongly influenced by gravity. Within the plume the high vertical permeability will lead to the average remaining water saturation being driven by gravity drainage. Appropriate techniques need to be selected to achieve representatively low water saturations and to adequately characterise the water relative permeability.
2. The mobility of the water at trapped gas saturation under current reservoir conditions is driven by conventional hydrocarbon gas trapping, rather than CO_2 trapping mechanisms
3. Displacement processes within the plume in the original HC column take place on a secondary drainage cycle, while the processes are on a primary drainage cycle where the plume has moved below the original hydrocarbon gas column into the aquifer.
4. CO_2 is highly soluble in brine and water can also be vaporised by dry CO_2. Reservoir condition flooding circuits need to be designed to make sure that the CO_2 and brine are kept in equilibrium to minimise artefacts. To this end a rig originally designed for SS tests was selected, in which the brine and CO_2 are held in equilibrium in a pressure-volume-temperature (PVT) cell, which also acts as a separator for the produced fluids. The circuit is a closed system and makes it possible to maintain an overall volume balance in the flooding circuit.

[3] Shell 2013, Well Completion Concept Select Report, Doc No. PCCS-05-PT-ZW-7180-00003. KKD no. 11.097.

[4] Shell 2013, Geochemical Reactivity Report Doc No. PCCS-05-PT-ZR-3323-00001,. KKD no. 11.116.

5. The core plugs from the previous study were available and should be incorporated into some of the test sequences to provide a means of relating new results to the existing data and the interpretation developed in Section 3.
6. Saturation monitoring should be used in all core flooding tests, and this should always be supported by volumetric balances to provide additional quality control (QC).

5.2. Programme Modules

The SCAL Modules developed to address the key data issues taking into account the design considerations of Section 5.1 are summarised in **Table 5.1**. The ticks indicate how the individual stages in the different Modules address the key displacement issues. The individual Modules are discussed in further detail below.

Table 5.1—CO_2 SCAL programme Modules

			Displacement issue			
Laboratory module			Mobility of water to be pushed back into aquifer	Mobility of gas within plume	Trapped gas saturation in zones reinvaded by brine	Capillary pressure and relative permeability control on plume thickness and water distribution
1	**Centrifuge primary drainage to representative pre-production initial water saturations, followed by forced water imbibition**	Primary drainage with multi-stage centrifuge test				✓
		Gas relative permeability at established Swi		✓		
		Trapped gas saturation			✓	
		Water relative permeability at trapped gas	✓			
2	**Centrifuge primary drainage to target Swi followed by forced water imbibition**	Primary drainage with single-stage centrifuge test				✓
		Gas relative permeability at established Swi		✓		
		Trapped gas saturation			✓	
		Water relative permeability at trapped gas	✓			
3	**Porous plate primary drainage followed by water imbibition**	Gas relative permeability at established Swi		✓		
		Trapped gas saturation			✓	
		Water relative permeability at trapped gas	✓			
4	**Reservoir condition CO2 flooding**	CO2 relative permeability at established Swi		✓		
		Trapped CO2 saturation to water imbibition			✓	
		Water relative permeability at trapped CO2 saturation	✓			
		Unsteady state CO2 injection from 100% water saturation		✓		✓
		Trapped CO2 saturation to water imbibition			✓	
		CO2 relative permeability at 100% gas saturation		✓		
5	**Brine CO2 IFT**					✓

5.2.1. Ambient condition tests

The use of a range of methods provides the means to compare different techniques and increases the confidence in the final results.

Module 1

Plugs were "flow through" solvent cleaned, water saturated and their permeability determined.

This module consists of a primary drainage multi-speed gas-water centrifuge test at ambient conditions with the objective of establishing representative initial water saturation and determining the gas water capillary pressure curve. In addition simulation would allow the water relative permeability on primary drainage to be established.

Following completion of the centrifuge test, the plugs are demounted and allowed to equilibrate prior to the flooding part of the module. The gas relative permeability at initial saturation is measured prior to an USS water imbibition flood, injecting water bottoms up at low rate in the vertically mounted core, and operating the flood at sufficient back pressure to minimise the impact of any compressibility effects. The favourable mobility ratio means that the produced fluids are expected initially to be 100% gas production followed by a sharp transition to 100% water production after water breakthrough. The throughput of brine is carefully managed to avoid injecting excess brine beyond that needed to establish the trapped gas saturation, thereby eliminating the risk of stripping gas from the core by the injected brine. The final stage of the test is to determine the water relative permeability at trapped gas saturation.

A sequence of calibration scans at 100% gas and then 100% brine were completed and the brine permeability at 100% brine saturation remeasured. The plug was then dried and the porosity and air permeability determined.

Module 2

This module is similar to module 1, except the initial water saturation is targeted to a value representative of what may be reached within the plume by gravity drainage. The centrifuge stage being executed with a single speed run, informed by the multi-speed test in module 2.

Module 3

This module is similar to modules 1 and 2, with the exception that the initial water saturation is achieved by desaturation in a flooding circuit against a porous plate, with gas being injected at the top of the vertically oriented core.

5.2.2. Reservoir condition tests

Module 4

This module addresses CO_2 injection at reservoir conditions in two stages:

- In the first stage of the test, an initial water saturation distribution that is representative of saturations within the CO_2 plume is established at ambient conditions using nitrogen. The N_2 is replaced with CO_2 and the rig was raised to temperature and pressure. The CO_2 relative permeability at the initial water saturation is measured. An imbibition water flood (with injection in the bottom of the vertically orientated core) then takes the core to the trapped CO_2 saturation to brine and the water endpoint relative permeability is measured.
- The core is taken to 100% brine to perform the brine calibration scan. This is achieved by flooding with dead brine until there is no further change in the gamma ray (GR) count rates and then displacing the dead brine with live brine. The core is then taken to 100% CO_2 saturation to allow a calibration scan to be performed for the GR saturation monitoring, using a flooding sequence of methanol, toluene pentane and finally CO_2. The permeability to CO_2 is measured. The next step in the flooding sequence is to return the core to 100% brine saturation.
- As an intermediate step between the 100% CO_2 saturated core and the brine saturated core required for the USS primary drainage flood, an imbibition waterflood is performed from 100% CO_2 saturation with live brine. This provides an additional set of data for trapped gas saturation. The core is then flooded with dead brine to remove the trapped CO_2 saturation before once again flooding with live brine.
- USS CO_2 injection is then performed at a series of increasing rates. CO_2 is injected at the top of the vertically mounted core, with an initial low rate of a nominal 4 cm^3/hour to maximise the benefit from gravity stabilising the displacement front. The saturation distribution at the different rates allows capillary pressure to be inferred using simulation over the range of pressure drops applied to the core. A subsequent imbibition water flood again brings the core to trapped gas saturation, with any variation in the initial CO_2 saturation giving a relationship between initial CO_2 saturation and trapped CO_2 saturation.

Module 5

To relate capillary pressures inferred from the reservoir condition tests to ambient condition data requires the CO_2 brine interfacial tension (IFT) to be known. This module uses the pendant drop method to measure IFT at reservoir temperature, across the range of reservoir pressures that will be encountered during operation of Goldeneye for CO_2 storage.

5.3. Programme overview

The remaining preserved core from the Captain D unit in well 14/29a-3 and 5 was computer tomography (CT) scanned to identify sections suitable for plugging for the new SCAL programme. In addition, Captain D plugs retained from the earlier study were also CT scanned, with the intent of performing part of the new programme of work on old plugs, to allow comparison with earlier results.

The reservoir condition module includes an USS primary drainage test. Simulations showed that using a single plug (even if this was maintained at the maximum possible length of around 8 cm) would likely mean that results were still influenced by capillary end effects. The Captain D sand is relatively homogeneous and has near unit k_v:k_h ratio, so to maximise the length of the cores used in the reservoir condition tests, axial plugs were cut from selected preserved sections. This avoids the need to build a composite core out of a number of shorter plugs, which for this very high permeability material would carry a greater risk of capillary discontinuities at the core butts. An

additional benefit of working with longer cores is that the accuracy of volumetric balance calculations is improved. Cores with usable lengths of around 20cm were successfully prepared.

Following plugging the individual plugs were also CT screened and characterised in terms of permeability and porosity (based on off cut plugs for the axial plugs, which were too long to fit in a conventional porosimetry rig). A final selection of conventional and axial plugs was then made for the SCAL programme as summarised in **Table 5.2**.

Table 5.2— Core plug selection and module assignment for CO_2 SCAL programme

						Module			
Plug	Well	Length (cm)	Diameter (cm)	Original brine permeability (md)	Porosity	1	2	3	4
S5A	14/29a-5	4.9	3.56	1148	0.271	✓			
38A	20/4b-6	4.9	3.70	1101	0.265	✓			
50A	20/4b-6	4.8	3.72	1438	0.261	✓			
PS6-1a	14/29a-3	4.7	3.64	2354	0.259	✓	✓		
PS9-1b	14/29a-3	4.8	3.70	1569	0.263	✓	✓		
PS17-1d	14/29a-3	4.9	3.69	896	0.238	✓	✓		
PS6-1B	14/29a-3	8.4	3.75	2257	0.264			✓	
PS9-1A	14/29a-3	8.8	3.76	1484	0.263			✓	
PS17-1B	14/29a-3	9.0	3.74	982	0.241			✓	
PS15-1A	14/29a-3	20.5	3.76	1350	0.269*				✓
PS1	14/29a-3	19.8	3.76	2048	0.263*				✓
PS10-1A	14/29a-5	21.4	3.68	1025	0.269*				✓

*Porosity based on trims from axial plugs

For the ambient condition Modules, plugs from three different permeability ranges were selected for Modules 1 to 3, around 900 mD, 1500 mD and 2300 mD. These were augmented by three plugs from the earlier studies (one from the gas-water tests and two from the gas-oil tests).

Plugs for modules 1 and 2, which used the centrifuge method to establish S_{wi}, were trimmed to 5cm length. However, the plugs for Module 3 were retained at their original length of 8 to 9 cm to maximise the pore volume.

6. CO_2 SCAL programme results

This section describes an initial analysis of the results of the SCAL programme. Significant amounts of data were generated and there is further detailed analysis recommended.

6.1. Ambient condition tests

This section discusses the results of the ambient condition tests. An initial water saturation on the primary drainage cycle was established using either the centrifuge or porous plate methods. Gas relative permeability at S_{wi} was measured. The plugs were then water flooded and the trapped gas saturation and the water relative permeability determined.

The initial brine permeability is compared with the brine and air permeability measured after the test sequence for each plug, **Fig. 6.1**. This shows a good consistency between the initial and final brine permeability, with air permeability in the dried plugs also similar to the reference initial brine permeability.

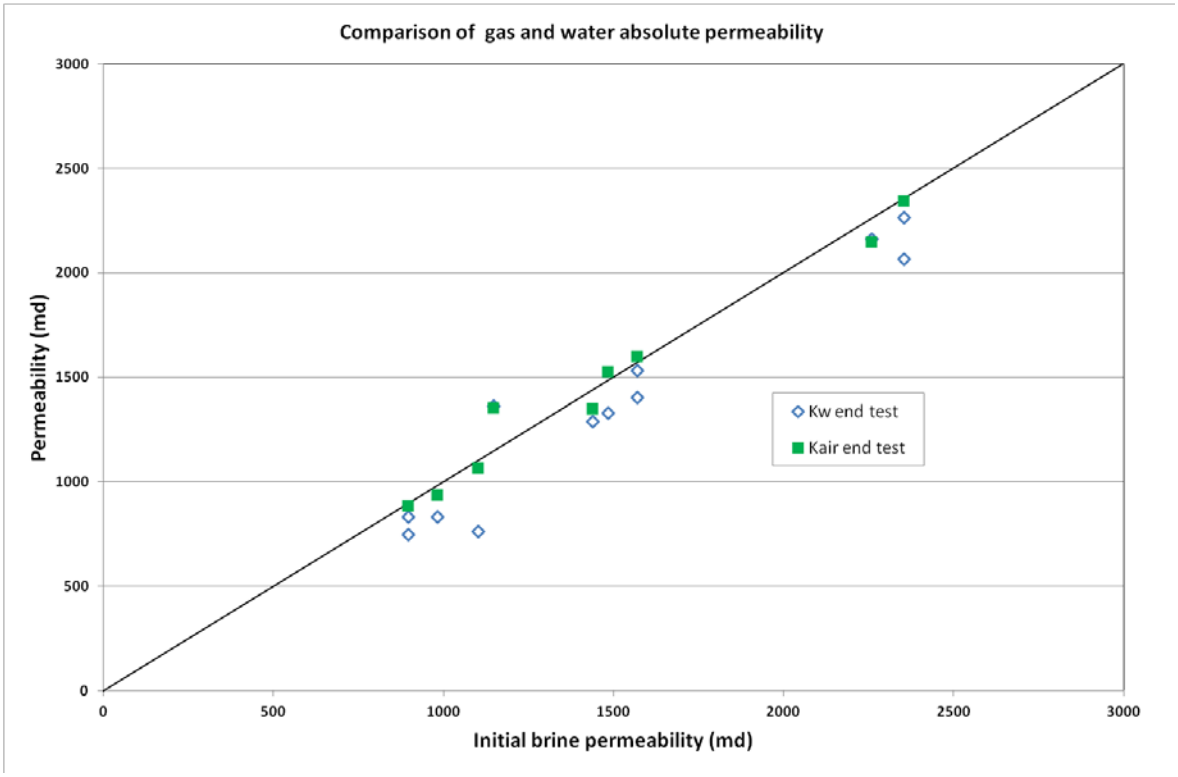

Fig. 6.1—Comparison of initial and final plug permeabilities in ambient condition tests

The gas permeability at initial water saturation was also compared to the initial brine permeability, **Fig. 6.2.** Within the range of initial water saturations established the gas relative permeability does not show any reduction. In the module 2 tests significantly higher gas permeabilities at S_{wi} were measured. This is despite subsequent 100% brine permeability showing values in line with the original permeability. The only difference in these plugs is that the conventional core analysis was carried out between the Module 1 and Module 2 tests, so that the cores were dried to determine porosity.

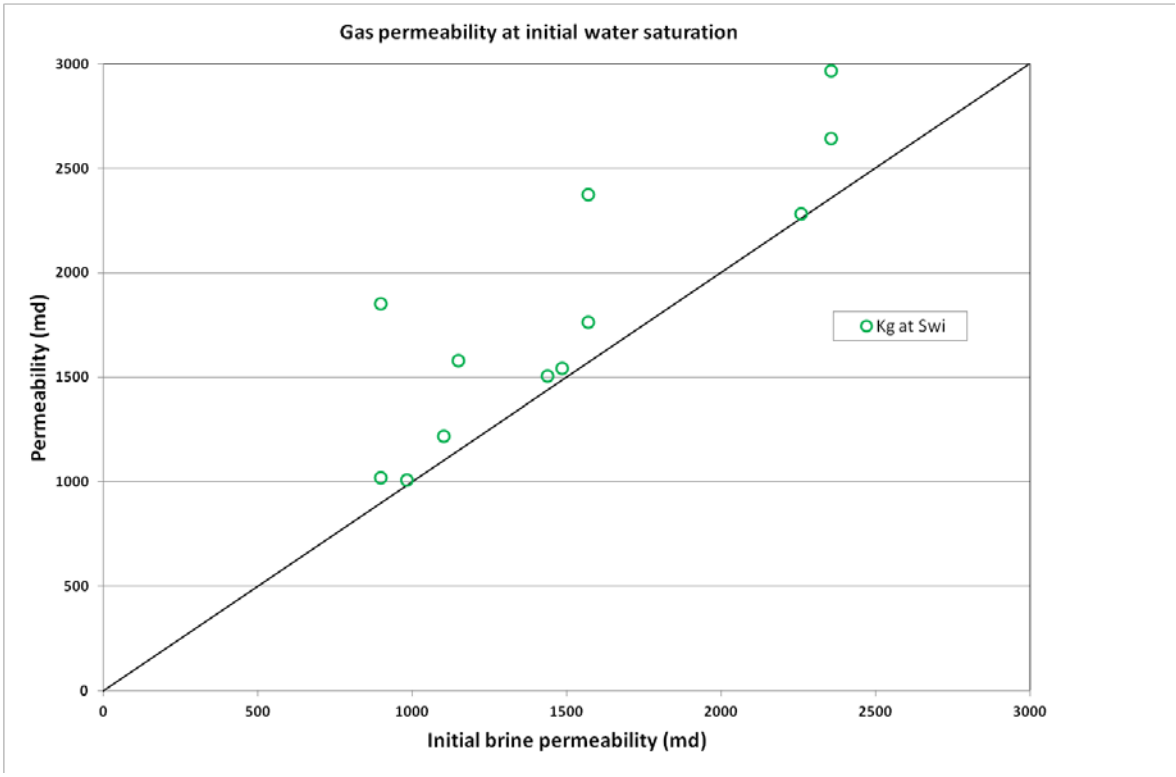

Fig. 6.2—Gas permeability at S_{wi} compared to initial brine permeability

Fig. 6.3 shows the relationship between the initial gas saturation and the subsequent trapped saturation (based on the best estimate procedure discussed in Section 8.2). For the range of initial water saturations explored (corresponding to initial conditions prior to Goldeneye development and those expected to be present in the CO_2 plume) there is no significant correlation between trapped gas saturation and the initial gas saturation. A potentially anomalous point is shown by the open symbol (see Section 8.2).

The data was also analysed to assess any permeability dependence in the relationship between trapped gas and initial gas saturation, over the three categories described in Section 5.3. These are highlighted in **Fig. 6.4,** where the points are coded red (<1200 mD), orange between 1200 mD and 2000 mD) and green (>2000 mD). No significant dependence on permeability is observed.

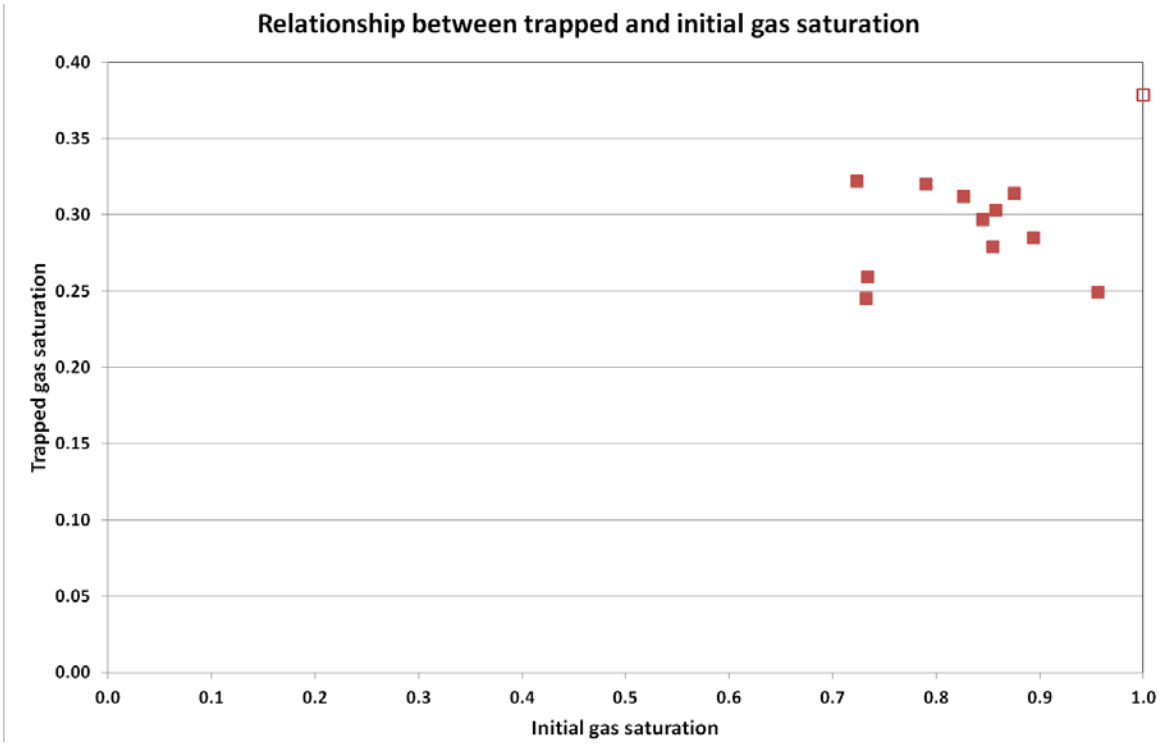

Fig. 6.3—Relationship between trapped gas saturation and initial gas saturation for ambient condition tests in new SCAL programme

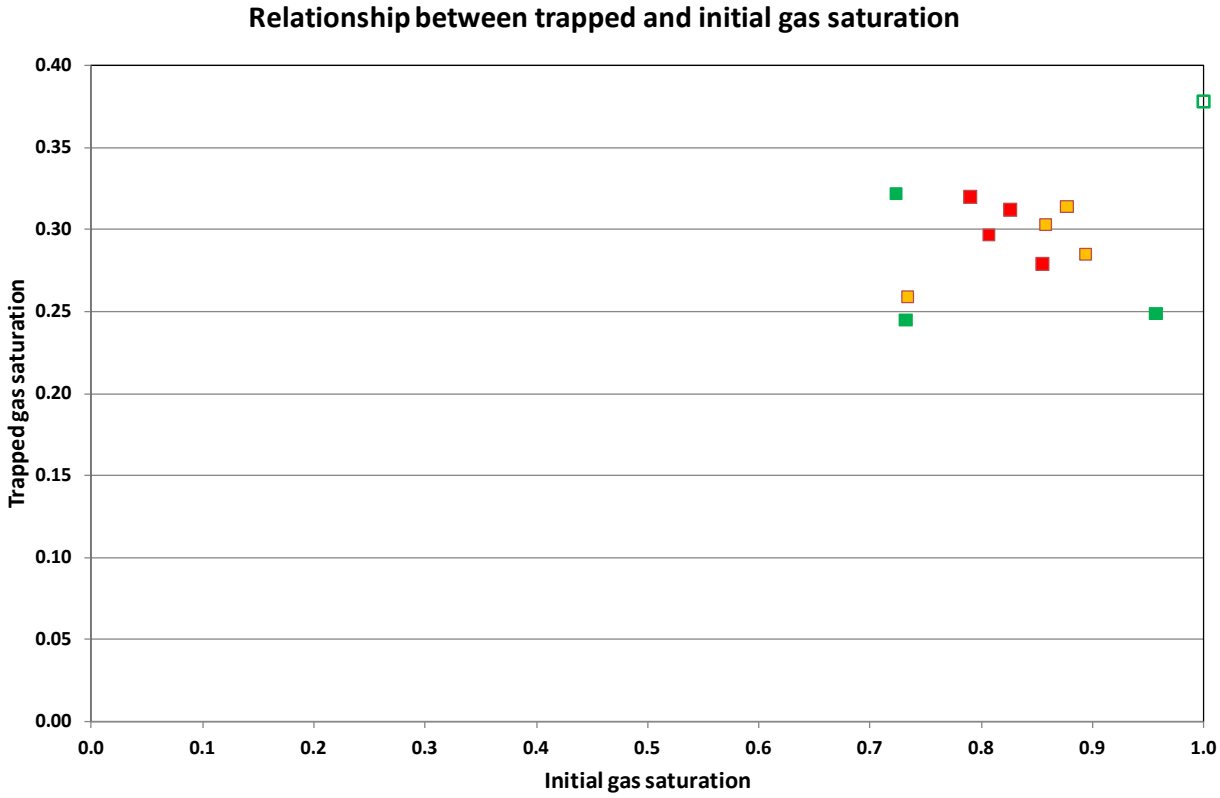

Fig. 6.4—Assessment of dependence of trapped gas saturation on permeability

Fig. 6.5 compares the new data with the legacy Captain D data (legacy saturations corrected where necessary based on the analysis described in Sections 3.1 and 3.2). The new data and old data sets are consistent, and fully support the uncertainty bands derived for input to history matching of Goldeneye production performance.

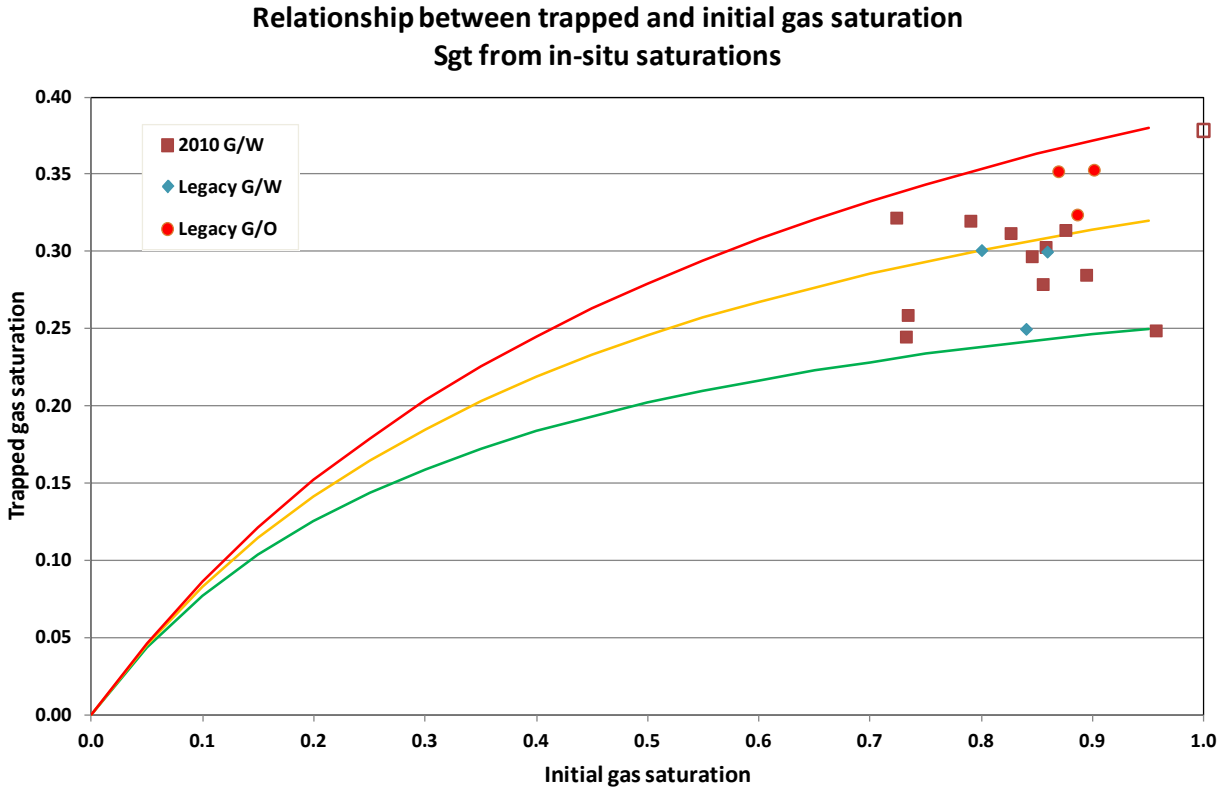

Fig. 6.5—Trapped gas saturation vs. initial gas saturation for new data and legacy data

Water relative permeability data at trapped gas saturation is plotted as a function of trapped gas saturation in **Fig. 6.6**. Data is not included for the legacy Captain D plugs which had required correction of saturations, since the relative permeability cannot be corrected to allow for this. Two data points from the new data set, PS9-1b (Module 1) and S5A, with demonstrated laboratory artefacts (see Section 8.3) are also omitted. The remaining data shows a clear correlation between the water relative permeability at trapped gas saturation and the trapped gas saturation. There is consistency between the reinterpreted legacy data and the new data and this supports the range of endpoint relative permeability of 0.05 to 0.25. Representing this in terms of a Corey relationship (tied to S_{wi} of 10%) gives a base case Corey coefficient of 4.7, with an uncertainty band of 6.3 to 3.6.

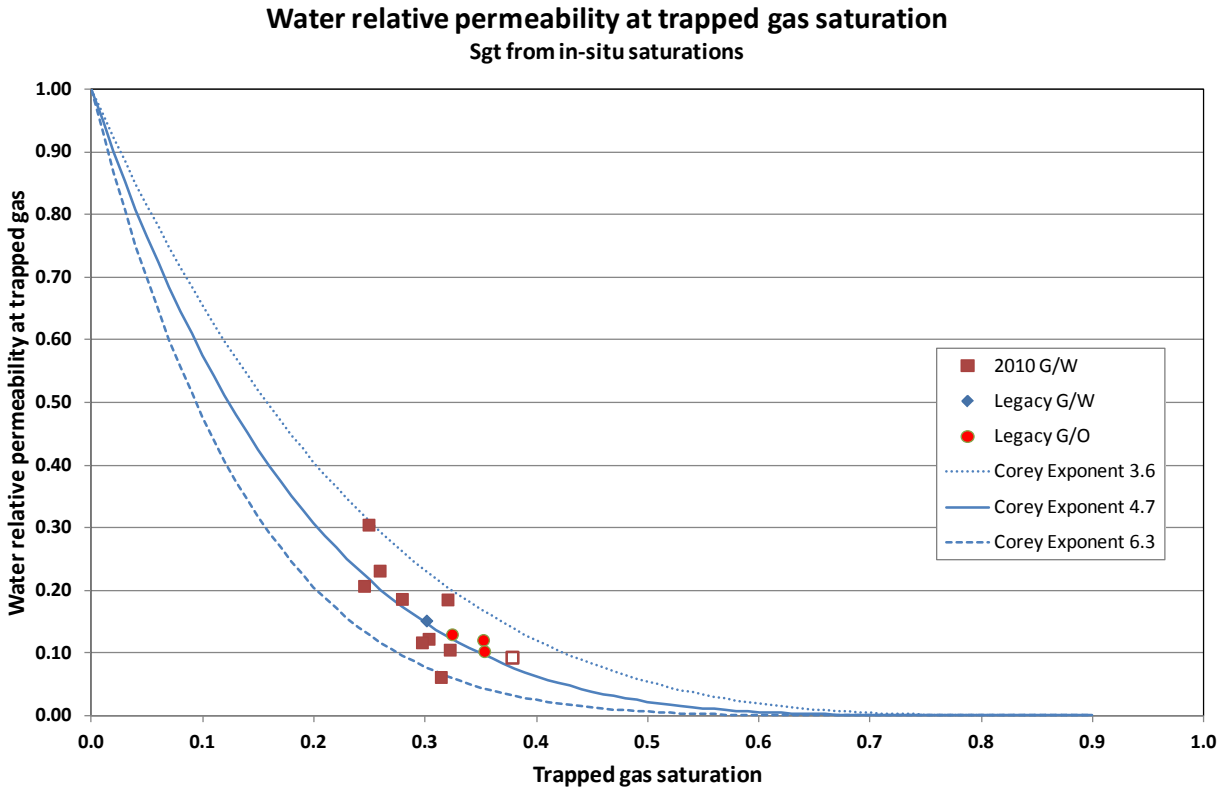

Fig. 6.6—Water relative permeability at trapped gas saturation for Captain D

6.1.1. Transient saturation profiles

Examination of the transient saturation profiles for all the USS brine imbibition floods to trapped gas saturation showed an unexpected range in behaviour.

- At one extreme, illustrated by **Fig. 6.7**, injected water appears to be drawn along the length of the core to give a relatively uniform water distribution, which just increases with time. Note that here each profile represents a transient state in the USS displacement. These should not be confused with the saturation profiles in Section 3 which are SS profiles corresponding to different fixed fractional flows of injected gas/water or gas/oil. In contrast, the production data shows 100% gas production until water breakthrough, after which there is essentially no further gas production. This behaviour is believed to be the result of the high permeability core material, in which capillary pressure can dominate over the viscous pressure drop at this short length scale, with water being imbibed through the core in the water-wet system. However, because of the water-wet nature of the core and the unfavourable mobility ratio, mobile gas is produced from the outlet of the plug to the exclusion of brine, until there is no more mobile gas in the plug when the trapped gas saturation is attained.
- **Fig. 6.8** shows a different type of behaviour, with a clear front moving through the plug, although again the theoretical shock front for the favourable mobility ratio displacement is still partly smeared by capillary pressure. Once more mobile gas is produced from the outlet of the plug to the exclusion of brine, until there is no more mobile gas in the plug.

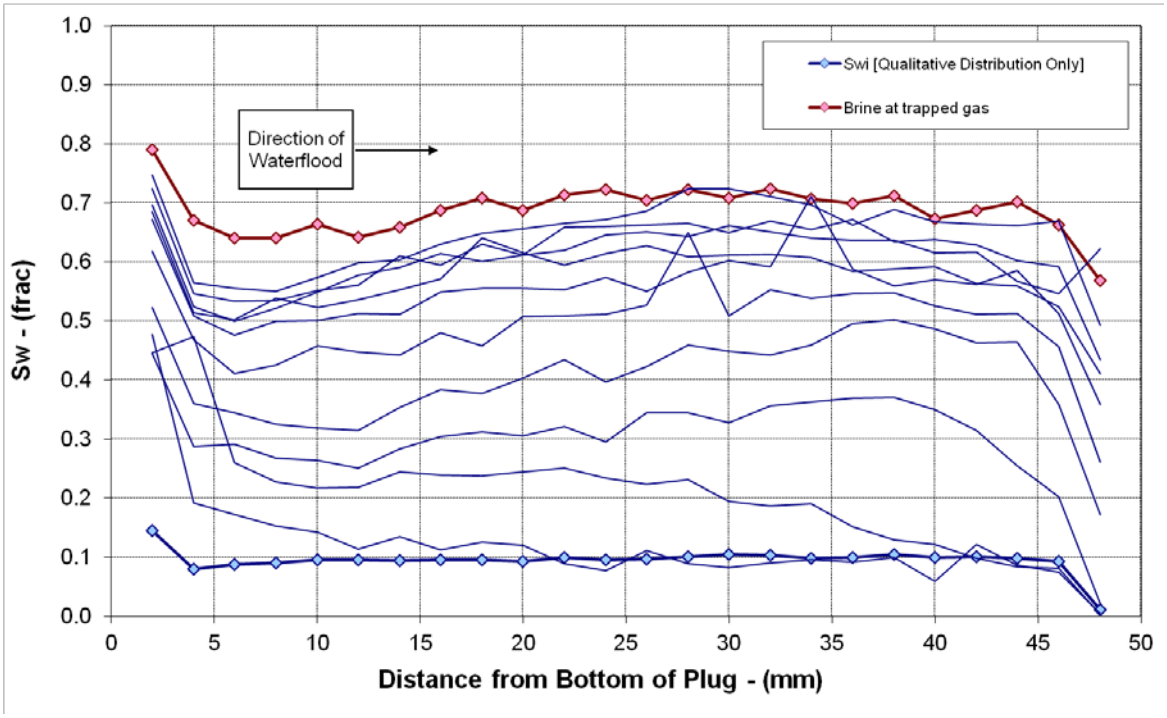

Fig. 6.7—Profiles for water imbibition flood in plug S5A showing transient data

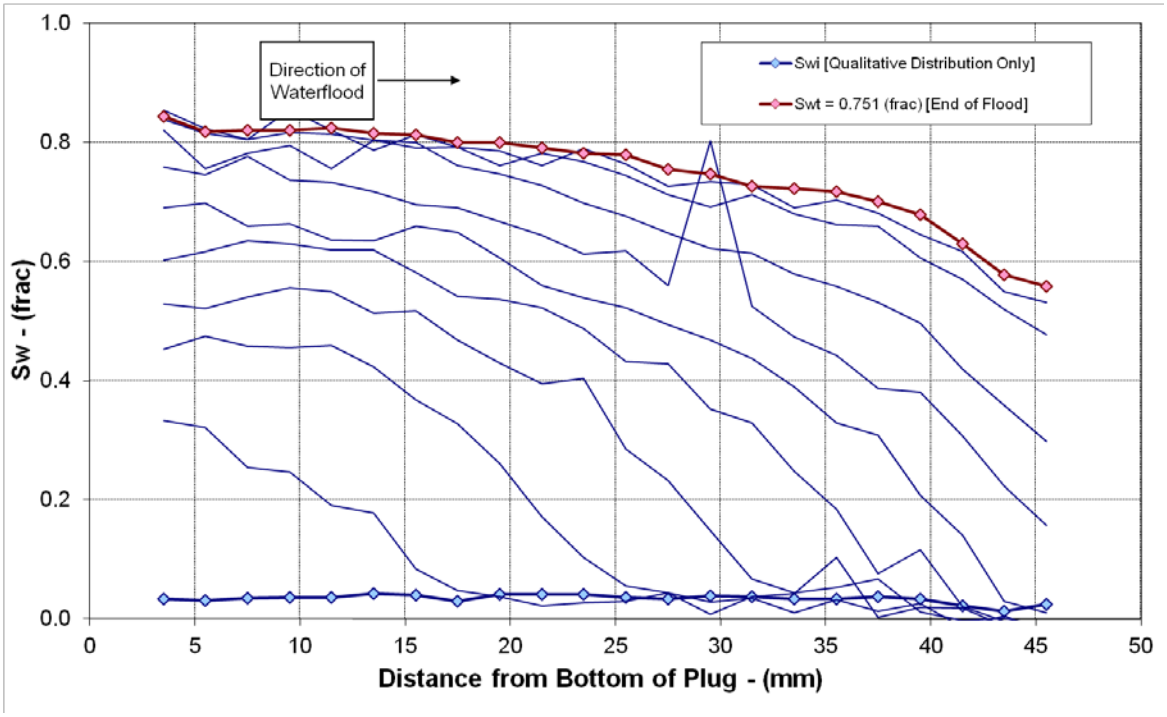

Fig. 6.8—Saturation profiles for water imbibition flood in plug PS6-1a (1) showing transient data

6.2. Reservoir condition flooding tests

Three reservoir condition flooding sequences were undertaken. In the first test (Axial Plug PS15-1A) the brine was doped with sodium iodide, a conventional dopant used to increase the GR attenuation

between the brine and gas phase and improve the accuracy and acquisition time for saturation data. Sodium iodide has been used in previously reported reservoir condition CO_2/brine displacements. As the first test progressed it was observed that the brine phase was becoming discoloured and that the CO_2 had acquired a pinkish hue. In the subsequent two reservoir condition tests, (Axial Plug PS1-1A and PS10-1A) the brine was changed out, from sodium iodide doped synthetic formation brine, to a brine doped with caesium chloride.

Plug PS15-1A suffered a structural failure of the sample leading to the release of fines, which blocked the flow lines and led to the sequence of tests being terminated.

Results from the two successful CO_2 floods each generate three sets of gas relative permeability data, trapped gas saturation data and water endpoint relative permeability at trapped gas:

- CO_2 relative permeability at pre-conditioned initial water saturation, followed by primary imbibition with water to trapped gas saturation
- CO_2 permeability at 100% CO_2 saturation, followed by primary imbibition with water to trapped gas saturation
- Primary drainage of water with CO_2, followed by primary imbibition with water to trapped gas saturation
-

Saturations have been plotted as the average of the (core average) in-situ data and the volume balance data, with error bars plotted on the points to show the spread between the in-situ and volumetric data.

Fig. 6.9 shows the CO_2 relative permeability at each of the three stages for the two plugs. In all cases the CO_2 relative permeability is between 0.75 and 1.0, showing that the influence of the initial water saturation is small. This range is well within the range of 0.5 to 1.0 used in sensitivity studies of CO_2 injection. Before the failure of Plug PS-15-1A a CO_2 relative permeability of 0.97 was measured, although the initial water saturation is uncertain (22% based on volumetric data). This is in line with the results from Plugs PS1-1A and PS10-1A.

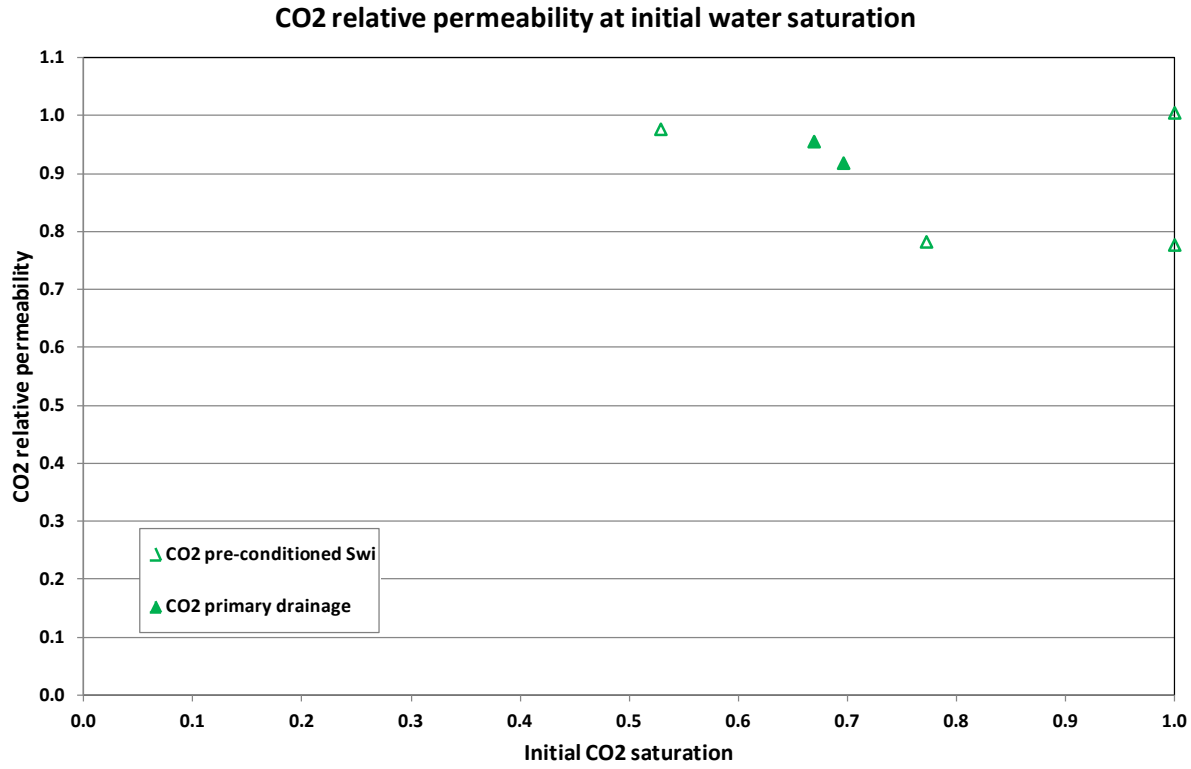

Fig. 6.9—CO_2 relative permeability as function of gas saturation

The results for the water imbibition floods are shown in **Fig. 6.10.** There is a striking difference between the tests with the initial water saturation established by primary drainage with CO_2 and the case of a pre-established S_{wi} or zero initial water saturation. The trapped saturation after primary drainage (solid green triangles) lies within or above the uncertainty band established by the ambient condition tests. In contrast, significantly lower, but still non-zero trapped CO_2 saturations are found for the pre-established initial water saturation or the case of zero initial water (open green triangles). The significance of this result for the Peterhead CCS project is discussed in Section 7.

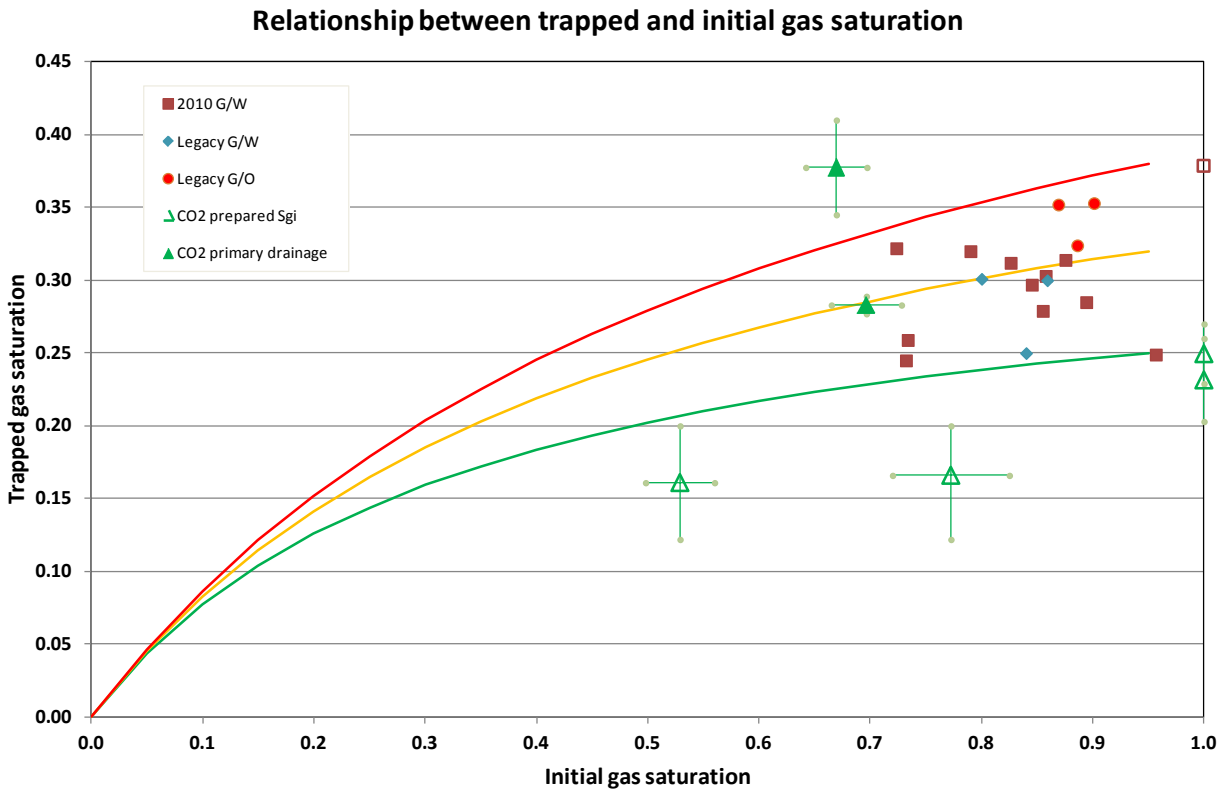

Fig. 6.10—Trapped gas saturation for ambient condition and reservoir condition CO_2 displacements

The corresponding water endpoint relative permeabilities are shown in **Fig. 6.11.** Water endpoint relative permeability at trapped gas saturation for ambient condition and reservoir condition CO_2 displacements lie on the same general trend.

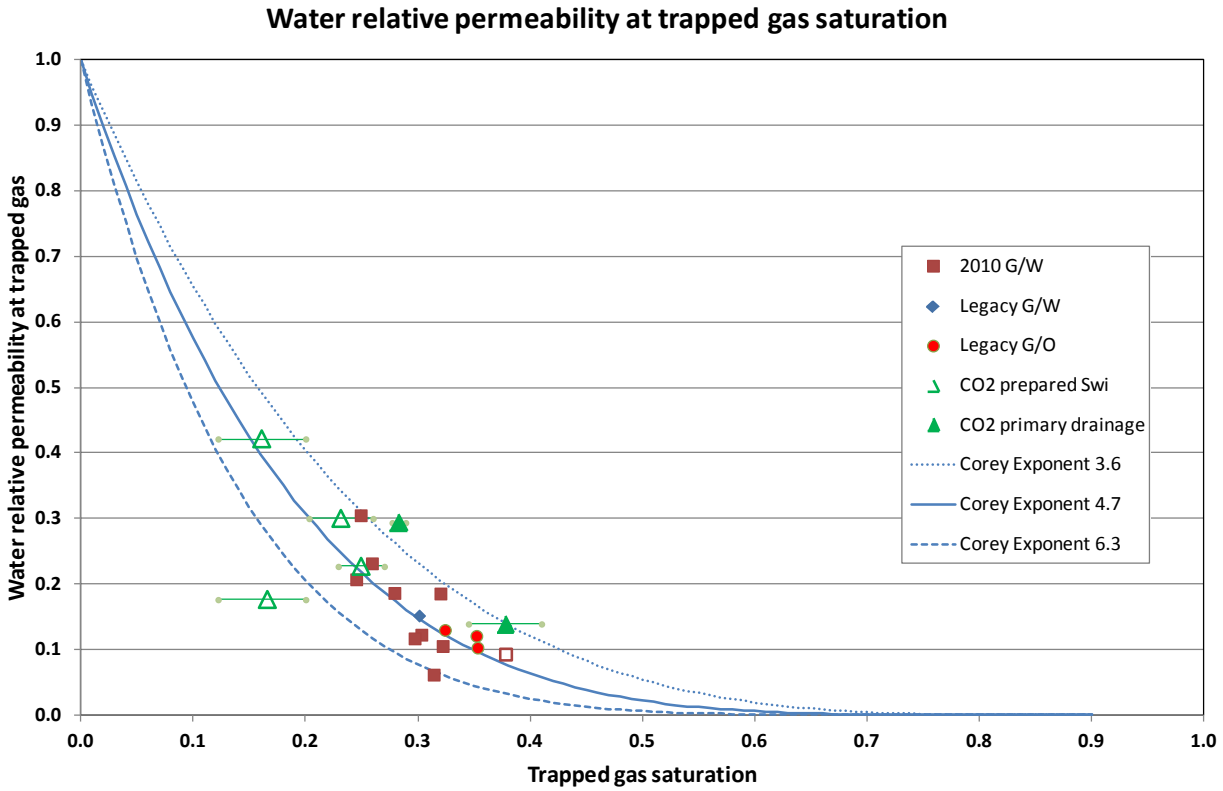

Fig. 6.11—Water endpoint relative permeability at trapped gas saturation for ambient condition and reservoir condition CO_2 displacements

6.2.1. Transient saturation profiles

This section discusses the transient saturation profiles, looking at whether these shed any light on the different levels of gas trapping found after primary drainage with CO_2 compared to starting at 100% CO_2 saturation or at a pre-conditioned initial water saturation.

In-situ saturation profiles for primary drainage of water by CO_2 and subsequent water imbibition in PS1-1A are shown in **Fig. 7.12** and **Fig. 6.13,** respectively. The primary drainage flood with CO_2 comprised three rate steps (nominal rates of 4, 40 and 400 ml/h), as the flow rate was increased the capillary pressure end-effect resulting in brine hold-up at the base of the core was progressively reduced. The CO_2 injection produces a relatively uniform water saturation with an average of 27%, for 50PV injection, and was as successful as the dedicated ambient condition flooding used to establish S_{wi} for the pre-conditioned S_{wi} scenario. The following brine imbibition flood produces a uniform trapped gas saturation profile in the core. The transient saturation profiles show the water shock front being smeared out, giving similar behaviour to the ambient condition tests. The presence of anomalously high saturations at the top of the core towards the end of the water imbibition flood is noted.

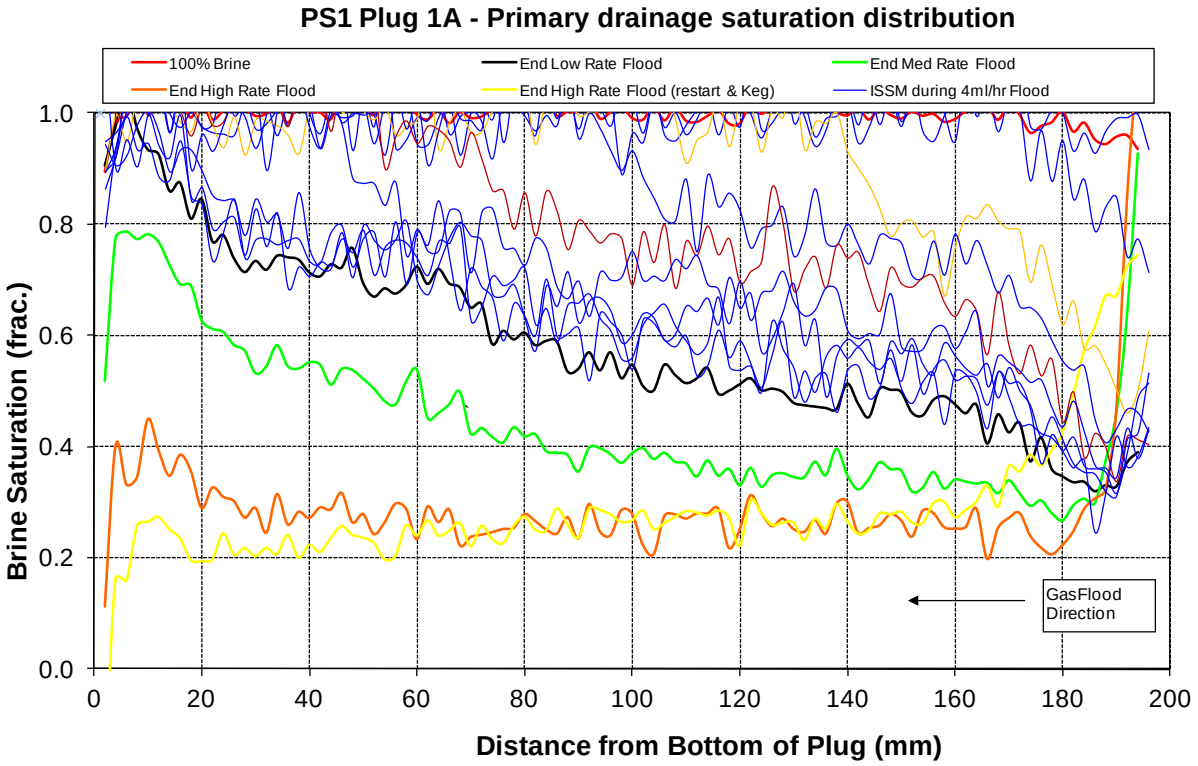

Fig. 6.12—Primary drainage with CO_2 in Plug PS1-1A

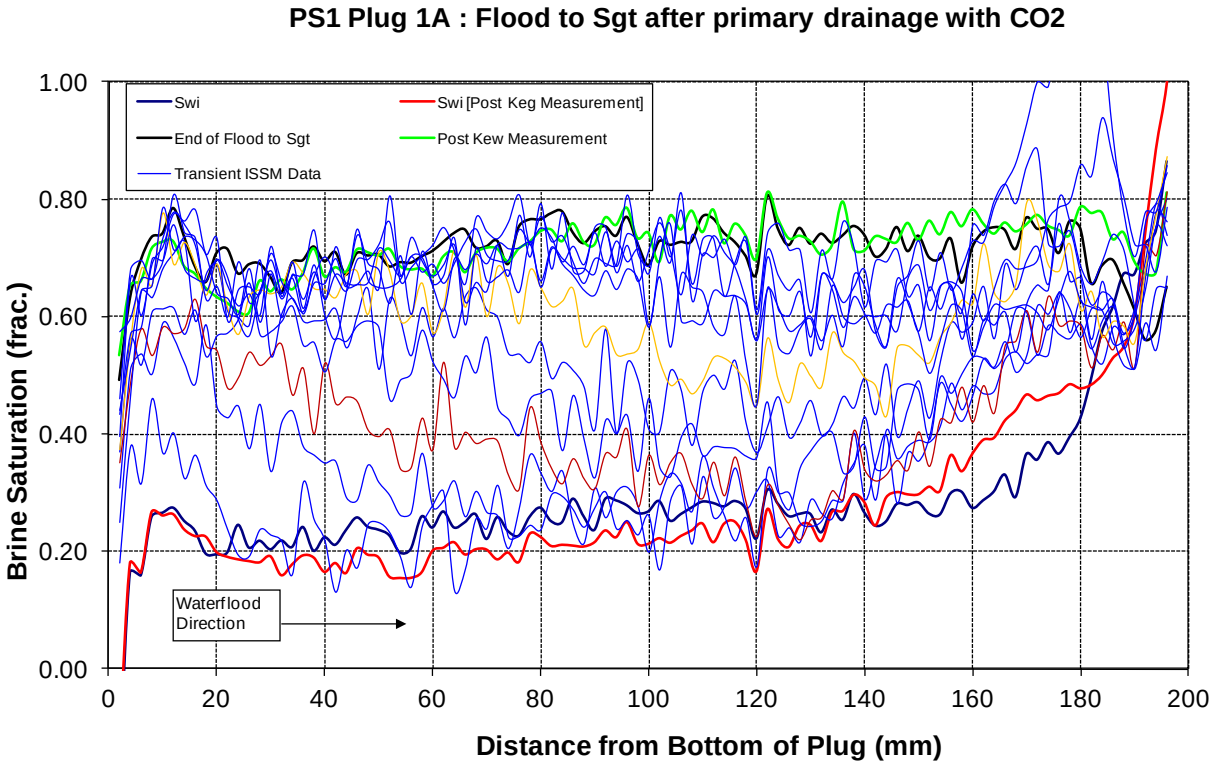

Fig. 6.13—Flood to trapped gas saturation after primary drainage with CO_2 in Plug PS1-1A

The equivalent set of plots for PS10-1A is shown in **Fig. 7.14** and **Fig. 7.15** respectively. The primary drainage flood with CO_2 comprised two rate steps (nominal rates of 4 and 400 ml/h), as the flow rate

is increased the capillary pressure end-effect resulting in brine hold-up at the base of the core is reduced. Again the CO_2 injection proves to be quite effective at lowering the water saturation. The transient saturation profiles for the water imbibition show the water shock front being smeared out, as in Plug PS1-1A. Most of the plug (bottom 140 mm) shows a uniform trapped gas saturation.

In a small section at the top of the plug (40 mm) the high rate drainage flood establishes an interval of reduced initial water saturation and then reduced trapped CO_2 saturations after imbibition.

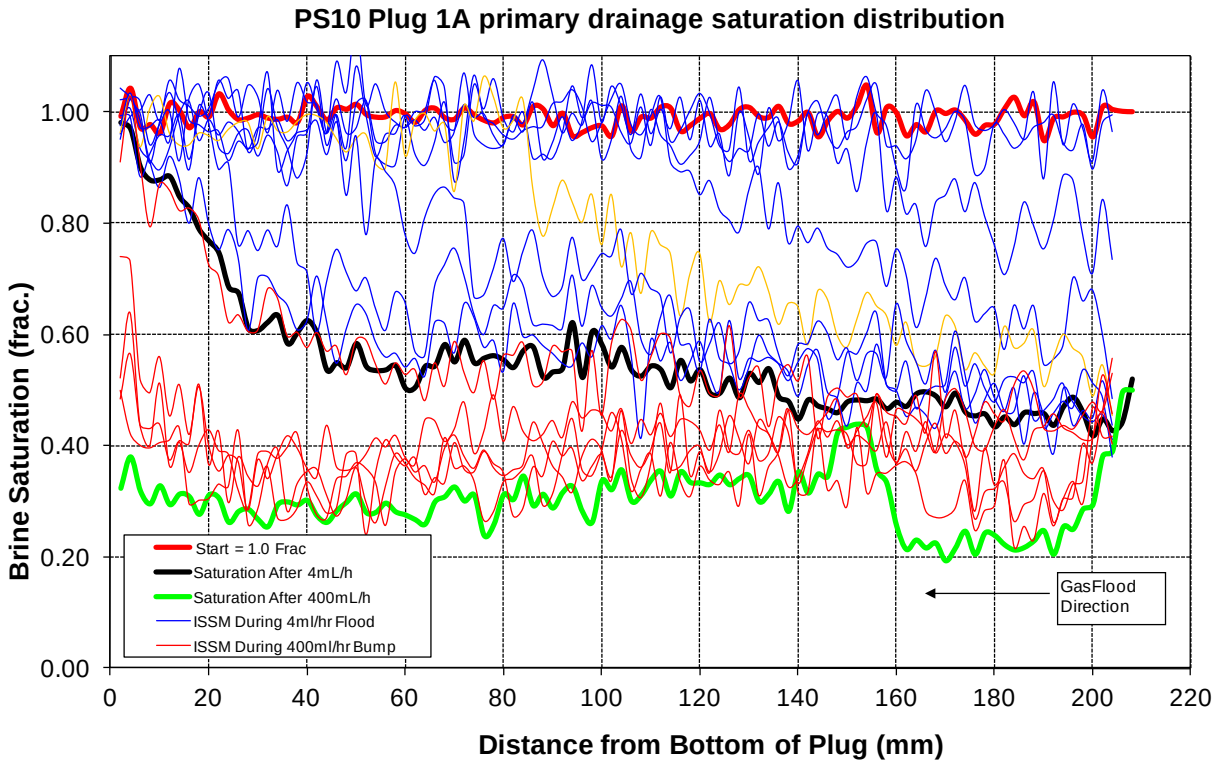

Fig. 6.14—Primary drainage with CO_2 in Plug PS10-1A

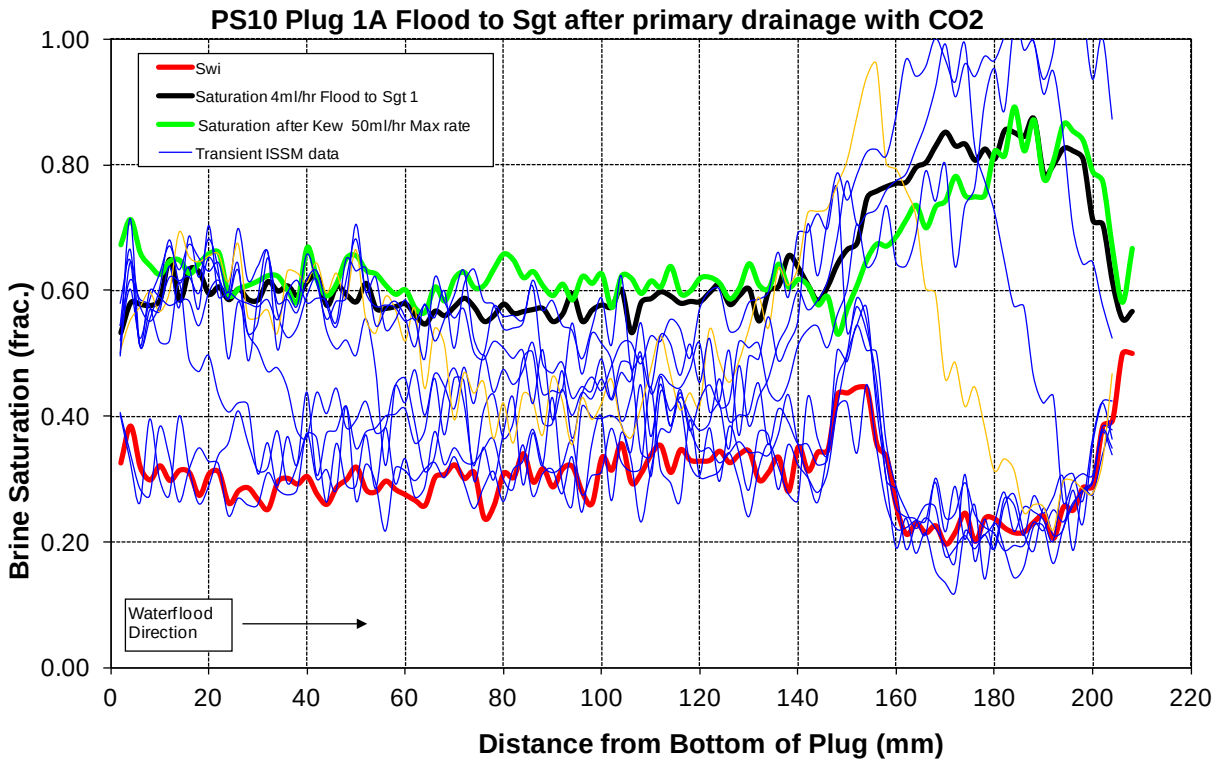

Fig. 6.15— Flood to trapped gas saturation after primary drainage with CO_2 in Plug PS10-1A

Saturation profiles for the imbibition water flood from the pre-conditioned initial water saturation are shown in **Fig. 6.16** and **Fig. 6.17.** These show a significantly different character, with a much sharper shock front. PS1-1A shows some temporary anomalous in-situ saturation behaviour just behind the front.

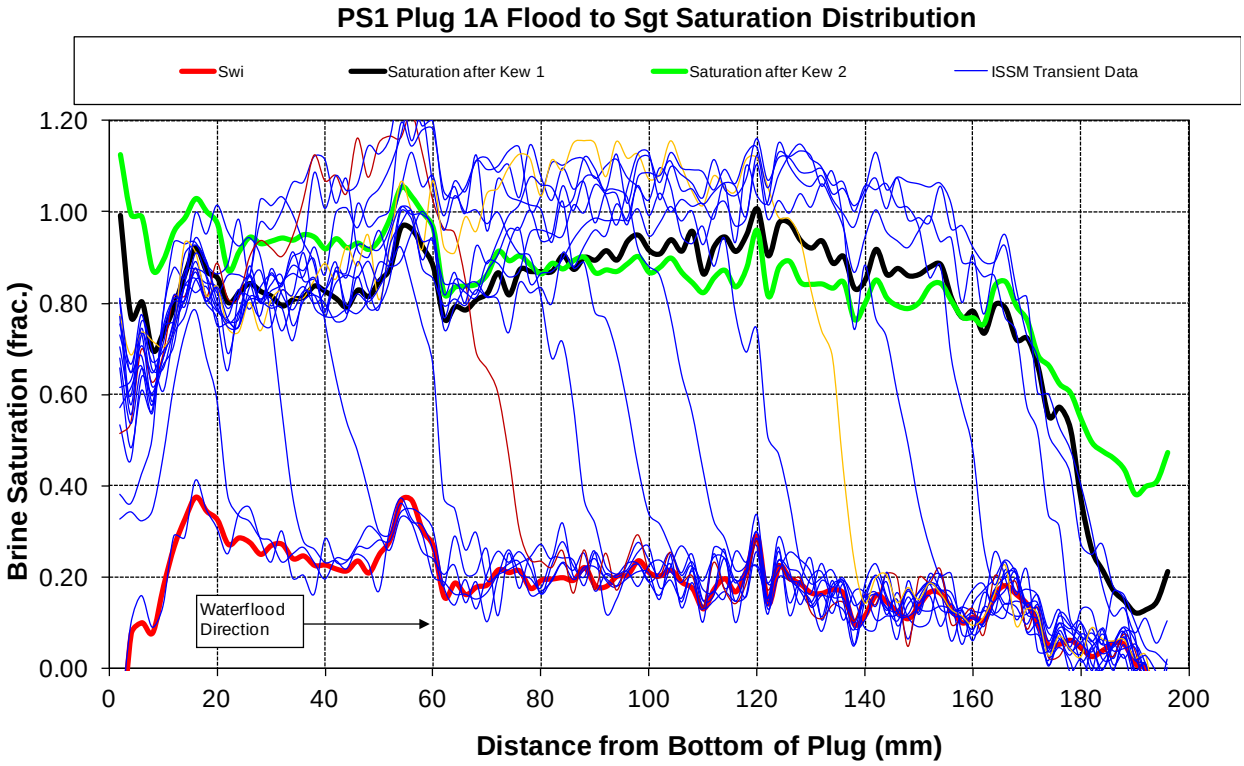

Fig. 6.16—Flood to trapped gas saturation for PS1-1A following S_{wi} being established at ambient conditions

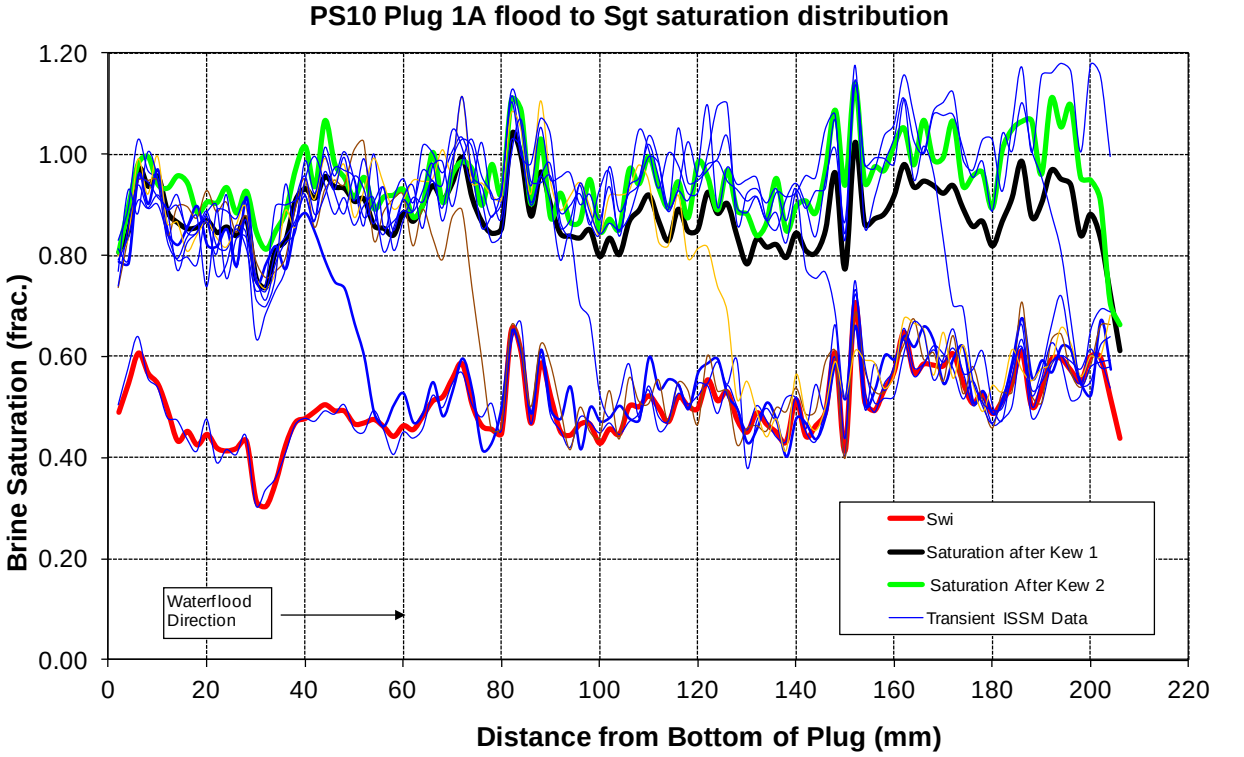

Fig. 6.17—Flood to trapped gas saturation for PS10-1A following S_{wi} being established at ambient conditions

A similar flooding character is also seen in the imbibition floods from 100% CO_2 saturation, **Fig.** 6.18 and **Fig. 6.19.** PS1-1A is slightly more complicated with the central region of the core temporarily suppressing the shock front as it passes through.

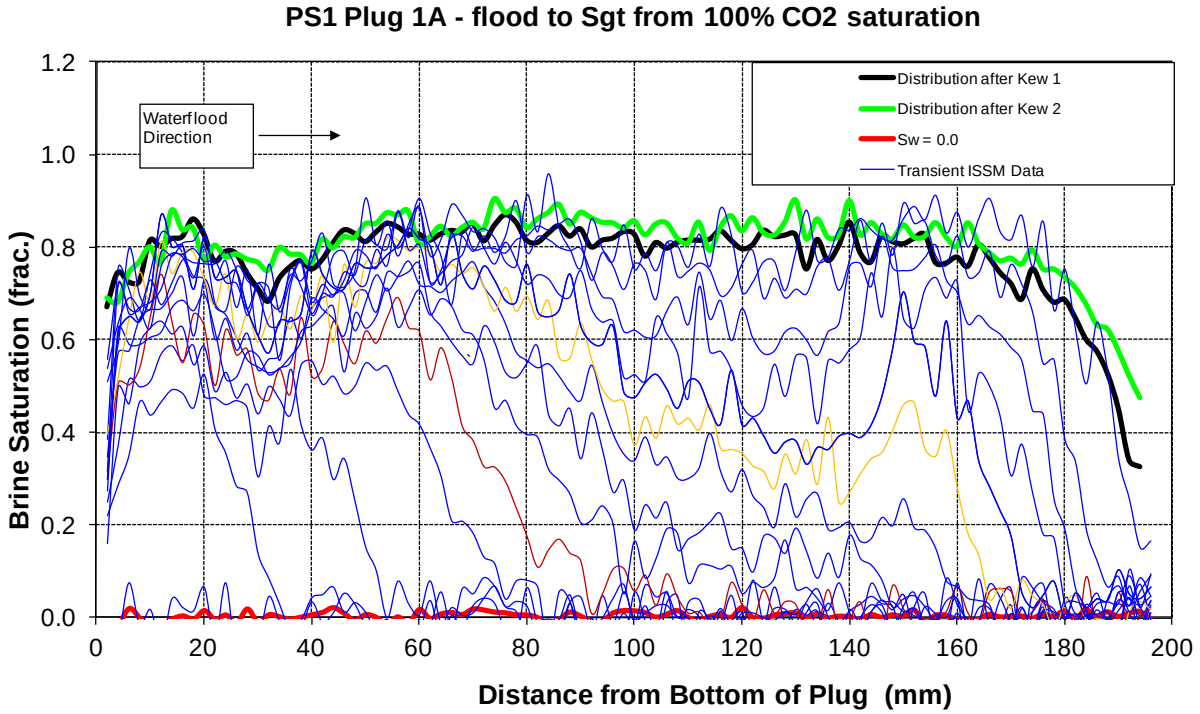

Fig. 6.18—Flood to trapped gas saturation for PS1-1A from 100% CO_2 saturation

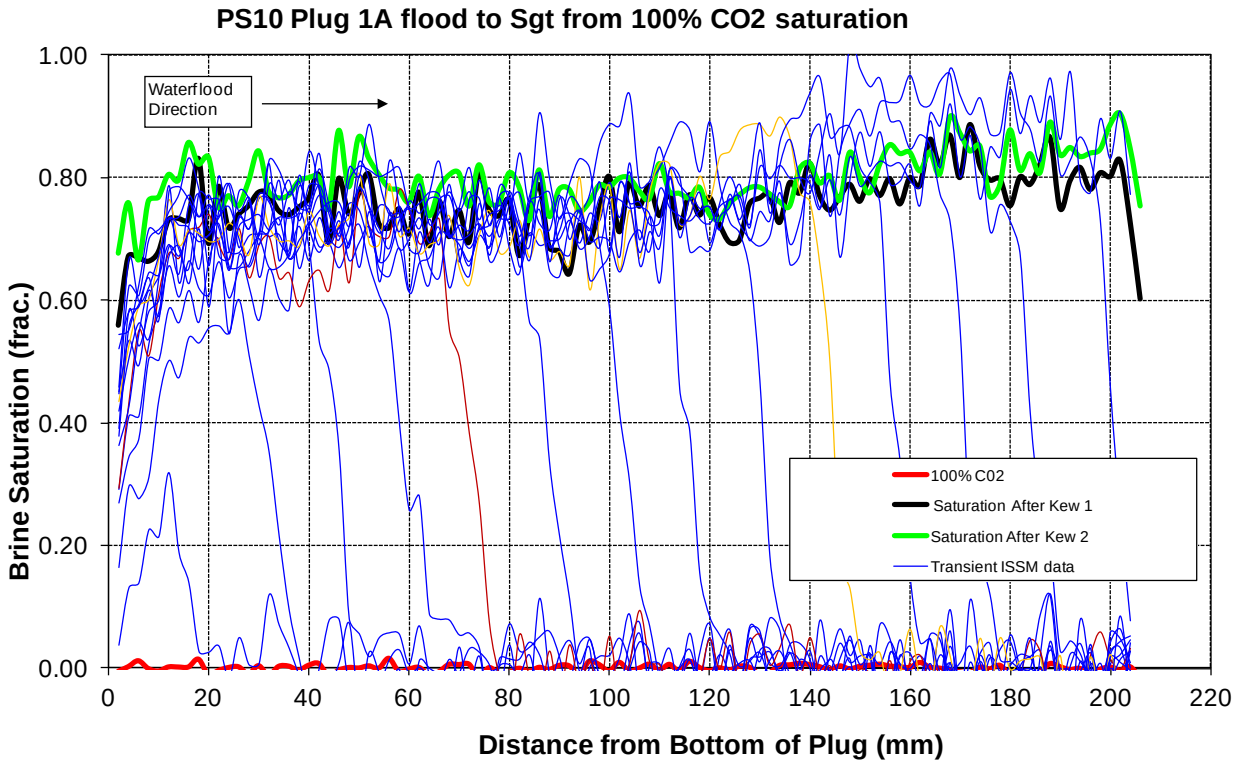

Fig. 6.19—Flood to trapped gas saturation for PS10-1A from 100% CO_2 saturation

The clear qualitative conclusion from this analysis is that the saturation profiles indicate a different character to the displacement depending on whether the imbibition flood starts from a water saturation established by primary drainage to CO_2 or not. This appears to correlate with the differences observed in average trapped gas saturations as a function of initial water saturation depending on the preparation method.

6.3. Brine/CO_2 interfacial tension

Interfacial tension has been measured using the pendant drop method at a range of pressure between 2000 psia [13789.51 KPa] and 4000 psia [27579.03 KPa] at 80°C.

The pendant drop method calculates IFT based on fitting the shape of the drop with solutions of the Young-Laplace equation. IFT can then be calculated provided the density difference between the phases is known, **Fig. 6.20.** The brine density and CO_2 density were measured as supporting data to the pendant drop experiment.

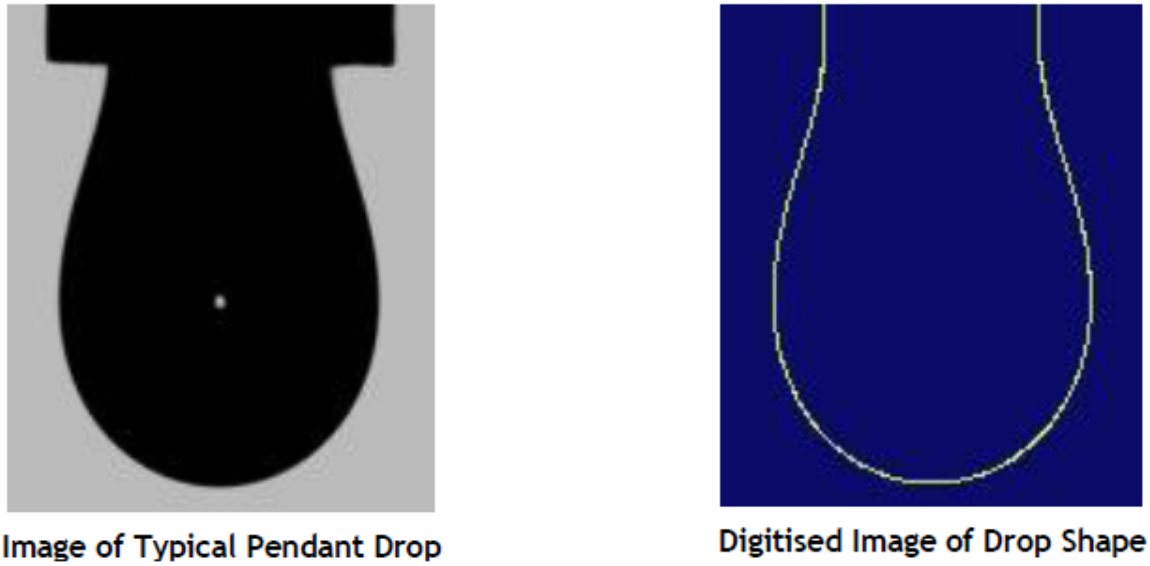

Fig. 6.20—Typical pendant drop shape and digitised image

The measured data is shown in **Fig. 6.21**. The reported IFTs are plotted, together with an adjusted set in which the density difference was based on the density of pure CO_2.

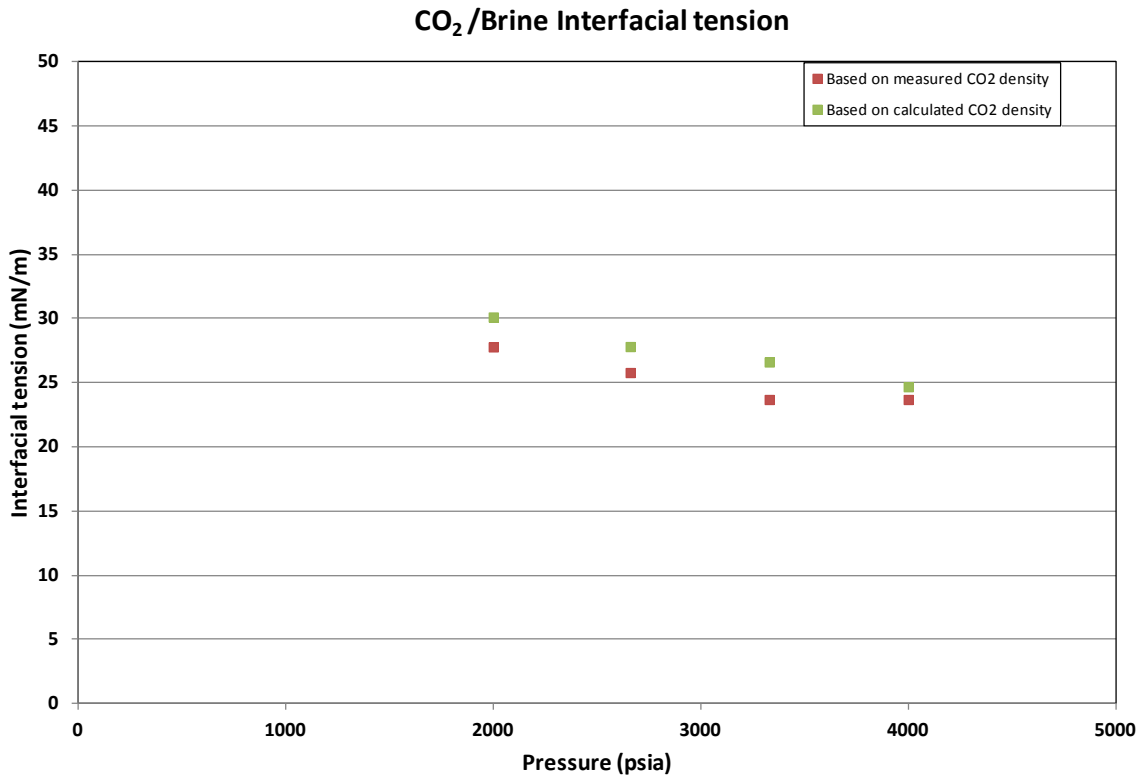

Fig. 6.21—Measured CO_2/Brine interfacial tension as function of reservoir pressure

The measured data is plotted as a function of the CO_2/brine density difference in **Fig. 6.22** and also shows a correlation which represents literature data. Goldeneye data is seen to be consistent with other reported data.

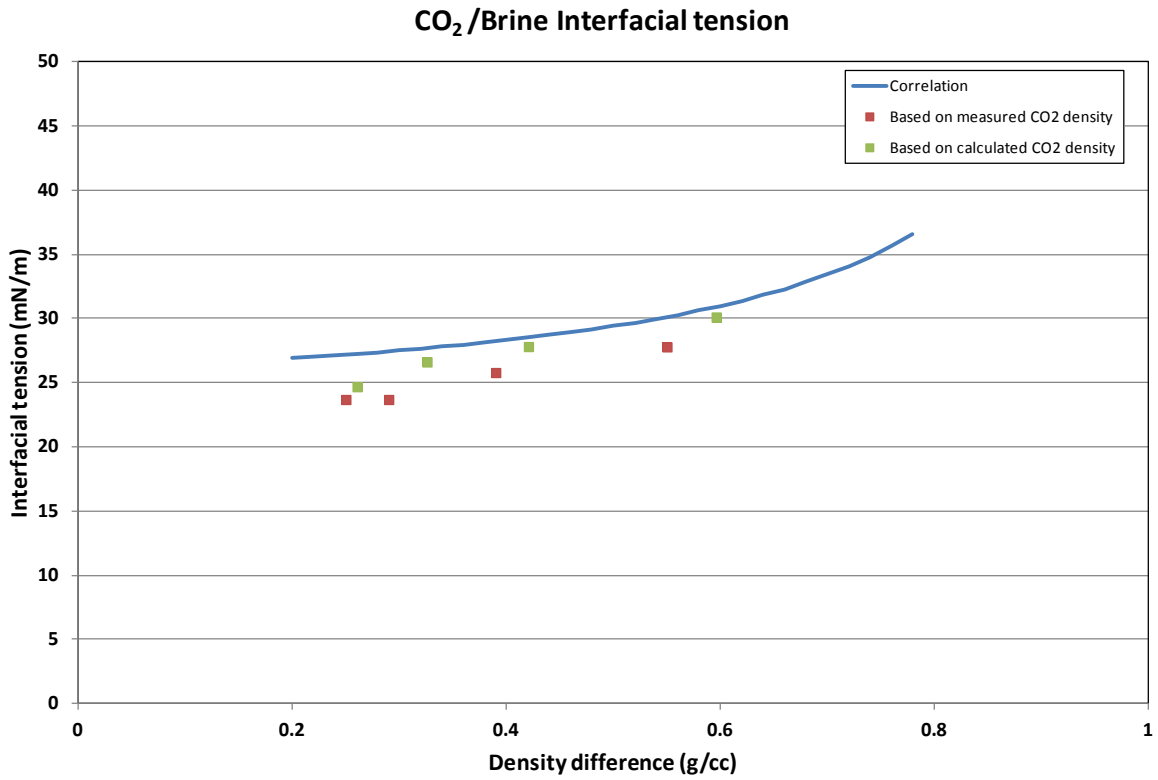

Fig. 6.22—CO_2/brine interfacial tension as a function of CO_2/brine density difference

7. Implications of SCAL results for modelling of CO_2 storage

In this section the results presented in Section 6 are discussed with particular reference to the wider technical assessment of the suitability of Goldeneye for Carbon Dioxide Storage.

The following general conclusions have been reached:

1) Based on ambient condition measurements an uncertainty range on trapped gas saturation has been established.
2) A clear relationship (with uncertainty bands) between trapped gas saturation and the water relative permeability at trapped gas has been established.
3) The current history matches uses relative permeability parameters that are within the uncertainty range developed, with a consistent combination of trapped gas saturation and water relative permeability.
4) Reservoir condition tests have shown that the relative permeability of CO_2, at a range of water saturations that cover the expected water distribution in the plume, is between 75% and 100% of the absolute water permeability. Sensitivity studies of CO_2 storage examining the Dietz stability of the CO_2 plume and injectivity used a range of 50% to 100% encompassing the SCAL results.
5) Trapped CO_2 saturations are in line with or higher than those predicted from ambient tests if the initial CO_2 saturation was established through primary drainage with CO_2. Unexpectedly low trapped saturations (12 to 25%) were measured if the water imbibition started from a pre-conditioned S_{wi} or at zero water saturation.

At the time of defining the SCAL programme it was not confirmed whether CO_2 could escape from the structure via a local spill point and then migrate updip in the Captain aquifer to the west. Subsequent simulation studies did not find a scenario where this occurs for injection volumes less than or equal to 10 or 20 mln tonnes of injection over 10 years; so the level of CO_2 capillary trapping has turned out to be much less critical in establishing the viability of using Goldeneye for CO_2 storage.

8. Laboratory procedures and data interpretation

This section discusses a range of detailed laboratory procedural and data interpretation issues and makes recommendations about how these could be further developed in any future SCAL studies of CO_2/brine relative permeabilities and capillary pressure.

8.1. Dopants

As the first reservoir condition test progressed it was observed that the brine phase was becoming discoloured and that the CO_2 had acquired a pinkish hue. Investigation showed that the discoloration of the brine and CO_2 was due to decomposition of the dopant, and not dissolution of minerals within the core. Carbonic acid can react with the sodium iodide to form iodine, which dissolves in the brine and is also solubilised into the CO_2 phase. This reaction potentially invalidates the saturation monitoring. Only the use of the windowed PVT cell as part of the recirculating system allowed this issue to be picked up.

In the subsequent two reservoir condition tests, (Axial Plug PS1 and PS10) the brine was changed out from a sodium iodide doped synthetic formation brine, to a brine doped with caesium chloride.

It was also noted in Section 6.2.1 that a number of the transient in-situ saturation profiles show anomalous behaviour, with calculated saturations going to unphysical values above 1 on a temporary basis behind fronts. For example, **Fig. 6.19** shows what appears to be a bank of increased saturations immediately behind the saturation front. The volume balance work has shown that at least semi-quantitatively, the in-situ saturation data is providing valuable additional insights. In any further SCAL studies for CO_2 storage, it is recommended that the behaviour of the caesium chloride dopant is investigated to identify the causes for the saturation anomalies, with a view to developing procedures to remove them if possible.

8.2. Saturation analysis and initial brine saturation for ambient condition tests

Two sources of saturation data are available for the ambient condition tests:

- Average saturation data based on volume balance data from measured production of fluids from the plugs
- In-situ saturation profiles from the Gamma-ray attenuation data, which also allow core averages to be calculated

The intent of the saturation data analysis is to achieve a basic consistency between the saturation data calculated from volume balance and the independently acquired in-situ saturation data. The situation for the ambient condition Goldeneye displacements is potentially complicated by a number of factors:

- For cores where S_{wi} is achieved in the centrifuge there will be a non-uniform saturation at the end of the run. When the core is then transferred to the core flooding rig this profile may have relaxed to give a uniform profile. Alternatively it is possible that any higher brine saturation at the outlet of the plug may subsequently be displaced by the gas injection during the determination of the relative permeability at S_{wi}.
- During the gas relative permeability measurement the S_{wi} may be partially dried out.

These two factors would mean that the volume balance would overestimate the initial water saturation in the plug prior to the water imbibition flood.

Interpretation of the saturation data is not straightforward because in the early tests the brine used to establish S_{wi} was not doped. This prevents the initial brine saturation being directly calculated using the calibration scans at 100% doped brine and 100% gas. However, after the water flood has been completed the undoped brine will have been fully displaced from the core (as evidenced by the profile for the average in-situ saturation in the core as a function of time).

The preferred analysis method has been to perform the following steps:

1. Endpoint average trapped gas saturation is given by in-situ saturation data (assumed to be reliable given extensive experience of applying this technique in these more straightforward ambient condition tests)
2. Calculate the average initial gas saturation, S_{gi}, before the imbibition flood by adding the produced gas measured in the imbibition test to the average trapped gas saturation calculated from the in-situ saturation data
3. Calculate the initial water saturation as $1-S_{gi}$ (from step 2)
4. Compare the calculated S_{wi} with the S_{wi} obtained by volume balance during the original core preparation (centrifuge or porous plate method)

Fig. 8.1 shows the comparison of the two assessments of S_{wi}. For all the plugs bar one, this shows good consistency, suggesting that any losses of water from the core were limited. The one exception (PS6-1B) shows a calculated S_{wi} which is significantly negative, implying that either the measured trapped gas saturation is too high or the volume of produced gas from the core is over reported. It is interesting to note that this plug gives the highest trapped gas saturation of all the measurements, and that the independent measurement of water relative permeability is fully consistent with a high trapped gas saturation. This gives support to the possibility of an anomalously low S_{wi} in this case. In any case, one possibly anomalous result does not take away from the integrity of the overall dataset that is demonstrated by this analysis, which implies that average saturations are generally accurate to within a few saturation units. On the plots summarising the results in Section6.1 the anomalous point is always shown as an open symbol at zero $S_{wi.}$

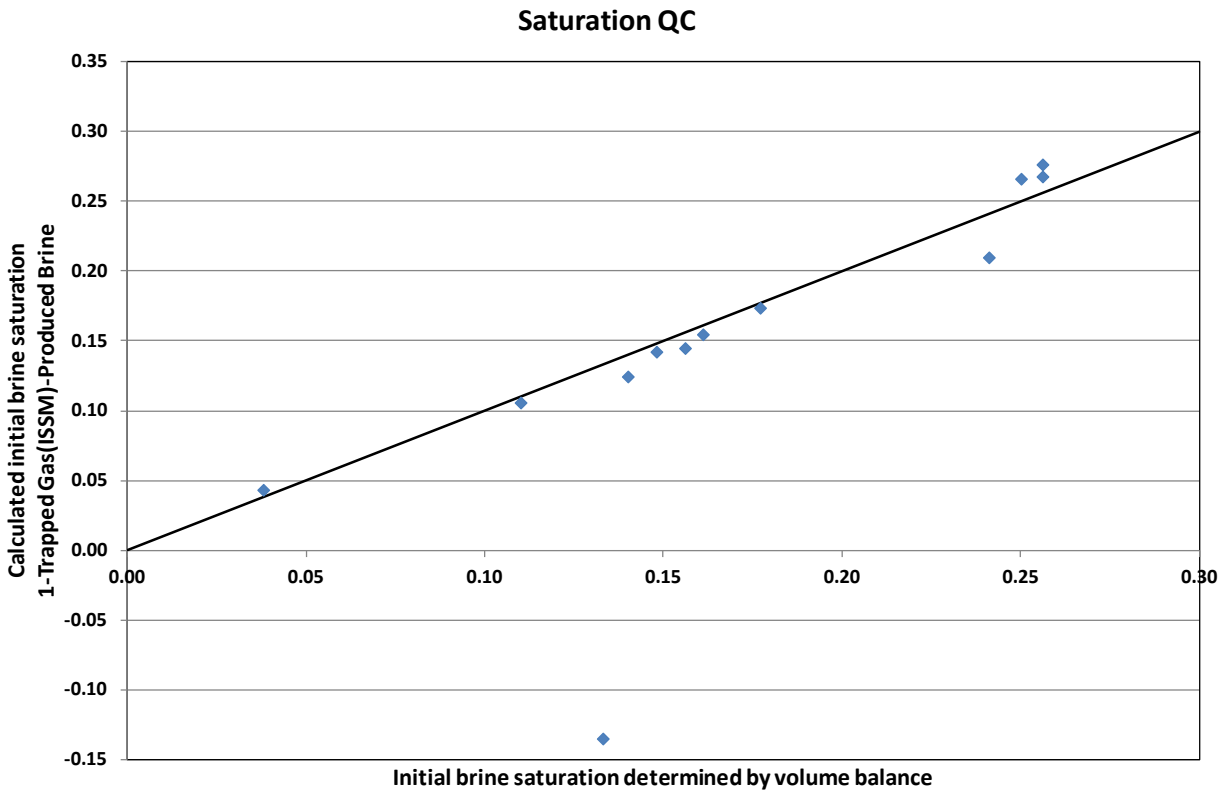

Fig. 8.1—QC of saturation data for ambient condition displacements

For the reservoir condition experiments both volume balance and in-situ saturation measurements are used, but neither initial water saturation, nor trapped gas saturation can be determined with such a high degree of confidence.

8.3. Stripping of trapped gas saturation

Data for water relative permeability was not included for two data points from the new data set, PS9-1b (Module 1) and S5A, because it was found that during clearing of the pressure transducer lines significant additional water had also flooded the plug (as a result of the high plug permeability). In-situ saturation data clearly showed that gas had been lost from the plug during this process, Fig. 6.7, invalidating the relative permeability data. Procedures were revised for subsequent plugs, with the core being valved off during the flushing of the differential pressure lines.

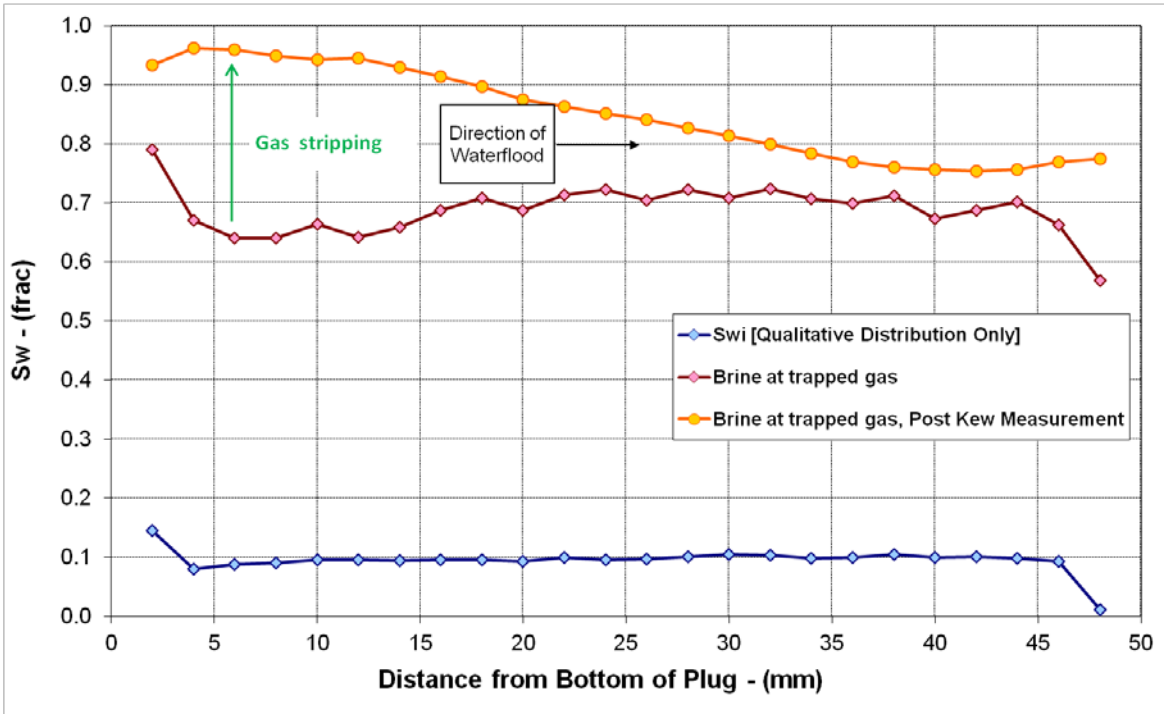

Fig. 8.2—In-situ saturation data for Plug S5A showing stripping of trapped gas saturation observed after the measurement of water relative permeability at trapped gas saturation

It is noted that the final saturation profile after the gas stripping is reminiscent of the data shown in Fig. 3.2 and Fig. 3.3.

9. Glossary of terms

CGR	Condensate gas ratio
CCS	Carbon Capture & Storage
CO_2	Carbon Dioxide
CT	Computer Tomography
FFM	Full Field Model
GIIP	Gas Initially In Place
HC	Hydrocarbon
IFT	Interfacial Tension
PVT	Pressure-Volume-Temperature
SCAL	Special Core Analysis
k_v:k_h	Ratio of vertical to horizontal permeability
SS	Steady State
S_{gi}	Initial gas saturation
S_{gt}	Trapped gas saturation
S_{wi}	Initial water saturation
USBM	United States Bureau of Mines
USS	Unsteady State
QC	Quality Control

Volumes quoted at 'standard conditions' assume temperature of 60°F and pressure of 14.7psia. A conversion of 1 m : 3.28048 ft has been assumed

10. Glossary of Unit Conversions

For the provision of the SI metric conversion factor as applicable to all imperial units in the Key Knowledge Deliverable.

Table 10-1: Unit Conversion Table

Function	Unit - Imperial to SI Metric conversion Factor
Length	1 Foot = 0.3048m Metres 1 Inch = 2.54cm Centimetres 1 Inch = 25.4mm millimetres
Pressure	1 Psia = 0.0690 Bara
Temperature	1°F Fahrenheit = -17.22°C Centigrade
Weight	1lb Pound = 0.45kg Kilogram

Peterhead CCS Project

APPENDIX B

Doc Title: Geomech/(RTM) Core Analysis Report - REPORT ON RESULTS OF LAB EXPERIMENTS (GEO-MECHANICAL INVESTIGATION) : Chemo-mechanical response of Captain Sandstone to CO_2 injection

Doc No. PCCS-05-PT-ZP-9018-00001
Date of issue: 12/09/2014
Revision: K02
DECC Ref No: 11.112
Knowledge Cat: KKD-Subsurface

KEYWORDS

Goldeneye, CO_2, Geomechanics, Core.

Produced by Shell U.K. Limited

ECCN: EAR 99 Deminimus

IMPORTANT NOTICE

Information provided further to UK CCS Commercialisation Programme (the "Competition").

The information set out herein (the "Information") has been prepared by Shell U.K. Limited and its sub-contractors (the "Consortium") solely for the Department of Energy & Climate Change in connection with the Competition. The Information does not amount to advice on CCS technology or any CCS engineering, commercial, financial, regulatory, legal or other solutions on which any reliance should be placed. Accordingly, no member of the Consortium makes (and the UK Government does not make) any representation, warranty or undertaking, express or implied, as to the accuracy, adequacy or completeness of any of the Information and no reliance may be placed on the Information. Insofar as permitted by law, no member of the Consortium or any company in the same group as any member of the Consortium or their respective officers, employees or agents accepts (and the UK Government does not accept) any responsibility or liability of any kind, whether for negligence or any other reason, for any damage or loss arising from any use of or any reliance placed on the Information or any subsequent communication of the Information. Each person to whom the Information is

made available must make their own independent assessment of the Information after making such investigation and taking professional technical, engineering, commercial, regulatory, financial, legal or other advice, as they deem necessary.

Table of Contents

Table of Figs

List of Tables

Executive Summary

The Goldeneye depleted gas condensate field is a candidate for the storage of CO_2. Injection of CO_2 into a reservoir might result in a range of chemical and mechanical effects, and therefore, understanding the possible effect of chemical reactions on the mechanical properties of the reservoir and cap rock is key.

The rock mechanical properties of Captain D Sandstone of the Goldeneye field and the effect of the CO_2-saturated brine flow on them have been studied using samples obtained from Wells 14/29a-3 and 14/29a-5.

This report is an updated and refocused version of the report originally issued for the Longannet CCS Project.

The Goldeneye reservoir consists of a consolidated sandstone (Captain D Sandstone) with only 6 % cement of which 30 % is calcite ($CaCO_3$). It is known that calcite reacts with acidic CO_2-saturated brine, leading to dissolution. Rock mechanical experiments were performed to obtain a range of key mechanical parameters of the host formation, in order to better constrain numerical modelling efforts. In addition, the effect of CO_2-brine-rock interaction on these rock properties was studied, as well as any associated carbonate cement dissolution. The following parameters have been measured during and after the experiments:

- Young's modulus, Poisson's ratio, bulk modulus before and during CO_2 exposure.
- Failure strength under in-situ conditions, after CO_2 exposure.
- Axial V_p and V_s, as well stress and strain sensitivity (*R*- and *S*-factors).
- Pre- and post-experiment sample characterisation: porosity, permeability, microCT scan, XRD and SEM analysis.
- Chemical analysis and pH of effluent.

Important findings of this work are:

i. Calcite was completely dissolved during CO_2-saturated brine flow. This was confirmed by comparison of microCT-scan, XRD and SEM analysis of the pre- and post-experiment sample.
ii. Elemental analysis of the effluent showed an increase of the calcium concentration in the effluent in the first part of the flow phase, indicative of calcite dissolution. In the same part of the flow phase, the pH gradually decreased from pH ~6 to 5, after which it stayed constant for the remainder of the experiment.
iii. No significant change in rock mechanical parameters (Young's modulus, Poisson's ratio, bulk modulus and velocities) was observed in response to the continuous flow of artificial reservoir brine and CO_2-saturated brine.
iv. There was no measurable rock strength reduction as a result of exposure to CO_2-saturated brine, and the concomitant dissolution of calcite.
v. The experiment has shown that P-wave velocity and ultrasonic attenuation are good indicators for supercritical CO_2 coming out of the solution. The S-wave velocity was not sensitive to pore-fluid changes.

The results of these experiments indicate that injecting CO2 into the Captain D Sandstone of the Goldeneye field does not result in a measurable reduction in rock strength.

1. Introduction

This report documents the results of rock mechanical experiments aiming to constrain the key mechanical parameters (Young's modulus, Poisson's ratio and bulk modulus) of rock material of the main reservoir of the Goldeneye field (Captain D Sandstone), and the effect of CO_2-saturated brine on them. The Goldeneye depleted gas condensate field is a candidate for the storage of CO_2. The geological description, lithology and geomechanical aspects of the Goldeneye reservoir are described in detail in reference[1].

Injection of CO_2 into a reservoir might result in a range of chemical and mechanical effects. For an assessment of reservoir and caprock integrity, it is important to understand all possible effects that chemical reactions can have on the mechanical properties of the rocks. For example, if supercritical CO_2 comes in contact with reservoir brine, it will partly dissolve into the formation brine, thereby creating an acidic fluid. This acidic fluid can react with minerals and, amongst others, may lead to the dissolution of carbonate-bearing cement. It is therefore important to understand the potential risks of CO_2 injection, which are:

- Dissolution of carbonate cement may have a weakening effect on the reservoir rock due to a change in the mechanical properties (rock strength, Young's modulus, Poisson's ratio, bulk modulus) of the reservoir formation. Rock strength may be reduced by the loss of cohesion between the sand grains when the cement is removed, i.e. a lowering of the failure envelope.
- Reduction of stiffness and strength of the reservoir rock may induce reservoir deformation.
- Depending on the location where deformation takes place, significant reservoir compaction may lead to well collapse, or to deformation of the overlying cap rock. The latter may fail if deformation becomes too extensive, leading to the creation of leakage pathways.

Analysis has shown that the Captain D Sandstone consists of a consolidated sandstone with about 6 % cement of which ~30 % is calcite ($CaCO_3$). Mechanical experiments were performed to obtain a range of key mechanical parameters of the host formation, in order to better constrain numerical modelling efforts. In addition, the effect of CO_2-saturated brine on these mechanical properties was studied. It is known that calcite dissolves in the presence of acidic CO_2-saturated brine. Therefore, the impact of this dissolution on the strength and stiffness of the carbonate cement was tested under worse-case scenario conditions. The worse-case scenario assumes that if no significant changes in rock-mechanical properties are observed, then no effects would be expected in the field with respect to calcite dissolution. This was achieved by continuously flushing the rock with fresh, unbuffered CO_2-saturated brine. Other, much slower (10 to 100s of years) chemical reactions, such as dissolution and reaction of feldspar and clay minerals, are not assessed in the present experiment. The following parameters have been determined:

- Young's modulus, Poisson's ratio, bulk modulus before and during CO_2 exposure.
- Failure strength under in-situ conditions, after CO_2 exposure.
- Axial V_p and V_s, as well strain and stress sensitivity (R- and S-factors respectively).
- Pre- and post-experiment sample characterisation: porosity, permeability, microCT scan, XRD and SEM analysis.

[1] PCCS-05-PT-ZG-0580-00004 - Goldeneye Static Model (Field), Key Knowledge Deliverable 11.108

- Chemical analysis and pH of effluent.

Where: V_p = compressional velocity

V_s = shear wave velocity

microCT = micro-Computer Tomography

XRD = X-ray Diffraction

SEM = Scanning Electron Microscopy

In Chapter 2, details of sample preparation and experimental procedure are described. Results of the mechanical properties obtained in the presence of brine and CO_2-saturated brine are presented in Chapter 3, with the implications of our results in Section 3.4.5. Conclusions are given in Chapter 4.

2. Experimental Procedure

Reservoir rock (Captain D Sandstone) from Wells 14/29a-3 and 14/29a-5 was received in the form of three plugs (samples PSx_1C; ~37.5 mm diameter and ~86 mm in length) and core, from which three more samples were drilled (samples GE_xxV). **Table 2-1** shows a summary of the location and depth from which the samples were obtained, as well as transport parameters (porosity and permeability). It should be noted that samples PS9_1C and PS17_1C still contained residual fluid and no attempts were made to remove this. The samples obtained from core were dry.

Table 2-1—Location, retrieval depth and transport properties of the samples used in the mechanical experiments

Sample name	Well location	Depth [m]	Porosity [-]	K_w [mD]	Comment
GE_01V	14/29a-3	2968.5	0.292	2100	Only mechanical properties measured, no CO_2
GE_02V	14/29a-5	2602.0	0.276	740	
GE_03V	14/29a-5	2602.6	0.266	650	
PS6_1C	14/29a-3	2979.6	n.d	1996	Sample failed in initial phase of the experiment
PS9_1C	14/29a-3	2991.5	0.264	1709	Flushed with CO_2-saturated brine
PS17_1C	14/29a-3	3014.6	n.d.	898	

Note K_w = permeability

2.1. In-situ stress conditions

The estimated in-situ total and effective stresses at depth are listed in **Table 2-2**. The experiments were performed at a pore pressure of 14 MPa, and effective in-situ conditions as given in Table 2-2. Note that although the total stresses and pore pressure used in the lab experiments differ from those under in-situ conditions, the effective stresses (i.e. total stresses minus pore pressure) are the same in both cases.

2.2. Pre-experimental procedure

Because of the friable nature of the core material, samples were kept frozen during set-up of the experiment. The samples were trimmed to 76 mm length. Teflon shrink tubing was placed around the sample. Two small holes were cut in the teflon sleeve to accommodate the placement of several radial displacement transducers in direct contact with the sample. A HNBR rubber sleeve was placed around the teflon coated sample. The teflon sleeve was necessary to reduce CO_2 diffusion through the HNBR sleeve. Note that a slightly modified procedure was used for samples GE_01V and GE_03V, which were only covered by a Viton sleeve, as these experiments were performed at room temperature. After mounting the sample into the apparatus, an isostatic load of 2 MPa was applied to the sample ($S_{ax} = P_{rad} = 2$ MPa) and the sample was left to thaw for ~70 hrs. After thawing, the sample was vacuum-saturated with artificial reservoir brine. The composition of the synthetic formation brine used in the mechanical experiments is given in **Table 2-3.**

Table 2-2—In-situ stress conditions within the Goldeneye field and experimental conditions for the mechanical lab experiments.

	Total stresses prior to reservoir depletion		Effective stresses prior to reservoir depletion	Total stresses at time of CO_2 injection		Effective stresses at time of CO_2 injection
	In-situ [MPa]	Lab test [MPa]	$S_i - P_{pore}$ [MPa] (for both in-situ and lab test)	In-situ [MPa]	Lab test [MPa]	$S_i - P_{pore}$ [MPa] (for both in-situ and lab test)
Total vertical stress ($S_V = S_{ax}$)	54.0	41.6	27.6	51.5	42.5	28.5
Horizontal stress ($S_H = P_{rad}$)	49.2	36.8	22.8	38.0	29.0	15.0
Pore pressure	26.4	14.0		23.0	14.0	
Pore pressure at max depletion	14.9	3.7				

2.3. Experimental procedure, data acquisition and analysis

The experiments were performed using a triaxial compression apparatus. Appendix 1 provides a schematic overview of the triaxial machine and the CO_2 flow loop. We performed two sets of experiments:

1) Mechanical properties measurements: these measurements aimed to better constrain the range of values for the key mechanical parameters (e.g. Young's modulus, Poisson's ratio and bulk modulus) for Captain D Sandstone.
2) CO_2-saturated brine flow experiments: these experiments aimed to determine the effect of carbonate (cement) dissolution on the mechanical strength of the material.

In the case of the experiments performed using CO_2-saturated brine (PSx_1C series), the apparatus was equipped with a CO_2 flow loop. For this type of experiment, artificial reservoir brine was saturated with supercritical CO_2 in a 300 ml autoclave at 35 to 40°C and a CO_2 pressure of ~7.2 MPa,

prior to being introduced into the sample. The CO_2-saturated brine was pumped through the core sample at a constant flow rate (0.025 to 0.06 ml/min) using a Quizix® pump. A second Quizix® pump at the effluent-side of the flow loop was used to maintain a constant pore fluid pressure of 14 MPa. After each 10 ml intake of the latter pump, the pump reservoir was emptied and the effluent was collected for analysis. The total amount of effluent collected within one day was combined and analysed for elemental composition and pH.

Table 2-3: Artificial brine composition used in the experiments. The composition is based on analysis of water samples from the Goldeneye field.

	NaCl	$MgCl_2$	KCl	$CaCl_2$	$CaCO_3$
Conc. [g/l]	50.89	0.97	0.46	2.36	0.78

A schematic stress path (S_{ax}, P_{rad} and P_{pore} versus relative time), as used in the experiments, is shown in Fig 2-1. As can be seen, the test consisted of up to five different stages. For the GE_xxV series, stress paths up to the point of brine flow were followed (i.e. up to step 3). For the CO_2-saturated brine flow experiments (PSx_1C series), all five steps were followed, which consisted of:

1) Establishing in-situ stress conditions: After mounting, thawing and vacuum saturating the sample with artificial brine (see section 2.1), the sample was taken to the desired effective stress conditions in four steps: (a) isostatic loading at constant pore pressure to $S_{ax} = P_{rad} = 8.5$ MPa, $P_{pore} = 0.5$ MPa; (b) loading at constant effective stress (identical stress increments for axial and radial stress and pore pressure) to $S_{ax} = P_{rad} = 36.6$ MPa, $P_{pore} = 28.6$ MPa; (c) isostatic loading at constant pore pressure to $S_{ax} = P_{rad} = 39.2$ MPa, $P_{pore} = 28.6$ MPa, while determining the rock bulk modulus; (d) triaxial loading at constant radial stress and constant pore pressure to in-situ stresses, $S_{ax} = 41.9$ MPa, $P_{rad} = 36.8$ MPa, $P_{pore} = 14.0$ MPa, while determining Young's modulus and Poisson's ratio. Once the appropriate in-situ stress conditions were obtained, the sample temperature was raised to ~ 60°C and the sample was left to consolidate for 24 hr. This temperature was maintained throughout the whole experiment.
2) Pore-pressure-depletion cycles: Two pore pressure depletion/inflation cycles were performed under uniaxial strain conditions. The depletion/inflation cycles were performed in two steps, each step followed by a consolidation period of at least 12 hrs to study the creep behaviour and irreversible compaction. In the depletion steps, the pore pressure was reduced from $P_{pore} = 14$ MPa to 3.7 MPa and the radial stress from 36.8 MPa to 28.1MPa, mimicking reservoir depletion. During the pore pressure inflation steps, pore pressure was increased back to $P_{pore} = 14$ MPa, while P_{rad} was increased again to 36.8 MPa. During the depletion/inflation cycles, the axial total stress was kept constant.

   After the second pore pressure depletion/inflation cycle, axial stress was increased to 42.9 MPa and radial stress was reduced to 29 MPa to simulate the stress state at the start of CO_2 injection. This procedure was again followed by a consolidation period. Rock mechanical parameters were determined prior to start of the flow stages, through a small axial unload/load cycle (i.e. S_{ax} reduced to 38.5 MPa and back to 42.9 MPa).
3) Brine flow stage: Artificial reservoir brine was flowed through the sample at a rate of 0.06 ml/min. Brine flow was stopped when no significant creep behaviour of the sample was observed anymore. After creep had ceased, another axial unload/load cycle was performed to determine rock mechanical parameters.

4) CO_2-saturated flow stage: Artificial brine was saturated with supercritical CO_2 and flowed through the sample at a constant rate (0.025 or 0.06 ml/min). Every 10 ml of effluent was collected for analysis. Four axial unload/load cycles, to determine rock mechanical parameters, were performed during this stage.
5) Triaxial failure: After CO_2-saturated brine flow was stopped, the axial load on the sample was increased at a rate of 10 MPa/hr until failure occurred. P_{rad} and P_{pore} were kept constant at 29.0 MPa and 14.0 MPa, respectively.

It should be noted that sample PS6_1C failed prematurely prior to the second pore pressure depletion/inflation cycle. Therefore, no CO_2-saturated brine flow was established for this specific sample. During the experiments, stresses, axial and radial displacements were recorded continuously. Corrections were made to the raw data to correct for apparatus distortion. For each loading/unloading step rock-mechanical properties (bulk modulus, Young's modulus and Poisson's ratio) were determined from the slopes of stress-strain curves (averaged over the loading/unloading time, not including the creep phase), using linear elastic theory for isotropic materials.

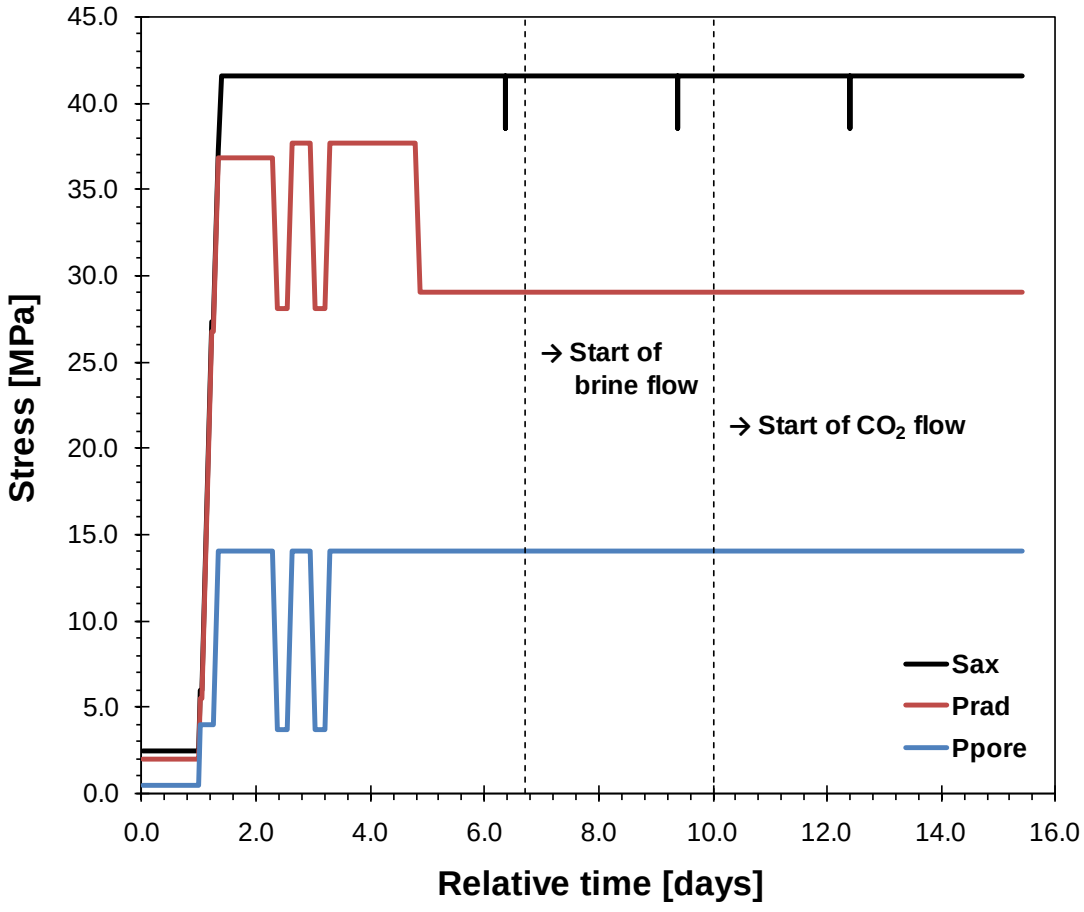

Fig 2-1 —Simplified stress path for the geomechanical experiments performed.

In addition, travel times for ultrasonic axial compressional and shear waves were measured by the pulse-transmission technique at regular time-intervals, and used to calculate V_p and V_s. For each

loading/unloading step, R and S, were determined from the average slopes of the velocity-strain and velocity-effective stress curves, respectively. R and S factors are determined for axial V_p and axial V_s and defined as follows[2]:

$$\text{Strain sensitivity factor: } R\,[-] = [\Delta V_i / V_i]/\Delta\varepsilon_{ax} \quad (1)$$

$$\text{Stress sensitivity factor: } S\,[\text{GPa}^{-1}] = [\Delta V_i / V_i]/[\Delta(S_{ax} - P_{pore})] \quad (2)$$

3. Results and Discussion

We performed two series of experiments: 1) to estimate the variability in key mechanical parameters of Captain D Sandstone reservoir rock, and 2) to determine the effect of chemical CO_2-brine-rock interaction on the mechanical properties. A summary of all mechanical properties measured during these experiments is shown in **Table 3-1** and **Table 3-2.**

3.1. Pore pressure depletion/inflation cycles

All samples showed a minor amount of irreversible (non-elastic) creep during the consolidation period following the first depletion stage. After the first depletion phase, all samples showed a linear and reversible strain-effective stress relationship **(**Fig. 3-1**)**. No pore collapse was observed during the experiments. In order to obtain the key rock mechanical parameters (E, ν and K_b) from these measurements, linear elastic theory was applied to the axial and radial strain, and the axial and radial effective stress data3, assuming the samples to be isotropic. It should be noted that Young's modulus E, Poisson's ratio ν and bulk modulus K_b obtained in the first depletion steps were approximately 30 to 70 % lower than the values obtained in the second pore pressure depletion/inflation cycle **(**see **Fig. 4.2).** Overall, the average values for the mechanical parameters, obtained from the inflation phase of the first cycle and the second depletion/inflation cycle, amounted to E = 15.8 ± 2.2 GPa, ν = 0.25 ± 0.03 and K_b = 10.6 ± 1.9 GPa. An overview of the rock mechanical parameters found in the pore pressure depletion/inflation cycles is given in Table 3-1.

[2] A. Bauer, B.C. Lehr, J.W. Dudley, S. de Vries, M.A. Addis, F. Korndorffer, A.J. van der Linden, D.K. Love, M.T. Myers, N. Yassir, C. Kenter 2007. Stress Dependence of Velocities in Shales: Deployment in 4D Seismics, EP 2007-5720.

[3] E. Fjaer et al. 2008. *Petroleum related rock mechanics*, 2nd edition, Amsterdam: Developments in Petroleum Science 53, Elsevier.

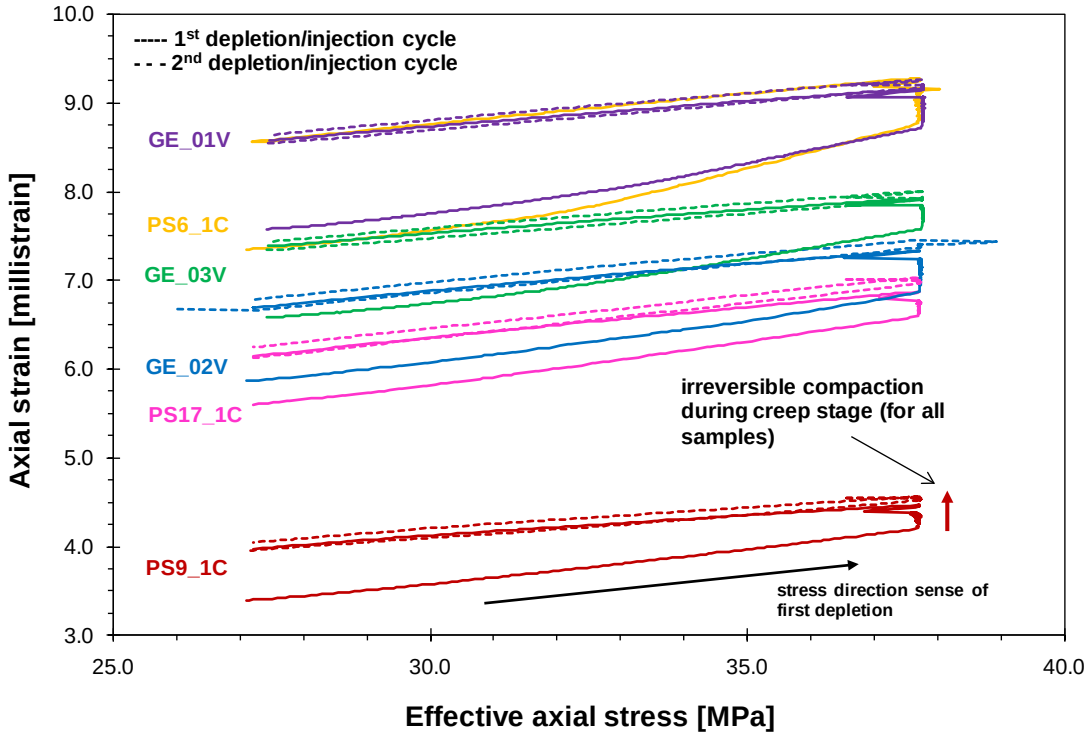

Fig. 3-1—Stress strain plot for pore pressure depletion steps.

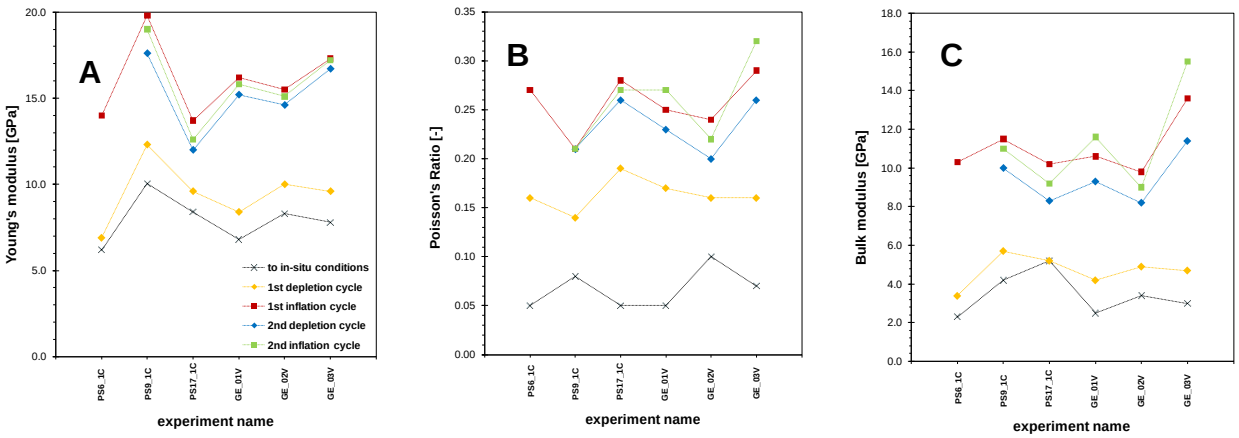

Fig. 3-2—Overview of the rock mechanical properties obtained during the pore pressure depletion/inflation cycles of the experiments: A) Young's modulus; B) Poisson's ratio; C) bulk modulus.

For V_p and V_s, linear relationships with effective axial stress and axial strain were found, showing that with increasing stress or strain, axial and radial velocities increased **(Fig. 4-3).** Ultrasonic velocities at in-situ stress amounted to 3387 to 3584 m/s for V_p and 1690 to 2030 m/s for V_s. The strain sensitivity of V_p, the *R*-factor, and the stress sensitivity, the *S*-factor were calculated using the slopes of the normalized velocity, $V_p/V_{p,0}$, vs. axial strain and axial effective stress curves,

respectively. As the first depletion cycle consistently showed different mechanical behaviour from the subsequent stages/cycles, we omitted those data from our calculations. For *R*-factors, we found $R = 12.7 \pm 5$ for V_p, and $R = 21.4 \pm 6$ for V_s. For the stress sensitivity of velocities, we found *S*-factors of 0.8 ± 0.2 GPa^{-1} for V_p and 1.4 ± 0.3 GPa^{-1} for V_s. An overview of the ultrasonic velocity data, and the corresponding *R*- and *S*-factors, for the pore pressure depletion/inflation cycles is given in **Table 3-1**. Note that velocities obtained for the depletion stages were taken at maximum effective stress (i.e. maximum pore pressure depletion), while the velocities stated for the inflation stages were taken at minimum effective stress (i.e. maximum pore pressure inflation).

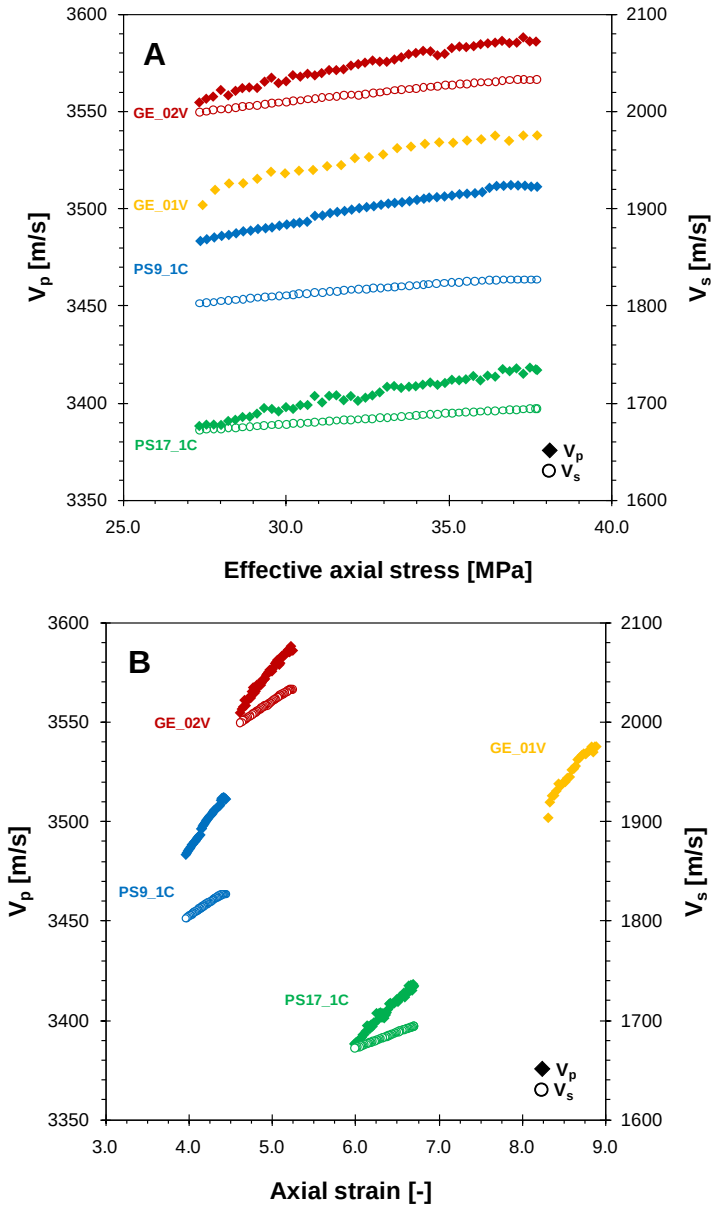

Fig. 3-3—Ultrasonic velocity (V_p and V_s) data for the first pore pressure inflation cycle of the mechanical parameter experiments: A) V_p and V_s vs. effective axial stress; B) V_p and V_s vs. axial strain.

Table 3-1—Mechanical parameters and ultrasonic velocity data determined for the pore pressure depletion/inflations cycles.

Sample name	GE_01V	GE_02V	GE_03V	PS6_1C	PS9_1C	PS17_1C
To in-situ conditions						
E [GPa]	6.8	8.3	7.8	6.2	10.0	8.4
ν [-]	0.05	0.10	0.07	0.05	0.08	0.05
K_b [GPa]	2.5	3.4	3.0	2.3	4.2	5.2
α_{axial} [10^6 K^{-1}]		10.4		14.4		
α_{radial} [10^6 K^{-1}]		17.9		10.4	10.8	
T [°C]	21	62	21	62	62	62
1st pore pressure depletion cycle						
E [GPa]	8.4	10.0	9.6	6.9	12.3	9.6
ν [-]	0.17	0.16	0.16	0.16	0.14	0.19
K_b [GPa]	4.2	4.9	4.7	3.4	5.7	5.2
V_p [m/s]	3533	3580		3251	3504	3415
S_{Vp} [GPa^{-1}]	0.8	0.6		0.3	0.7	0.4
R_{Vp} [-]	13.2	6.1		1.9	8.8	4.3
V_s [m/s]		2022			1821	1691
S_{Vs} [GPa^{-1}]		1.7			1.4	1.0
R_{Vs} [-]		17.7			18.0	10.8
1st pore pressure inflation cycle						
E [GPa]	16.2	15.5	17.3	14.0	19.8	13.7
ν [-]	0.25	0.24	0.29	0.27	0.21	0.28
K_b [GPa]	10.6	9.8	13.6	10.3	11.5	10.2
V_p [m/s]	3509	3556			3485	3388
S_{Vp} [GPa^{-1}]	0.9	0.9			0.8	0.8
R_{Vp} [-]	15.5	14.3			17.6	12.3
V_s [m/s]		1999			1803	1672
S_{Vs} [GPa^{-1}]		1.7			1.4	1.3
R_{Vs} [-]		27.8			29.7	18.8

Table 4-1 (continued)—Mechanical parameters and ultrasonic velocity data determined for the pore pressure depletion/inflations cycles.

Sample name	GE_01V	GE_02V	GE_03V	PS6_1C	PS9_1C	PS17_1C
2nd pore pressure depletion cycle						
E [GPa]	15.2	14.6	16.7		17.6	12.0
ν [-]	0.23	0.20	0.26		0.21	0.26
K_b [GPa]	9.3	8.2	11.4		10.0	8.3
V_p [m/s]	3536	3584			3512	3416
S_{Vp} [GPa^{-1}]	0.9	0.8			0.9	0.8
R_{Vp} [-]	14.7	12.0			19.2	10.3
V_s [m/s]		2030			1843	1690
S_{Vs} [GPa^{-1}]		1.4			1.3	1.0
R_{Vs} [-]		20.9			27.9	12.8
2nd pore pressure inflation cycle						
E [GPa]	15.8	15.1	17.2		19.0	12.6
ν [-]	0.27	0.22	0.32		0.21	0.27
K_b [GPa]	11.6	9.0	15.5		11.0	9.2
V_p [m/s]	3502	3552			3478	3387
S_{Vp} [GPa^{-1}]	1.0	1.0			0.9	1.0
R_{Vp} [-]	16.0	15.7			17.2	13.0
V_s [m/s]		2000			1801	1668
S_{Vs} [GPa^{-1}]		1.8			1.4	1.4
R_{Vs} [-]		28.2			26.0	18.3

3.2. Brine flow and CO_2-saturated brine flow stages

After the two pore pressure depletion/inflation cycles, samples PS9_1C and PS_17C were taken to the same effective stress conditions as at which CO_2 injection will take place at the Goldeneye storage site (S_{ax}^{eff} = 28.5 MPa, P_{rad}^{eff} = 15 MPa - see **Table 2-2**).

Fig. 3-6 shows the radial and axial strain measured during both flow phases of the experiments as a function of cumulative fluid flow (i.e. equivalent time). Overall, very minor (< 0.1 millistrain) of deformation is observed in either the axial or radial direction. Note that no enhanced deformation is observed during the CO_2-saturated brine flow, compared to the brine flow stage, though sample PS17_1C showed some fluctuations in radial strain.

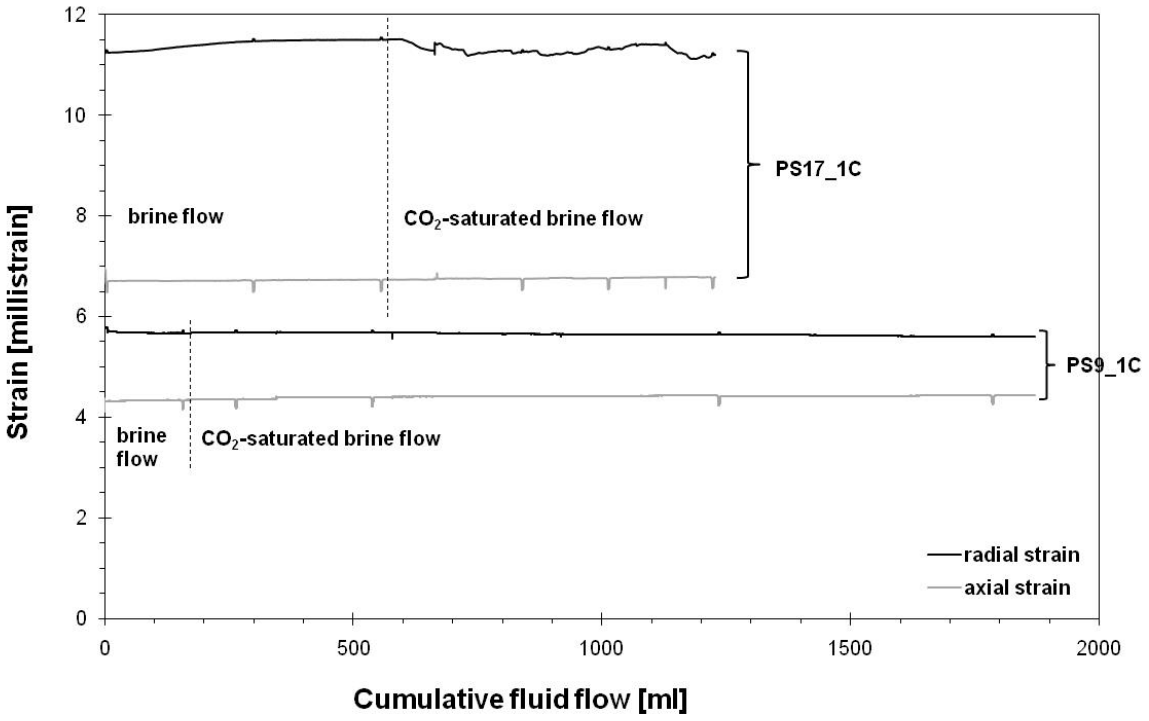

Fig. 3-4—Axial and radial strain during the flow phases of the experiment.

Like during the pore pressure depletion/inflation stages, stress cycles were performed prior to, during and at the end of brine flow and another four during the stage of CO_2-saturated brine flow. The results were again used to determine the key rock mechanical parameters (E, ν, K_b) and R- and S-factors for V_p and V_s. Throughout both flow phases, Young's modulus, Poisson's ratio and bulk modulus showed no significant change. Overall, average values for the rock mechanical properties are E = 18.4 ± 3.1 GPa, ν = 0.22 ± 0.03 and K_b = 11.2 ± 3.1 GPa. For the P-wave and S-wave velocities, a similar behaviour is found, with R-factors of 30.0 ± 1.9 for V_p and 24.1 ± 2.7 for V_s, and S-factors of 1.4 ± 0.3 GPa^{-1} for V_p and 1.2 ± 0.3 GPa^{-1} for V_s. All rock mechanical properties, ultrasonic velocity data and corresponding R- and S-factors are summarised in Table 3-2.

The ultrasonic velocity data showed that P-wave velocity proved to be sensitive to pore fluid type. This was evident from the results of experiment PS9_1C, which had a slightly different procedure for preparation of the CO_2-saturated brine. During the initial CO_2-saturated brine flow stage of the experiment (up to 600 ml of CO_2-saturated brine; ~ 750 ml cumulative fluid flow), 250 ml of brine was mixed with 50 ml of supercritical (SC) CO_2 at ~ 7 MPa total pressure and 35°C, i.e. a CO_2-brine volume ratio of 1:5. However, upon fluid flow, the autoclave pressure dropped relatively fast to 5 MPa, as the relatively small amount of SC CO_2 was not able to maintain pressure upon brine removal from the autoclave. As the total pressure in the autoclave dropped, the CO_2 changed from the supercritical to the gaseous phase, and the concentration of CO_2 in the brine decreased (see

Fig. 4-2 in Appendix 1). To prevent this in the further stages of the experiment and the second experiment (PS17_1C), the volume of brine fed into the autoclave was reduced to 200 ml, while the volume of SC CO_2 was increased to 100 ml, i.e. a CO_2-brine volume ratio of 1:2. With this CO_2-brine

ratio, the pressure in the autoclave stayed above ~6.3 MPa, keeping the CO_2 in the supercritical phase. However, the change in CO_2-brine ratio and total pressure resulted in a slightly higher CO_2 concentration in the CO_2-saturated brine that was introduced into the sample than in the initial stages of the experiments.

Table 3-2—Mechanical parameters and ultrasonic velocity data determined for the experiments flushed with brine and CO_2-saturated brine.

cum. ml of fluid flow	E [GPa]	ν [-]	K_b [GPa]	V_p [m/s]	S_{Vp} [GPa^{-1}]	R_{Vp} [-]	V_s [m/s]	S_{Vs} [GPa^{-1}]	R_{Vs} [-]
PS9_1C									
Brine flow									
160	21.7	0.24	13.6	3442	1.1	30.3	1764	1.0	26.8
CO_2-saturated brine flow									
260	21.5	0.25	14.4	3435	1.1	29.8	1755	0.9	22.8
540	21.4	0.27	15.3	3434	1.1	29.9	1758	0.7	18.8
1230	21.3	0.24	14.0	3404	1.1	31.1	1758	1.0	27.4
1780	21.9	0.25	14.6	3416	1.3	32.1	1754	1.1	27.2
PS17_1C									
Brine flow									
300	14.2	0.18	7.4	3341	1.5	27.7	1625	1.2	22.6
550	15.4	0.20	8.5	3342	1.6	27.4	1625	1.3	21.2
CO_2-saturated brine flow									
840	16.0	0.19	8.8	3335	1.6	28.4	1614	1.3	22.8
1010	16.2	0.19	8.6	3333	1.7	31.4	1616	1.3	25.0
1130	16.5	0.19	8.8	3331	1.7	31.3	1618	1.5	26.8
1220	16.2	0.21	9.5	3325	1.6	28.8	1612	1.5	27.3

Under the experimental conditions, total pore pressure of 14 MPa and a temperature of 60°C, CO_2 is slightly less soluble in water than under the conditions at which the solution was mixed (see

Fig. 4-2 in Appendix 1). Therefore, in the first experiment (PS9_1C), upon entering the sample, a small amount of CO_2 dissolved in the brine potentially came out of solution. Fig. 3-5 shows several axial P-waveforms obtained during this experiment, as a function of the amount of cumulative volume of fluid flow. As can be seen, the amplitude of the P-waveform acquired during the brine flow is similar to the amplitudes obtained during the initial stage of the CO_2-saturated brine flow **(**340 and 570 ml cumulative volume of fluid flow)After changing the CO_2-brine ratio, a reduction of the ultrasonic P-wave signal of approximately 45 % was observed (cf. 920 ml and 1470 ml of cumulative

volume of fluid flow). In addition, a small drop in P-wave velocity from ~3440 m/s to ~3420 m/s was noted, as well as a shift in zero-crossing, indicative for a change in wave travel time. This was most likely caused by the change from a single phase (CO_2-saturated brine) to a two-phase (SC CO_2 plus CO_2-saturated brine) fluid system, as SC CO_2 has a lower bulk modulus than a single-phase CO_2-saturated solution. It should be noted that the axial S-wave did not change significantly (V_s = 1759 ± 4.9 m/s) during both flow phases, as shear waves are less affected by changes in pore fluid properties.

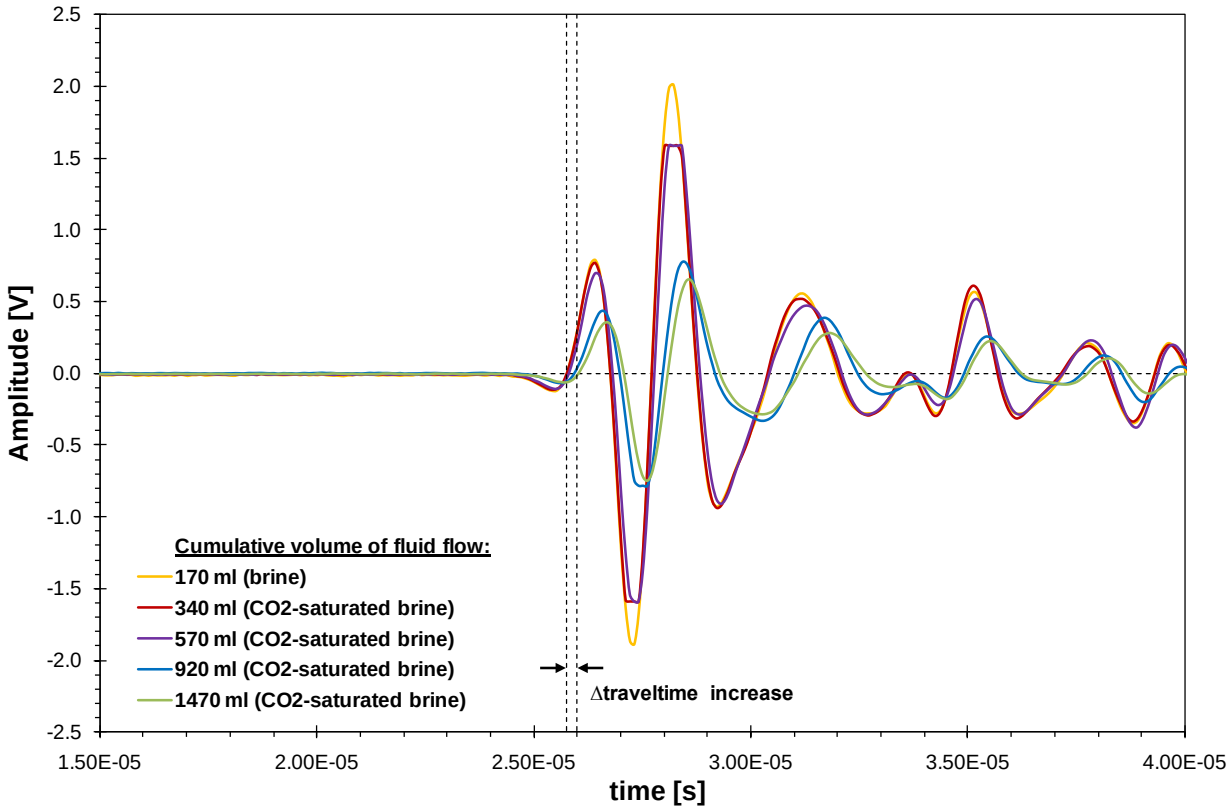

Fig. 3-5—Axial P-wave forms for experiment PS9_1C showing amplitude attenuation and travel time increase, as a result of CO_2 coming out of solution.

3.3. Triaxial failure

The last step of experiments PS9_1C and PS17_1C consisted of measuring the failure strength of the samples, after continuous flushing with CO_2-saturated brine, and the (expected) concomitant dissolution of carbonate present in the material. The axial stress on the samples was increased (ΔS_{ax} = 10 MPa/hr), while keeping P_{pore} = 14.0 MPa and P_{rad} = 29.0 MPa, until shear failure occurred. For samples PS9_1C and PS17_1C, brittle shear failure occurred at an axial total stress of 80.2 and 74.9 MPa, respectively **(**see

Fig. 3-6). After terminating the experiment, axial, radial and pore pressure were carefully removed, the sample was cooled down and gently removed from the apparatus, in order to cause no further disturbance to the sample.

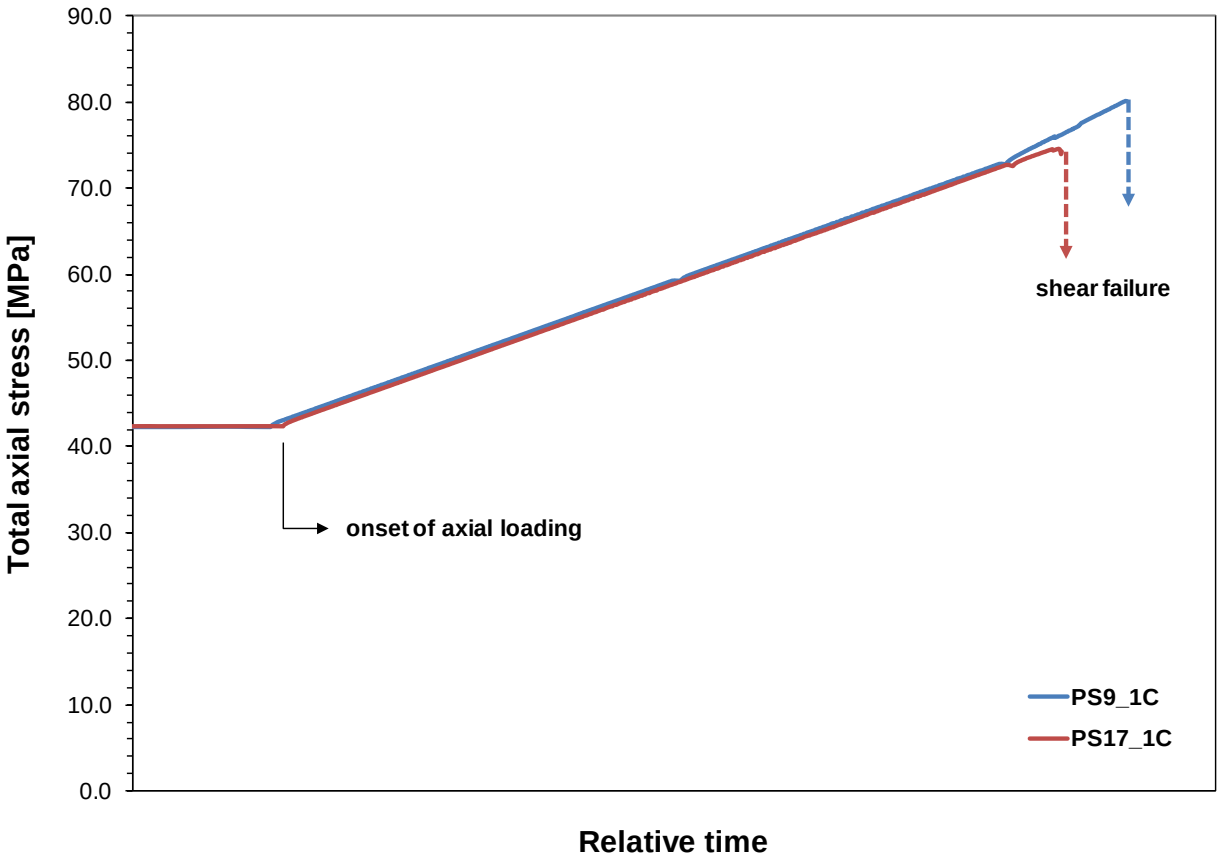

Fig. 3-6—Total axial stress vs. relative time for the shear failure stage (step 5) of experiments PS9_1C and PS17_1C

In order to confirm that dissolution of the carbonate (cement), present in the starting material, occurred, we performed microCT scan, SEM, XRD and effluent analysis of the pre- and post-experiment material. The results of these analyses are described in the next section.

3.4. Microscopic and chemical analysis

SEM and XRD analysis of samples PS9_1C, and microCT scan analysis and chemical analysis of the effluents of experiments PS9_1C and PS17_1C were performed, in order to confirm or refute the dissolution of carbonate (calcite) in our experiments. Part of sample PS9_1C was impregnated with resin, prior to analysis, for the preparation of polished thin sections used for SEM analysis. Sample preparation and analytical procedures are given in Appendix 2.

3.4.1. MicroCT scan analysis

Full core microCT scans of both samples pre- and post-experiment were performed. In CT images, grey values represent the X-ray attenuation of the rocks: white corresponding to high attenuation, black to low attenuation. In essence, denser rock, or rock composed of minerals rich in heavier elements, show higher X-ray absorption. The samples were scanned along radial sectional planes and axial orthogonal planes. In the pre-experiment and post-experiment images shown in **Fig. 3-7**, the

sandstone matrix is shown in various shades of grey. In the pre-experiment images, bright spots in the images represent calcite, siderite or pyrite inclusions, as verified by SEM-EDX. In the post-experiment CT scans, many of the bright areas/spots associated with calcite had disappeared, due to dissolution by the acidic CO_2-saturated brine.

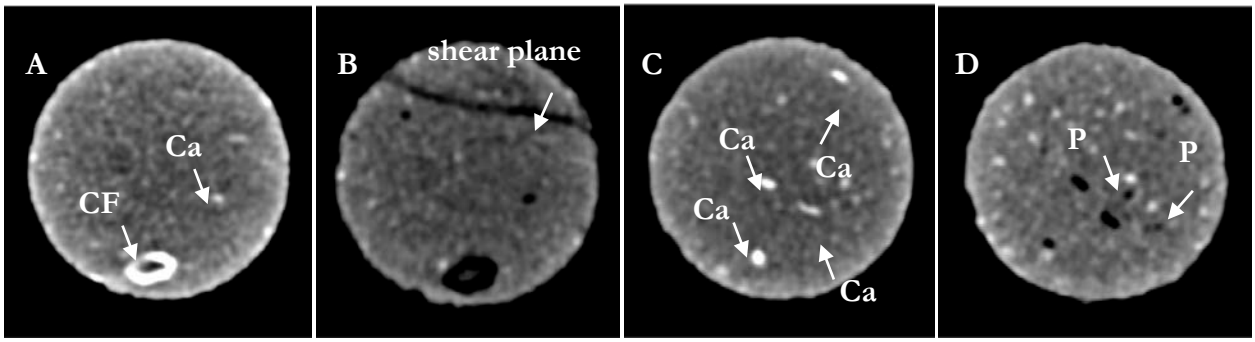

Fig. 3-7—MicroCT scanning images of sample PS9_1C A) pre-experiment and B) post-experiment, and sample PS17_1C C) pre-experiment and D) post-experiment. Ca denotes calcite, CF denotes carbonate fossil and P denotes pyrite.

3.4.2. SEM analysis

Both fresh sample surfaces and polished, thin sectioned sample material (PS9_1C) were studied. Images made from the polished thin section using back-scanning electron microscopy (BSEM) show grey scale variations representing the various types of minerals: heavy minerals are lighter in colour, quartz is basic grey and lesser abundant feldspar grains are lighter grey in colour. In addition, Energy Dispersive X-ray (EDAX) analysis was performed for mineral identification. Below, we present the SEM analysis of sample PS9_1C.

3.4.2.1. Pre-experiment analysis

The poorly sorted character of the pre-experiment sandstone sample is seen in Fig.4.8, where some large grains are broken. The larger grains are up to 1 mm in size and often very well rounded, while smaller grains are more angular. Locally re-precipitated (diagenetic) quartz was observed in the form of irregular ("teeth-like") grain coatings on detrital grains (Fig.4-8b). Overall, many detrital (quartz) grains show long grain boundaries and numerous concavo-convex grain-to-grain boundaries, as clearly seen in the BSEM images (Fig.4-8c and d). Minor calcite cement occurs in the pre-experiment sample between detrital grains (Fig.4-8c). Large areas containing calcite were not encountered in the pre-experiment samples, although poly-crystalline siderite (iron-rich carbonate) was observed .

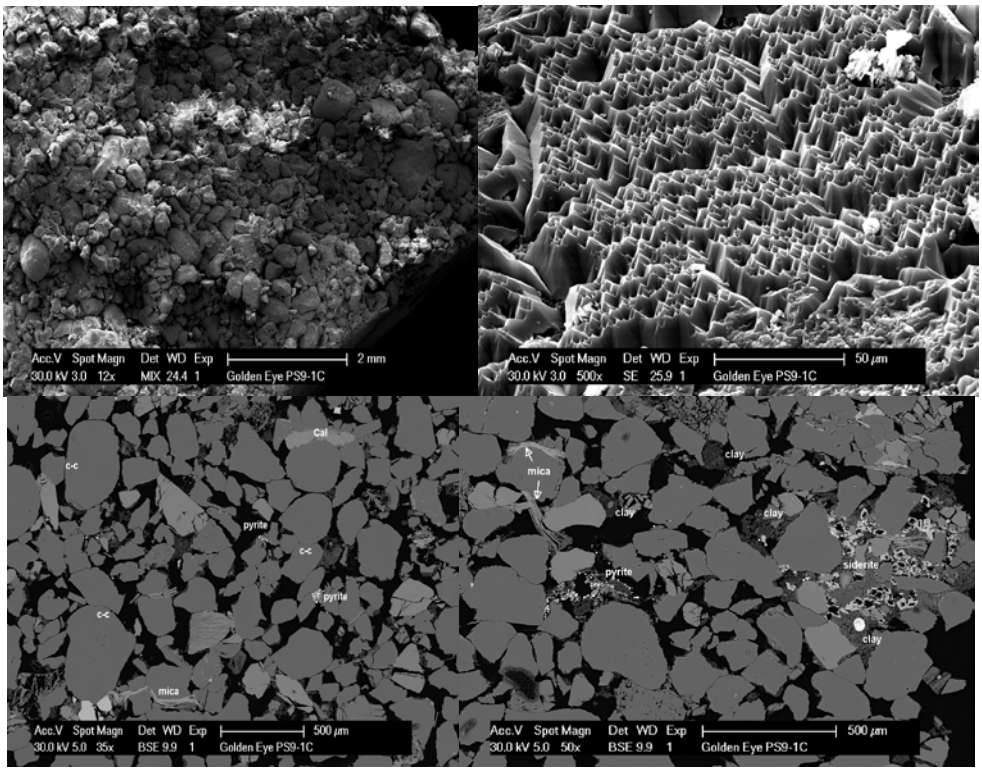

Fig. 3-8—A) SEM overview image showing the poorly sorted character of the sandstone; B) High magnification (500 x) SEM images of detrital grain surfaces displaying secondary quartz in the form of small "teeth-like" crystal faces pointing into the pores; C) BSEM image of the pre-experiment material showing the long grain-to-grain contacts (c-c), aggregates of small framboidal pyrite and minor calcite (Cal) cement; D) BSEM image of the pre-experiment material showing clay cement, framboidal pyrite and a large concentration of small euhedral siderite crystals.

3.4.2.2. Post-experiment analysis

After the experiment, the porosity of the sample is still high, and local pore-filling clay aggregates of kaolinite and chlorite occur. Essentially, SEM analysis has shown that calcite does not occur in the sample after continuous flushing with CO_2-saturated brine.

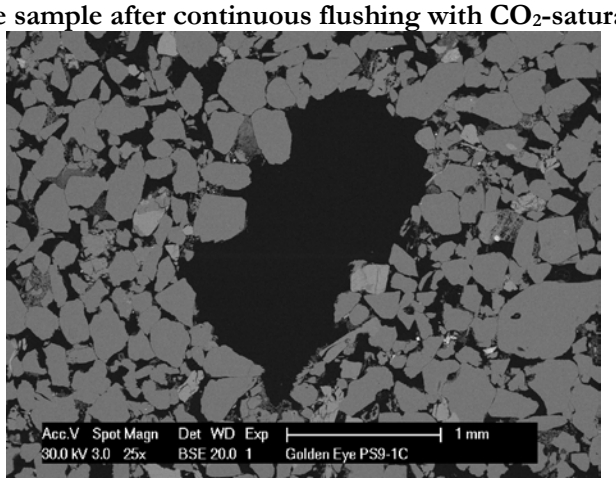

Fig. 3-9 shows a BSEM image displaying a large hole in the post-experiment sample. The presence of such a hole coincides with the observation of dissolved large particles, as seen in the microCT scans of the pre- and post-experiment sample. Note that the material did not collapse around these cavities. It is possible that the angular, teeth-shaped secondary quartz covering the detrital grains, as well as the concavo-convex grain-to-grain contacts, prevented shifting and rotation of the grains during the compaction experiment, while calcite cementation did not significantly contribute to rock strength.

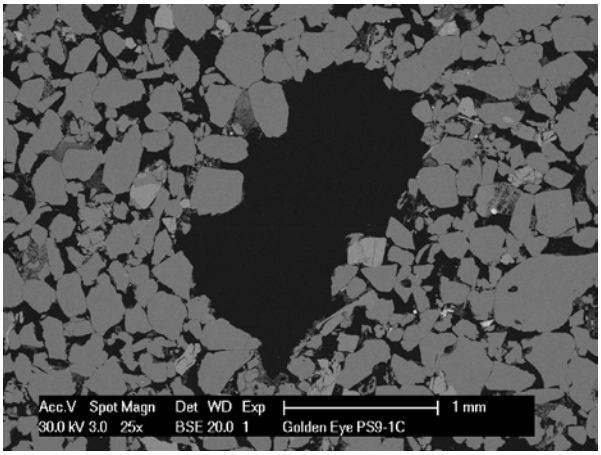

Fig. 3-9—BSEM image of the post-experiment sample showing a large hole, caused by the dissolution of a large calcite aggregate.

At the end of the experiment, shear failure was induced, leading to failure along a discrete fracture plane. The grain size of the (quartz) grains in the failure plane was dramatically reduced due to

Intense breaking and fracturing.

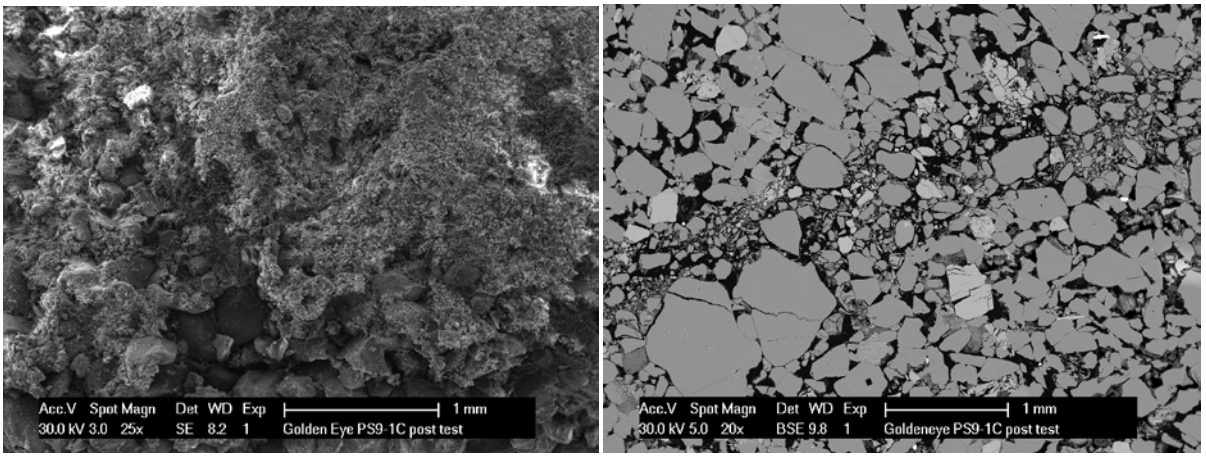

.

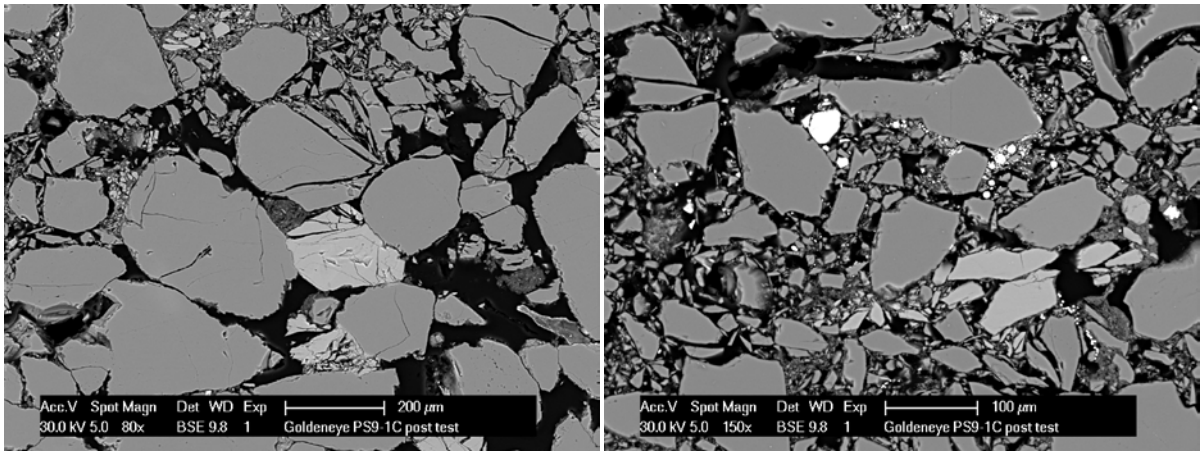

Fig. 3-10 shows SEM and BSEM images broken failure plane (oriented parallel to plane of view). It can be seen that the fault gouge consists of very small and highly angular grains (grain size generally <20 µm), though there are still remnant large well-rounded grains within the fault gouge. The fine grains result from the fracturing of larger grains during shearing along the failure plane.

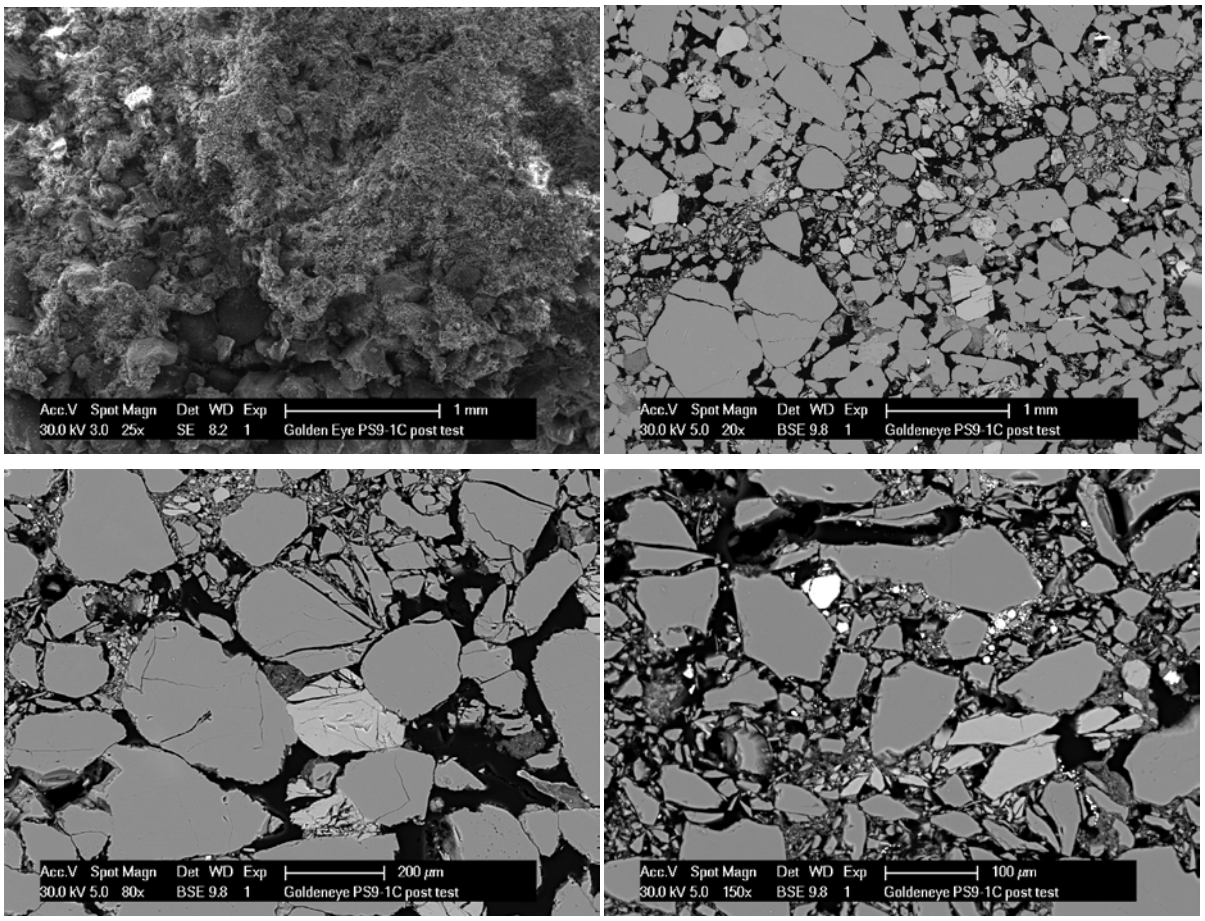

Fig. 3-10: A) Low magnification (25 x) section of the failure plane.

Note: Note the very fine grained fabric; B) Low magnification (20 x) BSEM image across the failure plane. Notice the strong reduction in grain size in the failure plane (i.e. the fault gouge) and the scattering of quartz grains into small angular pieces; C) Higher magnification (80 x) BSEM image of the failure plane (at the top of the image) showing extensive grain fracturing, long grain-to-grain contacts and scattered (broken) feldspar grains (light grey); D) Higher magnification (150 x) BSEM image indicative of the highly angular nature of the scattered grains in the failure plane.

3.4.3. XRD analysis

XRD analysis on a small portion of pre-and post-experiment sample PS9_1C were performed and results are shown in Table 3-3. It can be seen that analysis of the pre-experiment sample showed a minor amount of calcite (0.3 %) in the pre-experiment sample, though previous core analysis indicated that the Captain D Sandstone overall contains approximately 2 % of calcite. This suggests that calcite is most likely present in a clustered form and not fully homogenously distributed throughout the sample, explaining the presence of trace amounts of calcite in the pre-experiment sample. In the post-experiment sample, no calcite was observed by microCT scan, SEM or XRD

analysis, indicating all the calcite that was present in the starting material was completely dissolved by the CO_2-saturated brine.

Table 3-3—Semi-quantitative whole rock and clay fraction XRD analysis.

	Framework mineralogy							Clay fraction				
	Quartz	K-feldspar	Plagioclase	Calcite	Illite & mica	Illite-smectite-chlorite	Chlorite	Kaolinite	Illite	Illite-smectite-chlorite	Chlorite	Kaolinite
Pre-expt	89	5	2	0.3	1	tr	1	2	26	14	27	33
Post-expt	86	5	2	0	1	1	1	4	25	15	28	32

3.4.4. Effluent composition and pH

Sample effluent was collected through the experiment and the cumulative effluent of every 24 hrs was analysed for elemental composition, using Inductive Coupled Plasma (ICP), and solution pH. Note that pH is measured under ambient pressure and temperature, and hence is significantly higher than the pH at the in-situ conditions (i.e. pH ~ 3). We will proceed to present the results for the Ca^{2+} and pH measurements, as both are a good indicator for calcite dissolution. During the initial stage of CO_2-saturated brine flow, the concentration of calcium increased to 1600 ppm. The calcium concentration decreased to 1000 to 1150 ppm, which was close to the initial calcium concentration of the brine, after ~550 ml of CO_2-satured brine flow. At the same time, pH follows a trend similar to that of the calcium concentration. During the flow with CO_2-saturated brine, the pH is gradually decreasing from 6 to ~5 after 550 ml of CO_2-saturated brine flow. Hereafter, the pH remains nearly constant at pH = 5.0 ±0.2. This result indicates that once all the calcite is dissolved there is no more buffering capacity present within the rock sample and the pH of the acidic CO_2-saturated brine solution is measured.

It should be noted that for sample PS9_1C, it appears that calcite is already being dissolved during the brine flow stage. However, studying the trends of the other elements in solution indicated the presence of other cations, not present in the initial brine. This could indicate that there are impurities present in the sample as they contained a residual fluid, which was not removed prior to the experiment. This may have distorted the results of the first few effluent samples. There are no artefacts found in any of the following effluent samples taken during CO_2-saturated brine flow, which indicates that the measured excess calcium concentration is a measure of calcite dissolution.

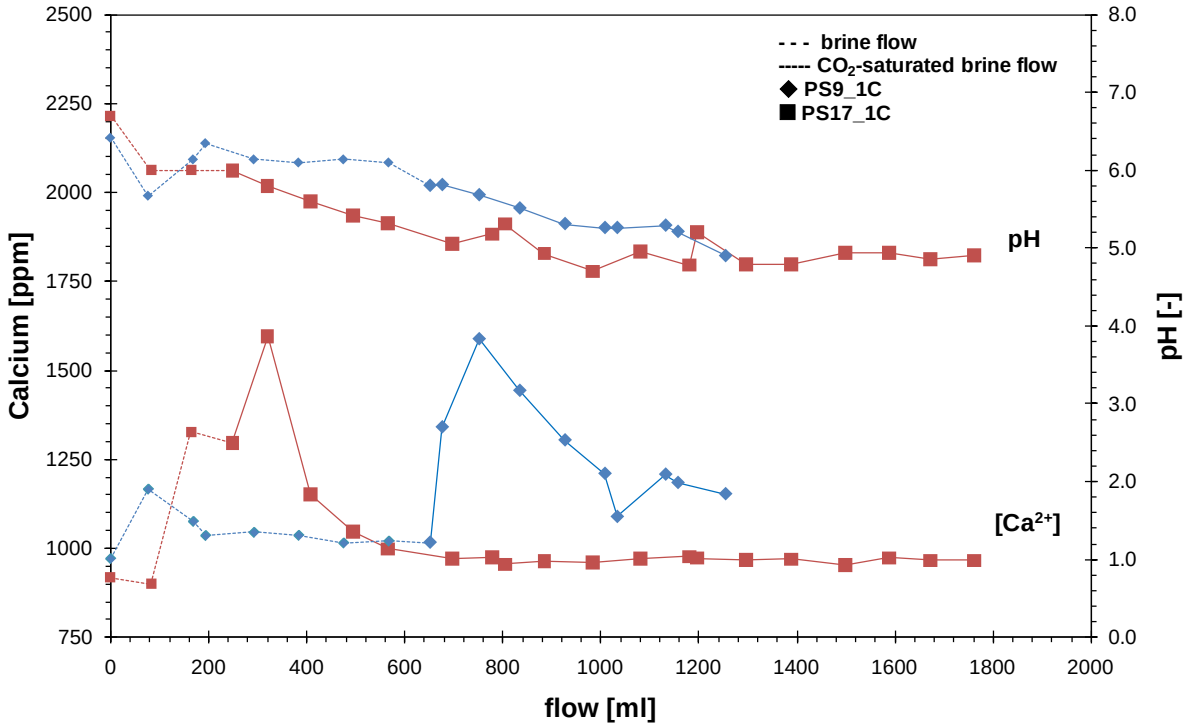

Fig. 3-11—Calcium concentration and pH of effluent samples obtained during the brine and CO_2-saturated brine flow stages.

3.4.5. Implications

The results of our measurements of the key mechanical parameters of the Captain D Sandstone were compared to values obtained in a previous study[4] on the same/similar material (Captain D and C). It can be seen that our values for Young's modulus are larger than those previously measured, i.e. 15.7 GPa vs. 6.0 GPa, respectively. It should be noted that in the latter study, Young's modulus was only determined using the first loading cycle, at confining stress conditions lower than those used in the current study (P_{rad} = 0.5-20 MPa). However, it should be noted that the previous results show values for E comparable to the Young's modulus values obtained in the present experiments during triaxial loading to in-situ stress conditions (step 1) and the first depletion step (step 2). The Poisson's ratio values found in the previous study were close to zero ($\nu < 0.1$), where higher values are expected for sandstone material. Again, these ν values are close to the values seen during the first step of our experiments. As seen in Fig. 4-1, there is quite some variation in the range of values for E, ν and K_b, which is most likely associated with sample variability (i.e. sample porosity, composition etc.).

Analysis of the samples flushed with CO_2-saturated brine pre- and post-experiment has clearly shown the removal of calcite by the acidic brine. Therefore, we will proceed to compare our failure strength data after CO_2-brine-rock interaction to failure behaviour observed in a previous study[4] without rock-fluid interaction. The latter data has provided a Mohr-Coulomb failure envelope, indicating a material

[4] M. de Kroon and G.H.M. Hertogh 1997. Dallas Dhu Sand Failure Prediction, Note for File EPT-IP SFP/97/10/01.

cohesion of 3.0 MPa and a friction angle of 34° for Captain C-D Sandstone. We have plotted the previous data together with the failure data obtained in this study in P'-Q stress space, with P' = (S_{ax} + 2P_{rad})/3 – P_{pore} and Q = S_{ax} – P_{rad} [MPa] (Fig. 3-12). As can be seen, the failure strength obtained in our experiments falls in line with the previously obtained material strength. Therefore, it can be concluded that the continuous flushing of the material with CO_2-saturated brine does not affect material strength. A likely explanation is that the reservoir material was already poorly consolidated, as confirmed by the very low cohesion of 3 MPa, and removal of calcite cement did not lead to further loss of cohesion, i.e. did not lead to any significant weakening. It is likely that for more competent rocks, with higher cohesion values, dissolution of carbonate cement may lead to a significant loss of strength. In addition, though analysis of the shear plane formed during failure showed a significant reduction of grain size (down to 20 µm), which may lead to fines-production during well shut-in, under the conditions at which CO_2 injection will take place (S_{ax}^{eff} = 28.5 MPa, P_{rad}^{eff} = 15.0 MPa, P_{pore} = 23.0 MPa) it is unlikely that failure as a result of calcite dissolution will occur (Fig. 3-12). However, it should be noted that the effect of long-term reactions (10 to 100s of years), such as feldspar and clay interactions, is to date unclear.

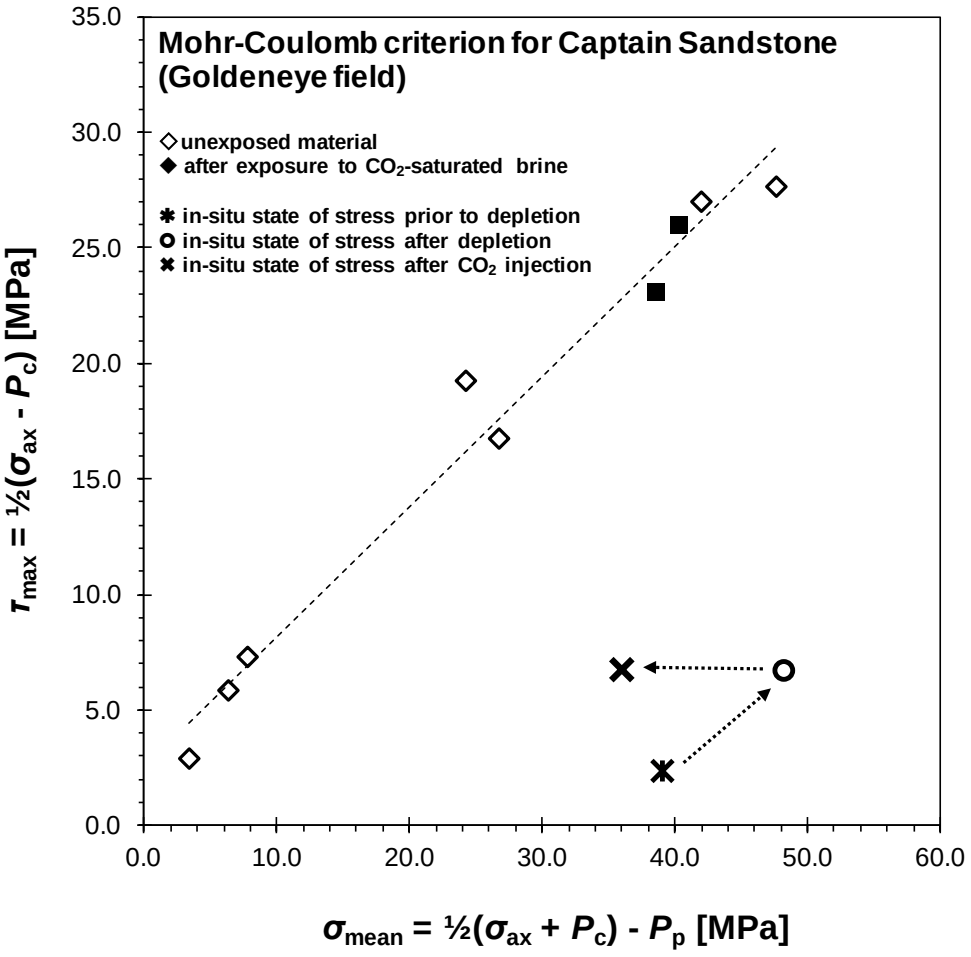

Fig. 3-12—Failure envelope for Captain Sandstone in P'-Q stress space obtained using data from a previous study[4], as well as data obtained in this study.

4. Conclusions

In summary, the rock mechanical parameters of Captain D Sandstone (Wells 14/29a-3 and 14/29a-5, Goldeneye field, UK North Sea) and the effect of CO_2-saturated brine flow on them were studied.

Mechanical properties measured include:

- Young's modulus, Poisson's ratio, bulk modulus before and during CO_2 exposure.
- Failure strength under in-situ conditions, after CO_2 exposure.
- Axial V_p and V_s, as well stress and strain sensitivity (*R*- and *S*-factors).

The main findings or our study are:

i. Calcite was completely dissolved during CO_2-saturated brine flow. This was confirmed by comparison of microCT-scan, XRD and SEM analysis of the pre- and post-experiment sample.
ii. Elemental analysis of the effluent showed an increase of the calcium concentration in the effluent in the first part of the flow phase, indicative of calcite dissolution. In the same part of the flow phase, the pH gradually decreased from pH ≈ 6 to 5, after which it stayed constant for the remainder of the experiment.
iii. No significant change in rock mechanical parameters (Young's modulus, Poisson's ratio, bulk modulus and velocities) was observed in response to the continuous flow of artificial reservoir brine and CO_2-saturated brine.
iv. There was no measurable rock strength reduction as a result of exposure to CO_2-saturated brine, and the concomitant dissolution of calcite.
v. The experiment has shown that P-wave velocity and ultrasonic attenuation are good indicators for supercritical CO_2 coming out of the solution. The S-wave velocity was not sensitive to pore-fluid changes.

Results are summarized in Table 3-1 and Table 3-2, and Fig. 3-1—Stress strain plot for pore pressure depletion steps.

APPENDIX 1. Experimental setup

The experiments described in this report were performed using a triaxial compression apparatus. A schematic diagram of the triaxial compression machine is shown in Fig. 4-1A. A cylindrical sample (1.5" in diameter and 3" in length) was placed between titanium end-caps and enclosed in impermeable Teflon Shrink tubing and a 2.5 mm thick HNBR sleeve. The end-caps contained small 1 mm bores for pore fluid access. The bores were offset out of the acoustic measurement path. The sample and end-caps assembly was mounted into a 100 MPa capacity pressure vessel with an integral axial loading piston. The sample was loaded axially by applying a fluid pressure in the chamber at the bottom of the loading piston using a piston (hydraulic) actuator. Axial pressure was measured using a 100 MPa pressure gauge and controlled to within 0.1 MPa by a custom analog servo-controller. Radial stress was applied directly to the sample through oil pressure on the elastomer sleeve using a similar piston (hydraulic) actuator, pressure gauge and controller. Pore-fluid pressure was generated by a piston actuator and applied through the top end-cap, and monitored with 100 MPa gauges at both the top and bottom to verify full pore-pressure communication in the sample during testing. The compression cell was located in an oven, which could be heated to a maximum of 150°C.

Changes in the sample length are measured using two internal linear variable displacement transducers (LVDT's) in contact with the end-caps. During processing, the raw axial displacement data was corrected for the axial deformation of the end-caps due to axial and radial loads and temperature changes. The change in the diameter of the sample was measured using a strain-gauged cantilever bridge. The sensor was clamped onto two pins that pierced the elastomer sleeve, making direct contact with the sample at opposite sides. During loading under uniaxial constant-lateral strain conditions, the total radial stress was varied to maintain a constant radial dimension using the above-mentioned servo-controller, and included corrections for pressure effects on the radial sensor. Calibration experiments on aluminium samples showed that the radial displacement under uniaxial constant-strain conditions can be maintained within 0.02 μm.

For CO_2-saturated brine flow experiments (PSx_1C series), a new CO_2 flow unit was incorporated into the existing triaxial compression apparatus. During the experiment, it was possible to measure axial and radial displacements and ultrasonic axial P- and S-wave velocities. This allowed for the determination of static and dynamic rock properties. In Fig. 4-1B, a simplified flow scheme of the CO_2 flow unit is given. In the original configuration of the triaxial compression machine, pore pressure was applied to the sample by means of an ISCO® pump. In the new situation, there is a possibility to:

1) Apply pore pressure with brine using an ISCO pump (original configuration).
2) Apply CO_2-saturated brine flow through the core.
3) Apply CO_2 flow through the core.

For the PSx_1C experiments, brine was saturated with SC CO_2 in an autoclave at 35°C. The pressure and temperature conditions of the autoclave were selected such that we obtained fully saturated CO_2-rich brine, even at the higher pore pressure and temperature present in the sample, and to avoid CO_2 coming out of solution.

Fig. 4-2 shows the CO_2 solubility in water as a function of temperature and pressure. In a test measurement, monitoring ultrasonic attenuation, we confirmed that no CO_2 was coming out of the solution in the rock sample and that the brine was almost fully CO_2-saturated for the chosen mixing conditions (CO_2-brine volume ratio of 1:2). During the experiments, CO_2-saturated brine was fed into a Quizix® pump (pump 1), which pumped at a constant fluid flow rate. Quizix® pump 2 was used to maintain pore pressure at a constant value in the CO_2 flow loop. The effluent was collected for further analysis. Throughout the entire experiment, data acquisition and experiment sequence control were done by custom software operating on a PC computer.

A

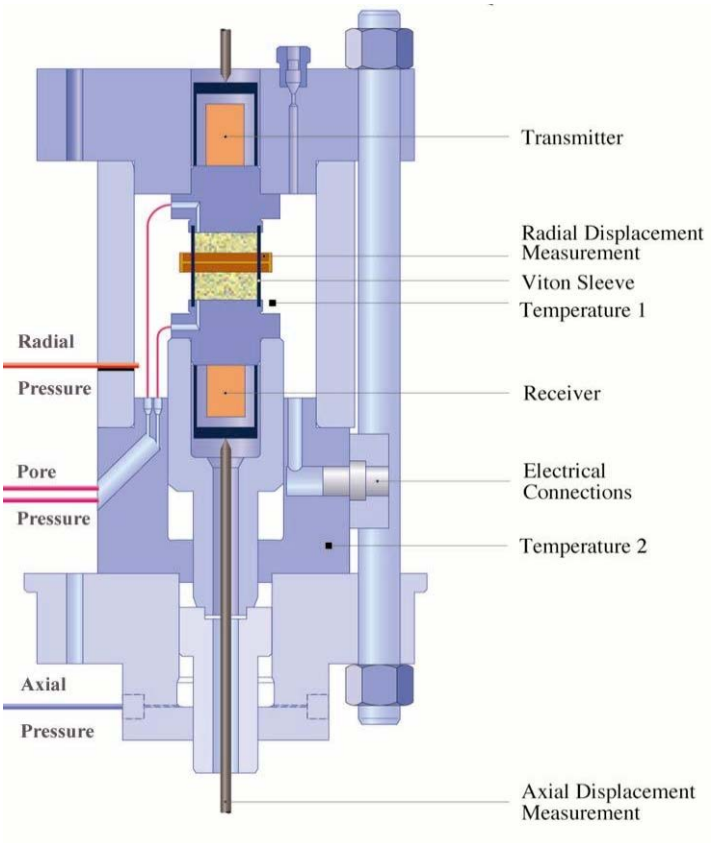

B

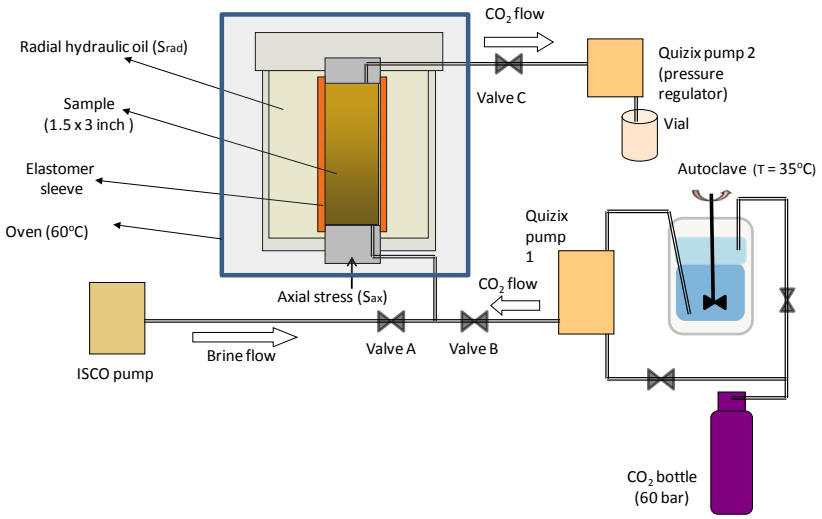

Fig. 4-1—A) Schematic diagram of the triaxial apparatus. The radial transducer set-up for radial ultrasonic velocity measurements are not shown in this diagram; B) Schematic of the CO_2 flow loop scheme that was added to the existing triaxial compression apparatus.

Fig. 4-2—Solubility curves of CO_2 in water as function of temperature and pressure.

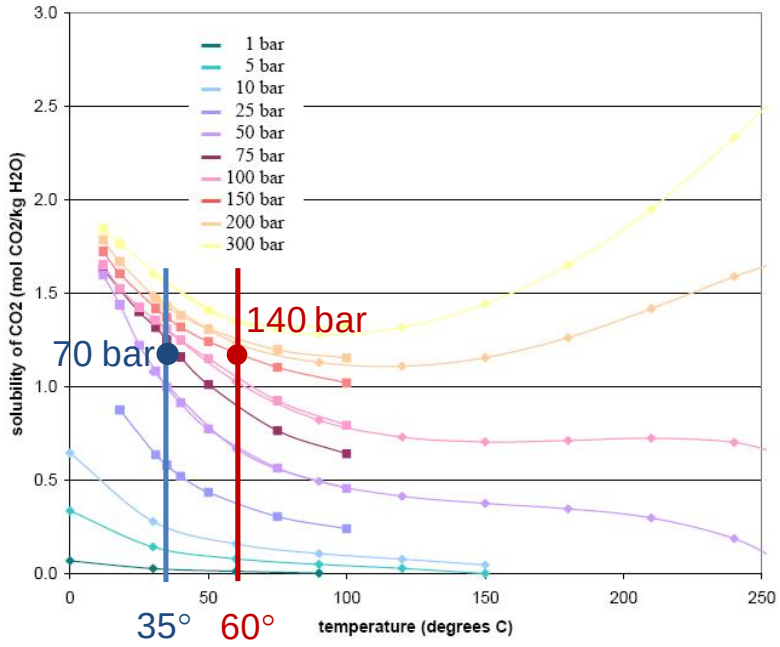

APPENDIX 2. Analytical methods

A2.1. XRD analysis

The X-ray diffraction semi-quantitative mineralogical analysis of sample PS9_1C, pre- and post experiment, were carried out by PETROCLAYS

A2.1.1. Methods

A portion of each sample was gently crushed, mixed with distilled water plus a few drops of ammonia as a dispersant and placed in an ultrasonic bath for 30 mins to release the maximum amount of clay into suspension. The clay suspension was then centrifuged to deposit the entire < 2 μm fraction, which was filtered (mixed with a little distilled water to make a thick slurry) onto unglazed ceramic tiles. A further portion was ground to a powder in a Tema mill (using industrial methylated spirits to minimise structural grinding damage). A few drops of the resulting slurry were allowed to dry on a silicon wafer. The samples were scanned using a Phillips 1820 automated X-ray diffractometer using Ni-filtered CuKα radiation. Clay tiles were scanned at a rate of 5 secs per 0.02° step width, using 0.3 mm slits from 2 to 40° 2θ. The tiles were scanned again after heating at 400°C for 4 hours, and after heating at 550°C, also for 4 hours. The whole rock powder samples were scanned at a rate of 15 secs per 0.15° step width with a 5° slit, from 5 to 70° 2θ.

A2.1.2. Results

The data has been quantified using Macdiff to de-convolute and measure peak areas. The relative proportions of each mineral are calculated by weighting the area of the chosen mineral reflection by a factor (mineral intensity factor) determined from measurement of known mixtures of the appropriate minerals, and normalizing the results.

Some of the swelling clay has a low proportion of chlorite mixed layers, indicating the presence of a illite-smectite-chlorite mineral. The amount of calcite in the pre-experiment sample was measured as <1 %, at the request of Fons Marcelis this was adjusted to 0.3 %, the amount measured by a more accurate approach.

A2.2. SEM analysis

SEM analysis was performed with the in-house Philips XL-40 FEG SEM (Scanning Electron Microscope), at Shell International Exploration and Production BV., Rijswijk, the Netherlands.

A2.2.1. Equipment

The FEG SEM microscope was recently upgraded with a state-of-the-art EDAX TEAM system with the Apollo SDD (Silicon Drift Detector) detector and the newest energy dispersive software. The SEM is equipped with a SE detector (Secondary Electrons) and a BSE (backscattered secondary electrons) detector. The SE detector is a very powerful tool to study grain morphology and pore structure. The BSE detector was used to study the polished surfaces and provides grey scale images showing different minerals in different grey scale colors. EDAX spectra were used for mineral identification.

A2.2.2. Sample preparation

A trim end was cut from the as-received original sample PS9_1C. This trim end was dried in a hot oven. A small chip was carefully broken from it and mounted on a SEM stub. After coating the surface of this rock chip with a very thin layer of gold, the sample was studied under the SEM. The remainder of the trim end was impregnated with a clear resin and highly polished. The surface of this polished block was coated with carbon, whereas the edges were coated with gold.

Also the post-experiment sample PS9_1C was prepared for SEM analysis. Therefore, the plug sample was cleaned to remove any residual brine, oven-dried and processed using a microCT scanner (see Section 3.4.1). The scans of the sample were used to orient the sample and cut sections/slices from it. These sections were used for fresh surface SEM analysis of the shear/failure plane and the adjacent rock, as well as for impregnation and polishing of the rock containing the failure plane for BSEM analysis. The coating of the samples was performed using the Emscope gold and carbon sputter coaters.

5. Glossary

Vp	Compressional Velocity
Vs	Shear Wave Velocity
microCT	Micro-Computer Tomography
XRD	X-ray Diffraction
SEM	Scanning Electron Microscopy
Kw	Permeability
HNBR	Hydrogenated Nitrile Butadiene Rubber
R	Strain-Sensitivity Factor
S	Stress-Sensitivity Factor
BSEM	back-scanning electron microscopy
EDAX	Energy Dispersive X-ray

6. Glossary of Unit Conversions

For the provision of the SI metric conversion factor as applicable to all imperial units in the Key Knowledge Deliverable.

Table 6-1: Unit Conversion Table

Function	Unit - Imperial to SI Metric conversion Factor
Length	1 Foot = 0.3048m Metres 1 Inch = 2.54cm Centimetres 1 Inch = 25.4mm millimetres
Pressure	1 Psia = 0.0690 Bara
Temperature	1°F Fahrenheit = -17.22°C Centigrade
Weight	1lb Pound = 0.45kg Kilogram